

HYBRID CAVITY-PLASMON MODE ENGINEERING WITH  
ELECTRONS ON HELIUM

By

Camille A. Mikolas

A DISSERTATION

Submitted to  
Michigan State University  
in partial fulfillment of the requirements  
for the degree of

Physics — Doctor of Philosophy

2025

## ABSTRACT

### HYBRID CAVITY-PLASMON MODE ENGINEERING WITH ELECTRONS ON HELIUM

By

Camille A. Mikolas

Electrons floating above the surface of superfluid helium are a unique platform for investigating a wide variety of collective phenomena in strongly interacting condensed matter. Additionally, hybrid quantum systems offer a versatile way to explore both the fundamental physics and quantum information science applications of single particle and collective quantum systems. In particular, hybrid systems containing superconducting coplanar waveguide resonators are emerging as an ideal tool for investigating the microwave-frequency collective dynamics of low-dimensional electron systems. In this thesis, we present experimental results from microchannel device architectures which allow us to engineer microwave frequency charge density waves (i.e. plasmons) in electrons on helium and couple those collective excitations to superconducting resonators. The microchannel device provides precision control over the electron density and enables access to both quasi-one-dimensional electron chains as well as two-dimensional electron sheets. In the hybrid system coupling a superconducting coplanar waveguide resonator with the electron on helium system, spectroscopic measurements of the resonator allow us to demonstrate coupling between a plasmonic excitation with the fundamental mode of the superconducting resonator, with coupling strength  $g = 50$  MHz. Finally, we discuss how this hybrid system offers a novel platform for cavity optoplasmonic and circuit quantum electrodynamic experiments with electrons on helium.

## ACKNOWLEDGMENTS

A wise physicist once said “I am of the conviction that it takes a village to raise a physicist”. That physicist was Dr. Justin Lane. He is right and was an important one of the many people that helped me to become the physicist I am today. Of the people that have contributed to my journey these last six years, my advisor, Johannes Pollanen, has been central to my academic journey and shaping me as a scientist. His eagerness to troubleshoot problems in the lab and enthusiasm for both educating and learning has made this entire process truly so enjoyable. I can with confidence say, I am better off as a physicist (and maybe as a person) because of Johannes. Thank you for always having an open door and (almost) always answering my FaceTime calls.

Additionally, I would like to thank the members of my committee: Prof. Norman Birge, Prof. Mark Dykman, Prof. Ryan LaRose, and Prof. Angela Wilson. In particular, it has been a great experience to be able to have the guidance of Mark, whose intuition for electrons on helium is invaluable. I would also like to thank Kim Crosslan, who always made sure I was taken care of.

My experience at Michigan State University would be nothing without the graduate students and postdocs I have been lucky enough to collaborate with and learn from. I am beyond grateful to have been able to be mentored by our former postdoc, Dr. Niyaz Beysengulov. From being my personal electrons on helium expert on speed dial to becoming a dear friend (and at times, therapist) – I am a better experimentalist because of you. Being a part of the Laboratory for Hybrid Quantum Systems (LHQS) has brought so many valuable collaborators and friends into my life that I am indebted to. If you know me, you know that means Camryn Undershute, in particular. She has truly made me a better

scientist in every way and I am forever grateful for all I have learned from her and for her unwavering support and friendship. I am also indebted to Dr. Joe Kitzman for always answering my quantum device questions and my valuable electrons on helium collaborator Austin Schleusner. Another former LHQS-er I am indebted to and so grateful for is Dr. Heejun Byeon, who has helped me immensely in developing the electrons on helium devices discussed in this thesis.

While many people at MSU have been an irreplaceable part of my journey, those outside of MSU have also supported me along the way. My dear friends who were so close (but so far) – Brandon, Sarah, and James. I don't know what I would do without you guys and the invention of FaceTime. And of course, my family members who have given me all the support I could ever need – Mom, Grandma Barbara, Grandpa Terry and Ralph. I also feel like I should acknowledge Freddie Freeman – I don't actually know him, but that grand slam in Game 1 of the 2024 World Series really gave me the mental support I needed as I was wrapping up my research.

The projects described in this dissertation were partially supported by the National Science Foundation under grant numbers DMR-2003815 and ECCS-2142846 (CAREER), and by the generous support of the Cowen Family Endowment. I would also like to thank Reza Loloee and Dan Edmunds for their invaluable technical assistance and Baokang Bi for device fabrication advice and use of the W.M. Keck Microfabrication Facility at MSU. A portion of this work made use of the Pritzker Nanofabrication Facility of the Institute for Molecular Engineering at the University of Chicago, which receives support from Soft and Hybrid Nanotechnology Experimental (SHyNE) Resource (NSF ECCS-2025633), a node of the National Science Foundation's National Nanotechnology Coordinated Infrastructure.

# TABLE OF CONTENTS

<b>Chapter 1</b>	<b>Overview</b>	<b>1</b>
1.1	A brief overview of electrons on helium	1
1.2	Overview of this thesis	3
<b>Chapter 2</b>	<b>Introduction</b>	<b>5</b>
2.1	Basics of electrons on helium	5
2.1.1	Superfluid helium	5
2.1.2	Electrons bound to the superfluid helium surface	6
2.1.2.1	A single trapped electron	6
2.1.2.2	Ensembles of electrons	10
2.1.3	Correlations and Wigner crystallization	13
2.2	Plasmons and collective phenomena	16
2.2.1	Collective phenomena in electrons on helium	17
2.2.2	Plasmons in electrons on helium	18
2.2.2.1	Two-dimensional screened plasmon dispersion relation	19
2.3	Transport properties of electrons on bulk helium	26
2.3.1	Mobility	26
2.3.1.1	The Drude model	27
2.3.1.2	Scatterers: Vapor atoms and ripplons	29
2.3.2	Sommer-Tanner transport measurements	32
2.3.3	Transport of the Wigner crystal	36
2.3.3.1	Bragg-Cherenkov scattering	38
2.3.3.2	The unresolved microscopic picture: crystal sliding versus melting	40
2.4	Microchannel devices for electrons on helium	41
2.4.1	Superfluid helium as a substrate in microchannel devices	42
2.4.2	Critical electron density	45
2.4.3	Transport measurements in microchannel devices	48
2.4.4	Confinement	52
2.5	Quantum devices with electrons on helium	53
2.5.1	Qubits with trapped electrons on helium	53
2.5.2	Single electron transistors	55
2.5.3	Charge-coupled devices	56
<b>Chapter 3</b>	<b>Plasmon mode engineering with microchannel devices</b>	<b>58</b>
3.1	Experimental setup	60
3.1.1	Microchannel device for plasmon confinement	60
3.1.2	Transport measurements & microwave excitation	64
3.2	Detection and analysis of plasmon modes	66
3.2.1	Plasmon detection	66
3.2.2	Non-equilibrium transport in the presence of microwave excitation	69

3.2.3	Plasmon mode generation and coupling . . . . .	73
3.2.4	Analysis of plasmon mode structure . . . . .	74
3.2.5	Power dependence of plasmon modes . . . . .	76
3.2.5.1	Evolution of the plasmon lineshape . . . . .	77
3.2.5.2	Sources of plasmon broadening . . . . .	79
3.2.6	Reservoir dependence of the resonance features . . . . .	81
3.2.7	Consideration of the one-dimensional dispersion relation . . . . .	84
3.3	Summary of results . . . . .	87
<b>Chapter 4 Coupling plasmons in electrons on helium to superconducting resonators . . . . .</b>		<b>89</b>
4.1	Integrating superconducting resonators with microchannel devices . . . . .	91
4.1.1	Superconducting coplanar waveguide resonators . . . . .	91
4.1.2	Composite resonator and microchannel device . . . . .	93
4.1.2.1	General device architecture . . . . .	93
4.1.2.2	Microchannel-CPW resonator device operation . . . . .	98
4.2	Standard transport measurements and transport assisted cavity spectroscopy	101
4.3	Plasmon-resonator coupling . . . . .	105
4.3.1	Spectroscopy of the coupled resonator-plasmon system . . . . .	105
4.3.2	Plasmon-resonator interaction: two classical coupled oscillators . . . . .	107
4.3.2.1	Electric field coupling and boundary conditions . . . . .	107
4.3.2.2	Coupled system equations of motion and eigenfrequencies . . . . .	110
4.3.3	Analysis of the effective plasmon-resonator coupling . . . . .	114
4.3.4	Summary of results . . . . .	117
<b>Chapter 5 Using superconducting resonators to investigate helium surface fluctuations . . . . .</b>		<b>119</b>
5.1	Superconducting coplanar waveguide resonator device . . . . .	120
5.2	Resonator spectroscopy . . . . .	121
5.3	Resonator response to liquid helium . . . . .	124
5.4	Investigating helium surface fluctuations . . . . .	126
5.5	Summary of results . . . . .	129
<b>Chapter 6 Conclusion and outlook . . . . .</b>		<b>130</b>
6.1	Summary of work . . . . .	130
6.2	Outlook and future directions . . . . .	132
6.2.1	Resolving the unresolved: Wigner crystal <i>sliding</i> vs <i>melting</i> . . . . .	132
6.2.2	Towards strong coupling with a longer lifetime plasmon in electrons on helium . . . . .	133
6.2.3	Regimes of cQED and cavity optoplasmonics with plasmons in electrons on helium . . . . .	133
<b>APPENDICES . . . . .</b>		<b>135</b>

Appendix A Measurement apparatus, circuits, and protocol . . . . .	136
A.1 Measurement apparatus and circuit components . . . . .	136
A.2 Pre-experiment device preparation . . . . .	137
A.2.1 Sample cell “pump & flush” procedure . . . . .	137
A.2.2 Condensing helium into sample cell . . . . .	138
A.2.3 Electron firing procedure . . . . .	139
A.3 Plasmon mode engineering device . . . . .	140
A.4 Microchannel-resonator hybrid device . . . . .	141
A.4.1 Helium filling characteristics of the resonators . . . . .	142
A.4.2 Reservoir voltage dependence for avoided crossing measurements . . .	143
Appendix B Fabricating microchannel devices . . . . .	147
B.1 Silicon chip cleaning protocol . . . . .	147
B.2 Fabrication of plasmon mode device . . . . .	148
Appendix C Finite element modeling calculations for devices . . . . .	155
C.1 FEM for microchannel devices . . . . .	155
C.2 Method 1: FEM calculation of coupling constants, $\alpha(x, y)$ . . . . .	156
C.3 Method 2: FEM calculation of densities, $n_s$ , using the microchannel device cross section . . . . .	157

# Chapter 1

## Overview

### 1.1 A brief overview of electrons on helium

Electrons on helium refers to the system that consists of electrons floating in vacuum above a liquid or superfluid helium surface. As a consequence of free electrons existing in proximity to the liquid helium surface, like any dielectric, the helium substrate becomes polarized. In fact, helium is a nearly perfect dielectric ( $\epsilon_{\text{He}} = 1.057$ )! The free electron is naturally attracted to the surface of the superfluid by the positive image charge it induces in the dielectric liquid, but prevented from entering the helium by the lack of open electronic states. The combination of these effects confines the electron approximately 11 nm above the surface of the superfluid. The simple fact that electrons can exist freely, while remaining vertically confined while spatially controllable around the xy-plane (more on that later), opens the door to possibilities of investigations in fundamental physics no other system can compete with. Every quantum mechanic textbook asks you to consider a free spin-1/2 particle and the system of electrons on helium provides that experimental platform. From probing quantum physics with single particle experiments to the strongly correlated collective dynamics of Coulomb liquids, electrons on helium affords the foundation for studying fundamental physics via a fundamental platform.

In the late 1960s through the mid-1970s, electrons on helium was a leading platform to

investigate two-dimensional electron systems (2DES). The first experimental evidence of a 2DES on liquid helium was in 1964, when Sommer reported findings on measurements of the potential barrier electrons must overcome to penetrate the helium surface [1]. Between 1969-1970, following the initial experiments of measuring the liquid helium potential barrier [1, 2], theoretical explanations of these surface electron states were developed [3, 4]. However, the true inflection point was in 1971, when Crandall and Williams proposed electrons on helium as the optimal platform to demonstrate the crystallization of an electron system [5], or Wigner crystallization [6]. Up until this point, Wigner crystallization had not been demonstrated in any system since its theoretical conception in 1934 [6]. Forty-five years after Wigner proposed the possibility of a solid electronic state of matter, the first experimental demonstration of the Wigner crystal was done with electrons on helium [7].

An ensemble of such electrons forms a unique trapped particle system, which bears many similarities to systems of trapped ions [8, 9]. Electrons confined above the surface of liquid helium are characterized by extremely strong electron-electron interactions [10]. These interactions lead to correlated electronic fluid and Wigner solid [7] many-body ground states possessing exotic spatial order [11] and temporal dynamics. In addition to the strong electron-electron interactions produced by the Coulomb force, electrons on helium also interact with a quantum field of helium surface vibrations, which leads to rich and nontrivial quantum many-body behavior [12]. The electrons reside in a pristine environment, devoid of defects or disorder, allowing for investigation of many-body phenomena (e.g. non-equilibrium phase transitions and collective modes) in a controlled way, which is difficult (if not impossible) to do in other areas of condensed matter physics. While there has been significant progress studying electrons on helium, many fundamental questions related to the nature of the collective electron ground states and their dynamics remain open. Tremendous advances in

nano-fabrication techniques have allowed for the creation of devices in which electrons on helium can be precisely confined in tailor-made geometries and mesoscopic devices [11, 13, 14], however, the overwhelming majority of experiments conducted to-date have relied on conventional transport measurements to investigate the trapped electron system in these device architectures. Qualitatively new opportunities to use electrons on helium as a model system for studying open questions in condensed matter arise by integrating the electron system with the experimental framework of circuit quantum electrodynamics (cQED). The work in this thesis largely aims to understand and integrate the collective excitations in electrons on helium in the presence of the superconducting resonators used in cQED architectures.

## 1.2 Overview of this thesis

To start, in Chapter 2, we lay the groundwork for understanding the basic concepts of single electrons on helium, ensembles of electrons on helium, and what integrating quantum circuits with these systems looks like. Then in Chapter 3, we discuss the microchannel device architecture we have developed that enables us to generate and detect microwave frequency plasmon modes. From this device, we are able to create a next generation architecture which includes a superconducting coplanar waveguide resonator coupled to the microchannel confined plasmon mode, which we describe and discuss the results of in Chapter 4. In Chapter 5 we present experiments investigating the effects of the superfluid helium on a superconducting resonator, and further find the resonator allows us to investigate the helium surface fluctuations. In the final chapter of this thesis, Chapter 6, we discuss how the work presented here paves the way for novel hybrid quantum systems that integrate electrons on helium with quantum circuits. We outline experiments in cavity optoplasmonics and circuit

quantum electrodynamics, aiming to explore a new framework for hybrid quantum systems with electrons on helium.

# Chapter 2

## Introduction

### 2.1 Basics of electrons on helium

#### 2.1.1 Superfluid helium

The discussions and experiments presented throughout this thesis are carried out with *superfluid*  ${}^4\text{He}$ . As you will see in the subsequent sections, electrons can be bound to the surface of superfluid  ${}^4\text{He}$ , however electrons can also be bound to the normal liquid  ${}^4\text{He}$  surface as well as to both liquid and superfluid  ${}^3\text{He}$  surfaces. At room temperature and ambient pressure, the stable isotope  ${}^4\text{He}$  is gaseous and at sufficiently low temperature it can be liquefied. In 1908, Heike Kamerlingh Onnes showed that at atmospheric pressures,  ${}^4\text{He}$  liquefies at 4.2 K, which earned him the 1913 Nobel Prize in Physics [15]. Unlike any other element, at atmospheric pressure  ${}^4\text{He}$  will not solidify even when cooled down to absolute zero. However, as the temperature gets near absolute zero helium will undergo a phase transition into a superfluid state. The superfluid phase is characterized by fluid flow without kinetic energy loss, i.e. zero viscosity. Superfluidity in  ${}^4\text{He}$  was first experimentally observed in 1938 by Pyotr Kapitza – this phase transition occurs at or below the so-called “ $\lambda$ -point”,  $T_\lambda = 2.2$  K [16, 17]. Superfluidity in helium is a result of the atoms occupying a collective quantum mechanical ground state, similar to Bose-Einstein condensation. However, the superfluid is a highly dense quantum liquid such that standard Bose-Einstein condensation

(BEC) theory cannot be used to fully describe it, as the theory neglects the interactions between particles. For superfluid  $^4\text{He}$ , one must consider the two fluid model [18]. A full description of superfluidity in helium is beyond the scope of this thesis, however for a well contained and comprehensive resource, I refer the reader to Ref. [18]. Additional details on how we utilize the lack of viscosity of superfluid  $^4\text{He}$  in the devices presented in this thesis are discussed in Sec. 2.4.1.

## 2.1.2 Electrons bound to the superfluid helium surface

Imagine you have your favorite box of free electron cereal, a bowl, and a carton of superfluid helium. If you fill the bowl with liquid helium and try to pour electrons into the bowl, they will actually float about ten nanometers above the superfluid helium surface. This collection of electrons will form a bound two-dimensional surface state electron system on helium, which is a model system for studying a wide range of topics and systems in condensed matter physics such as Coulomb liquids [19–25] and Wigner solids [6, 7, 26–29], the Hall effect [30–33], collective excitations of electron ensembles [34–44], and low-dimensional transport at the highest mobilities of any two-dimensional electron system (2DES) [45, 46].

### 2.1.2.1 A single trapped electron

When a free electron meets the surface of liquid (or superfluid) helium, the electron will hover above the surface as a result of the competition between a long-range attraction – from an image charge formed beneath the helium surface ( $\epsilon_{\text{He}} \simeq 1.057$ ) – and the short-range repulsion – a consequence of the Pauli exclusion principle which forbids an additional electron in the already full valence shell of the helium atoms (see Fig. 2.1a). The bound electron above the liquid helium surface creates a hydrogen atom-like energy spectrum of

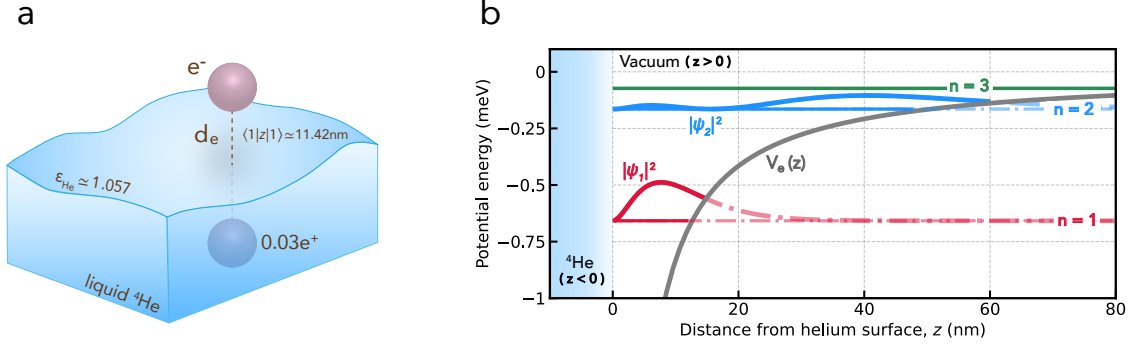


Figure 2.1: **Floating electron above the surface of liquid helium.** (a) Depiction of a single electron floating above the surface of liquid helium ( ${}^4\text{He}$ ). The liquid helium is a nearly perfect dielectric ( $\epsilon_{\text{He}} \simeq 1.057$ ) and when an electron is at the surface an image charge forms beneath the surface  $0.03e^+$ . In its ground state, an electron floats a distance  $d_e = 11.42$  nm above the surface of the liquid helium, calculated from the ground state wave function expectation value. (b) Solutions to the Schrödinger equation (Eq. 2.6) for the  $n = 1$  (red curve,  $|\psi_1|^2$ ) and  $n = 2$  (blue curve,  $|\psi_2|^2$ ) hydrogenic states normal to the surface, with their corresponding energy levels (the  $n = 3$  energy level is also plotted in green). In the absence of an applied pressing field normal to the surface ( $E_{\perp} = 0$ ), the potential trapping the electron is  $V_e(z) \sim -\Lambda/z$  (solid dark gray line).

the motional states normal to the helium surface, i.e. Rydberg states, where the image charge formed beneath the helium surface is analogous to the nucleus of the hydrogen atom (Fig. 2.1b). An electron can remain bound above the helium surface without the help of an additional electric field normal to the helium surface ( $E_{\perp}$ ) to hold it in place, however to trap larger areal electron densities ( $n_s$ ) one must satisfy  $E_{\perp} \geq \frac{en_s}{2\epsilon_0}$ <sup>1</sup>. If we take  $E_{\perp}$  into consideration, the one-dimensional (1D) potential that traps the electrons above the helium surface takes the form:

$$V_e(z) = eE_{\perp}z + \begin{cases} -\frac{\Lambda}{z+z_0}, & z \geq 0, \\ V_0, & z < 0 \end{cases} \quad (2.1)$$

where  $e$  is the electron charge,  $V_0$  is the potential barrier the electrons must overcome to

<sup>1</sup>This comes from the requirement that in equilibrium the net force on the electrons must be zero, where the electric field created by an infinite sheet of charge will be  $E = \frac{en_s}{2\epsilon_0}$  normal to the helium surface.

penetrate the helium surface ( $V_0 \simeq 1.0$  eV) [1, 2],

$$\Lambda = \frac{e^2(\varepsilon_{\text{He}} - 1)}{4(\varepsilon_{\text{He}} + 1)} \frac{1}{4\pi\varepsilon_0} \quad (2.2)$$

is the image charge factor,  $\varepsilon_0$  is the vacuum permittivity, and  $z_0$  is an adjustable parameter that shifts the origin of the image potential inside the liquid to account for the divergence one would get in  $V_e$  at the helium surface – this value is typically chosen to be  $z_0 \approx 1$  Å based on a fit to the experimentally observed transition frequencies [47]. To approximate the Rydberg-like energy spectrum of the bound electron, we can make some simplifying assumptions. First, because the average distance of the electrons from the surface  $\langle z \rangle$  will be much larger than  $z_0$ , we can take  $z_0 \rightarrow 0$  in this approximation. Further, the typical surface electron state energies are much smaller than  $V_0$ , so we assume the fluid interface resembles an infinite potential barrier ( $V_0 \rightarrow \infty$ ) [47]. In the absence of the externally applied field  $E_{\perp}$ , we have the simplified potential,  $V_e(z) \simeq -\Lambda/z$ , and we solve the Schrödinger equation

$$-\frac{\hbar^2}{2m_e} \nabla^2 \Psi - \frac{\Lambda}{z} \Psi = E \Psi, \quad (z > 0), \quad (2.3)$$

where  $\Psi = 0$  for  $z < 0$  and  $m_e$  is the mass of the electron. With electrons free to move in the  $xy$ -plane, the symmetry of the system allows us to consider the quantized vertical motion separately, thus we consider only the 1D wave function normalized by the surface area,  $S_A$ ,

$$\Psi_n(\mathbf{r}, z) = \frac{1}{\sqrt{S_A}} e^{i\mathbf{k}\cdot\mathbf{r}} \psi_n(z). \quad (2.4)$$

Here,  $\mathbf{k}$  is the two-dimensional (2D) wave vector of the  $xy$ -plane,  $\mathbf{r}$  is the in-plane position vector, and  $n$  is the quantum number describing the vertical electron states. As noted

previously, the electron bound to the surface of liquid helium exhibits Rydberg-like energy levels, resembling the bound electron states of a hydrogen atom. By analogy, we can simply insert the image charge factor  $\Lambda$  from Eq. 2.2 into the quantized energy spectrum of the 1D hydrogen atom to write the energies of the electron bound to the helium surface:

$$E_n = -\frac{\Lambda^2 m_e}{2\hbar^2 n^2}, \quad (n = 1, 2, 3, \dots). \quad (2.5)$$

To find the wave functions of the bound electron, we use the 1D Schrödinger equation

$$\frac{d^2\psi_n(z)}{dz^2} + \frac{2m_e}{\hbar^2}\left(E_n + \frac{\Lambda}{z}\right)\psi_n(z) = 0, \quad (2.6)$$

in the position basis ( $\psi_n(z) = \langle z|n\rangle$ ) and solve for the  $n = 1$  and  $n = 2$  wave functions, where

$$\psi_1(z) = \frac{2z}{a^{3/2}}e^{-z/a} \quad (2.7)$$

$$\psi_2(z) = \frac{z(1 - z/2a)}{\sqrt{2}a^{3/2}}e^{-z/2a}. \quad (2.8)$$

Here we have defined the effective Bohr radius  $a$  of the electron state

$$a = \frac{\hbar^2}{\Lambda m_e} = \frac{a_0 e^2}{\Lambda} \quad (2.9)$$

with  $a_0 = \hbar^2/m_e e^2 \simeq 0.53 \text{ \AA}$ , and find  $a \simeq 76 \text{ \AA}$ . Using these values, we can calculate the expectation values for the vertical positions of the first two states:

$$\langle 1|z|1\rangle = 11.4 \text{ nm} \quad \& \quad \langle 2|z|2\rangle = 45.6 \text{ nm}. \quad (2.10)$$

The wave functions of the first two levels are plotted in Fig. 2.1b along with the first three energy levels,  $E_1 = -0.649$  meV (red),  $E_2 = -0.162$  meV (blue), and  $E_3 = -0.072$  meV (green). The energy difference between the ground and first excited state is  $(E_2 - E_1)/h \simeq 119$  GHz and  $(E_2 - E_1)/k_B \simeq 6$  K, which is well below standard experimental operation temperatures ( $T \simeq 0.01$  K), thus the surface electron states will generally be cooled to their vertical ground state.

In the previous analysis, we neglected the externally applied pressing field  $E_\perp$  that is present in many electrons on helium experiments. The first-order correction to the energy levels results in a linear Stark shift to the hydrogen atom-like energy spectrum. The ground state wave function can be found by using a trial wave function of the same form as Eq. 2.7 and then solving the 1D Schrödinger equation given by Eq. 2.6 (using the variational method) with the full expression for  $V_e(z \geq 0)$  presented in Eq. 2.1. This gives the first order correction to the energies [48]:

$$\Delta E_n \approx eE_\perp \langle n|z|n \rangle. \quad (2.11)$$

From this, we see that as the pressing field  $E_\perp$  increases, the transition frequencies into higher vertical states increases linearly [7, 49] and can be used to experimentally tune these levels over a wide range of frequencies [50].

### 2.1.2.2 Ensembles of electrons

A two-dimensional electron system (2DES) above liquid helium is an ideal system for investigating a variety of interesting properties of low dimensional electronic matter. To understand what makes the system so ideal, it is instructive to compare it to the 2DESs in solid state

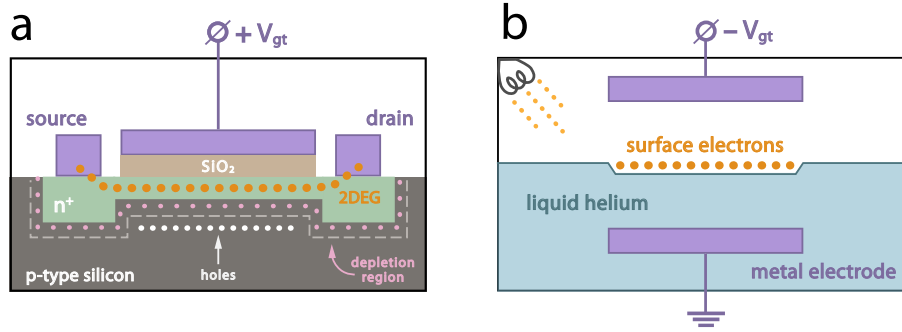


Figure 2.2: (a) Cross section of a  $p$ -type silicon MOSFET device. The central purple electrode is the gate (voltage  $V_{gt}$ ) and to the left and right are the source and drain electrodes which sit above the  $n$ -type source and drain regions. Beneath the gate electrode is the oxide layer, which is  $\text{SiO}_2$ . A depletion region (grey dashed lines and pink charges) forms around the  $pn$ -junction regions in the absence of an electric field ( $V_{gt} = 0$ ) [51]. Once  $V_{gt} > V_{th}$  and with a voltage across the source and drain electrodes, current will flow across the channel creating a 2DEG in this channel region. (b) Sketch of surface state electrons on liquid helium. A filament source (upper left corner) deposits the free electrons (orange) into the region between the parallel plate electrodes (purple). The electric field  $E_{\perp}$  is set by the gate voltage,  $V_{gt}$  (top electrode), which helps determine the density  $n_s$  of the surface electrons.

devices. In this modern age, you are likely carrying around billions of 2DESs in your pocket everyday, as computers rely on the physics of complementary metal-oxide semiconductor (CMOS) technology. Several things set a 2DES of electrons on helium apart from a 2DES in a semiconductor system such as those found in a metal-oxide-semiconductor field-effect transistor (MOSFET), however the key characteristics that make surface state electrons on helium a model system for understanding fundamental physical phenomena is their ability to exist freely in vacuum above the perfect dielectric that is superfluid helium. A typical solid state 2DES device is depicted in Fig. 2.2a. These 2DESs rely on fabrication reproducibility and are limited by their semiconductor and dielectric properties. In particular, defects in these devices will ultimately limit the 2DES mobility and the semiconductor-based architectures limit the electron-electron interaction strengths necessary for investigating the unique properties of strongly correlated electronic behavior such as Wigner crystallization [49].

Compared with its semiconductor counterpart in Fig. 2.2b, free electrons floating above the superfluid helium surface can host the lowest areal densities and highest mobilities of any 2DES. Here, a source filament (upper left hand corner) deposits electrons (orange) into the region between the two metal electrodes (purple). The applied gate electrode voltage ( $V_{gt}$ ) produces an electric field perpendicular to the helium surface ( $E_{\perp}$ ). When the source filament emits electrons via thermal emission, they will accumulate in the region between the two metal electrodes. If the filament is continuously depositing electrons, the electrons will continue to flow into the regions between the plates until the equilibrium condition is met – the total electric field above the surface electrons  $E_{\perp}^{\uparrow} = 0$ , i.e.  $E_{\perp} - en_s/2\epsilon_0 = 0$ . This equilibrium condition results in a gate voltage dependent equilibrium electron density:  $n_s = 2\epsilon_0 E_{\perp}/e$  [49].

An unconventional macroscopic analog of the standard n-channel field-effect transistor (FET), like the one shown in Fig. 2.2a, was demonstrated with electrons on helium by Nasyedkin *et al.* in 2018 [52]. This electron-on-helium FET device consists of three neighboring electrodes submerged in superfluid helium – a source ( $V_s$ ), gate ( $V_g$ ), and drain ( $V_d$ ) electrode – and operates as a FET by varying the gate voltage  $V_g$  and fixing  $V_s = V_d$ . In this configuration, the electron conductivity is controlled by  $V_g$ , as in the n-channel semiconductor FET. The foundation of this experiment is based on the techniques and architecture introduced by Sommer and Tanner [53], in which surface electrons on helium above three submerged electrodes provide an ideal platform to measure the mobility of electrons on helium. This mobility measurement architecture, referred to as the Sommer-Tanner technique, is discussed in further detail in Sec. 2.3.2

As in the case of a single electron, the 2DES will be bound to the surface with only vacuum and helium vapor atoms separating the two. Below 1 K, the surface electrons will

be in their vertical quantum ground state, where they form a non-degenerate – i.e. the wavefunctions of the electrons do not overlap – 2DES free to move in the plane parallel to the superfluid surface. The excited state occupation of the electrons and their energy above the surface will follow a Boltzmann distribution, whereby increasing the temperature will result in an increased probability ( $p_i$ ) of electrons populating some higher energy state  $\varepsilon_i$ , i.e.  $p_i \propto e^{-\varepsilon_i/k_B T}$  [54]. This non-degenerate 2DES creates the model system necessary for understanding non-degenerate electronic states of matter, strongly correlated electron behavior, collective excitations, and investigating free-floating electron on helium systems in 1D and quasi-1D geometries.

### 2.1.3 Correlations and Wigner crystallization

A defining property of surface state electrons on liquid helium is the strongly correlated nature of the electron system, which results from the strong Coulomb forces between electrons. Most solid state systems at the macroscopic level are insensitive to the effects of the repulsive forces of interacting electrons at the microscopic level, and the kinetic energy of the electrons dominate. For electrons on liquid helium, the microscopic influence of the strong Coulomb forces persist to the global level of the whole Coulomb liquid or solid. This long-range Coulomb interaction is an important characteristic of the electron on helium system and is the feature that has made it a model system for observing strongly-correlated phenomena like Wigner crystallization.

For the 2DES on helium, the liquid to solid phase transition can be understood via the plasma parameter, which describes the competition between the mean Coulomb potential energy  $\langle U \rangle$  and the mean kinetic energy  $\langle K \rangle$  of the electrons

$$\Gamma = \frac{\langle U \rangle}{\langle K \rangle}. \quad (2.12)$$

In general, for a 2DES these energies are given by

$$\langle U \rangle = \frac{e^2}{4\pi\epsilon_0 r_0} = e^2 \sqrt{\pi n_s} \quad (2.13)$$

$$\langle K \rangle = \frac{1}{\pi n_s} \int_0^\infty \varepsilon \nu(\varepsilon) f(\varepsilon) d\varepsilon \quad (2.14)$$

where  $r_0$  is the interelectron spacing, which is related to the areal electron density  $n_s$  by  $r_0 = 1/\sqrt{\pi n_s}$ ,  $\nu(\varepsilon) = m_e/\pi\hbar^2$  is the density of states for electron energy  $\varepsilon$ , and  $f(\varepsilon) = [e^{(\varepsilon-\mu)/T} + 1]^{-1}$  is the Fermi-Dirac distribution function with chemical potential  $\mu$  [49]. Here, the average kinetic energy of electrons with the energy spectrum  $\varepsilon_k \propto k^2$  allows us rewrite the kinetic energy in terms of the Fermi energy,  $E_F = \pi\hbar^2 n_s/m_e$ , and  $\langle K \rangle = E_F/2$ . Further, the characteristic energies of the electron system can be represented by the dimensionless parameter,  $r_s = r_0/a_B$ , where  $a_B = \hbar^2/m_e e^2$  is the Bohr radius. Utilizing the Rydberg unit of energy,  $\text{Ry} = m_e e^4/2\hbar^2 \simeq 13.6$  eV, and substituting these into the above equations for the average kinetic and potential energy, gives

$$\langle U \rangle = \frac{2}{r_s} [\text{Ry}] \quad (2.15)$$

$$\langle K \rangle = \frac{\pi\hbar^2 n_s}{2m} = \frac{1}{r_s^2} [\text{Ry}] \quad (2.16)$$

Semiconductor systems typically have densities in the range  $n_s \simeq 10^{14} - 10^{15} \text{ m}^{-2}$  and

are studied at experimental temperatures on the order of  $T \simeq 0.5$  K. In these systems, that gives the Fermi-degeneracy parameter  $k_B T/E_F < 1$ , meaning the system cannot be treated with the classical Maxwell-Boltzmann statistics, and in the zero temperature limit, one must consider the plasma parameter for the degenerate 2DES:  $\Gamma = 2r_s$ . If we replace  $m_e$  with the effective mass  $m^*$  for GaAs ( $m^* \simeq 0.07m_e$ ) and  $e \rightarrow e/\sqrt{\epsilon}$  ( $\epsilon_{\text{GaAs}} = 12.5$ ) to take into account the dielectric constant of the surrounding semiconductor medium, the Coulomb energy is decreased while the kinetic energy is increased, making the plasma parameter ratio much smaller and the crystallization condition relatively difficult to realize [29, 49].

In contrast, typical densities in electrons on helium are within the range of  $n_s \simeq 10^9 - 10^{12} \text{ m}^{-2}$ . For standard experimental temperatures ( $T = 0.01 \text{ K} - 1 \text{ K}$ ), the Fermi-degeneracy parameter  $k_B T/E_F \gg 1$  and interelectron distances  $n_s^{-1/2}$  are much larger than the electron thermal deBroglie wavelength  $\lambda_{\text{th}} = 2\pi\hbar/\sqrt{2m_e k_B T}$ . Thus, electrons on helium are a quantum non-degenerate system. In this case, the mean kinetic energy is simply  $\langle K \rangle = k_B T$  and the plasma parameter for the non-degenerate 2DES takes the form:

$$\Gamma = \frac{1}{4\pi\epsilon_0} \frac{e^2 \sqrt{\pi n_s}}{k_B T} \quad (2.17)$$

When  $\Gamma \ll 1$  the Coulomb interaction is negligible and the system takes a form similar to that of an ideal gas of fermions. For the range  $1 < \Gamma < 100$ , in the low density high temperature limit, the electrons behave like a correlated electron liquid, whereas in the high density low temperature limit ( $\Gamma > 100$ ), the Coulomb potential energy dominates and the strong correlations between electrons drive the system into a crystalline phase, i.e. a Wigner solid [54]. The first experimental realization of the classical Wigner solid was in electrons on helium, where it was found that the crystallization condition was  $\Gamma \gtrsim 137$  for electron areal

densities in the range of  $n_s \simeq 3 \times 10^{12} \text{ m}^{-2} - 8 \times 10^{12} \text{ m}^{-2}$  at temperatures  $T = 0.35 \text{ K}$  to  $0.65 \text{ K}$  [7]. As we will discuss in the next chapter, various techniques have been implemented to detect the formation of this 2D electron crystal on helium, including measurements of the electron conductivity and through coupled electron-helium surface modes (i.e. ripplons). The extremely high mobilities together with the formation of a relatively low density Wigner crystal, has motivated efforts to utilize these trapped electron systems for quantum computing.

## 2.2 Plasmons and collective phenomena

Plasma is the often forgotten fourth state of classical matter<sup>2</sup> – typically associated with things like lightning, hot flames of fire, or plasma televisions – which are conducting gas-like states of unbound electrons and ions that exhibit long-range collective motion. The characteristic long-range collective motion of plasmas is the result of Coulomb interactions, which can result in a compression and expansion of the average interparticle distances. In the case in which the thermal motion of electrons can be ignored, a three-dimensional electron plasma can sustain charge density oscillations at the plasma frequency

$$\omega_p = \sqrt{\frac{n_e e^2}{m_e \epsilon_0}}, \quad (2.18)$$

where  $n_e$  is the volume density of electrons and  $m_e$  is the electron mass (see Sec. 2.3.1.1 for how this arises from the Drude model).

Plasma oscillations are a typical collective excitation found in electrons on helium, however other collective phenomena also exist. Before discussing how these charge density waves

---

<sup>2</sup>Sorry, plasma.

(i.e. plasmons) arise in electrons on helium, we briefly discuss the other collective phenomena inherent to electrons on helium.

### 2.2.1 Collective phenomena in electrons on helium

Collective phenomena in electrons on helium are the result of the highly correlated nature of the electrons, facilitated by the long-range Coulomb interaction. Examples of the collective excitations that result from this long-range order include phonon modes in the electron crystal that arise from the propagation of shear waves [55], resonantly excited incompressible electronic states [56], as well as coupled phonon-ripplon modes [7, 57, 58].

In the presence of a magnetic field, electron dynamics will exhibit cyclotron motion and the formation of Landau levels [24]. This leads to magnetoresistance [31, 59, 60] as well as bulk and edge magnetoplasmons – a dynamical manifestation of the Hall effect in electrons on helium – which have been widely studied and observed in both two-dimensional [30, 35, 61] and quasi-one dimensional electrons on helium systems [40].

Other collective phenomena of the electron system include hybrid modes coupling the dynamics of multiple degrees of freedom, including Rydberg level excitations coupled to the electron cyclotron motion [41, 42] as well as electron ensembles coupled to piezoelectric surface acoustic waves [43]. Additionally, ensembles of electrons on helium have been strongly coupled to three-dimensional microwave cavities to study cyclotron resonance [37, 44] and integrated into hybrid circuits in which an electron ensemble is placed above a planar microwave resonator [39].

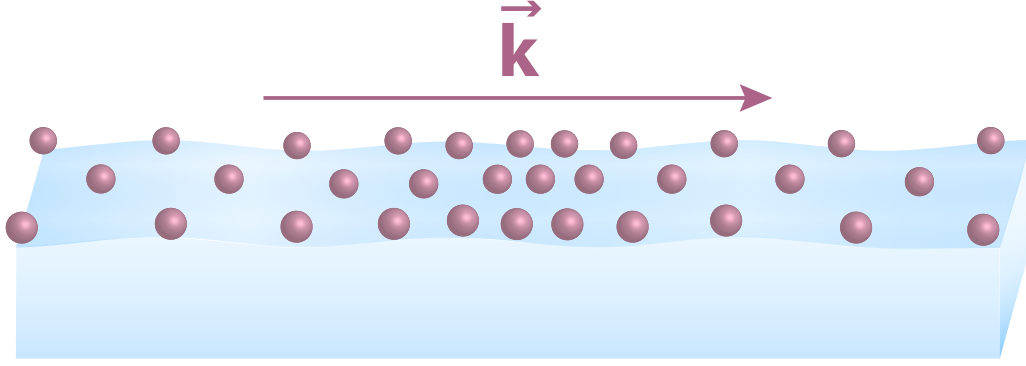


Figure 2.3: Simple illustration of a longitudinal charge density oscillation, i.e. plasmon, of electrons on superfluid helium, with wavevector  $\vec{k}$ . Electrons (pink) hover above the surface (blue), where here the charge density is greatest in the center.

### 2.2.2 Plasmons in electrons on helium

In electrons on helium, plasmons are simply the charge density oscillation of the floating charges, as depicted in Fig. 2.3. Two-dimensional plasmons in electrons on helium were first observed in 1975 by Grimes and Adams [34] in a frequency range of  $\sim 20$  MHz – 250 MHz. The general form of the plasmon dispersion relation in the long-wavelength limit (i.e. small wavevector  $k$ ,  $kv_{\text{th}}/\omega_p \ll 1$ ) and small damping ( $\omega_p\tau \gg 1$ ) takes the form [34, 62]

$$\omega_{p0}^2 = \frac{2\pi n_s e^2}{m_e} \left( 1 + \frac{i}{\omega_{p0}\tau} \right), \quad (2.19)$$

where  $v_{\text{th}}$  is the electron thermal velocity and  $\tau$  is a phenomenological relaxation time. In the geometry used by Grimes and Adams, the plasmon dispersion relation is modified to account for the screening. The modified form of Eq. 2.19 takes into account the finite height  $h$  of their sample cell, in which image charges in the top and bottom plate electrodes will screen the Coulomb restoring force and lower the long-wavelength plasmon frequency. This screened two-dimensional plasmon dispersion relation in the geometry of Grimes and Adams

$\omega_p$  is

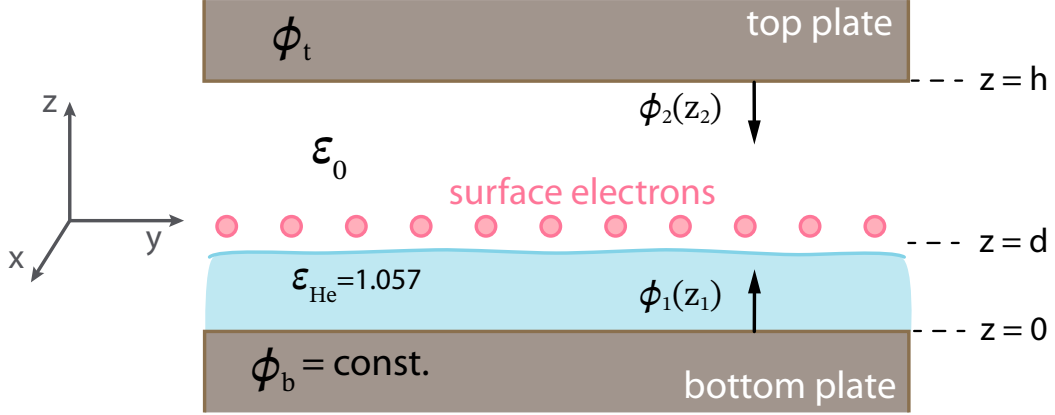


Figure 2.4: Cross sectional illustration of the set up used by the Grimes and Adams to observe 2D plasmons in electrons on helium. The system consists of top and bottom plate electrodes, which induce potentials above ( $\phi_2(z_2)$ ) and below ( $\phi_1(z_1)$ ) surface electrons (pink).

$$\omega_p^2 = \frac{n_s e^2}{2\epsilon_0 m_e} \left[ q_x^2 F(q_x) + q_y^2 F(q_y) \right]^{1/2}, \quad (2.20)$$

where the screening factor is given by

$$F(q_i) = \frac{2 \sinh [q_i d] \sinh [q_i (h - d)]}{\sinh (q_i h)}, \quad (2.21)$$

where  $d$  is the helium depth,  $h$  is the height of the cell, and  $q_x = m\pi/W$  and  $q_y = n\pi/L$  are the wave numbers for the  $m$  and  $n$  modes corresponding to the width  $W$  and length  $L$  of the cell, respectively.

### 2.2.2.1 Two-dimensional screened plasmon dispersion relation

To derive this two-dimensional screened plasmon dispersion relation, we consider the cross section depicted in Fig. 2.4. Neglecting any dissipation, we begin with the continuity equation, an equation of motion to describe the electron motion in a given potential, and the Poisson equation for the 2D charge sheet, respectively, to describe the system:

$$\frac{\partial n(\mathbf{r}, t)}{\partial t} + \nabla \cdot [n(\mathbf{r}, t)\mathbf{v}(\mathbf{r}, t)] = 0 \quad (2.22)$$

$$\frac{\partial \mathbf{v}(\mathbf{r}, t)}{\partial t} + (\mathbf{v}(\mathbf{r}, t) \cdot \nabla) \mathbf{v}(\mathbf{r}, t) = -\frac{e}{m_e} \nabla \phi(\mathbf{r}, t) \quad (2.23)$$

$$\nabla^2 \phi(\mathbf{r}, t) = -\frac{e}{\varepsilon_0} n(\mathbf{r}, t) \delta(z - d). \quad (2.24)$$

Here,  $n(\mathbf{r}, t)$  is the  $xy$ -position dependent electron density  $n(\mathbf{r}, t)$ , where the electron position is represented by the vector  $\mathbf{r}(x, y)$ ;  $\mathbf{v}(\mathbf{r}, t)$  is the electron velocity; and  $\phi(\mathbf{r}, t)$  is the total electrostatic potential. For the Poisson equation (Eq. 2.24), we require the term  $\delta(z - d)$ , as charge is only present at  $z = d$  where the electrons exist<sup>3</sup>. At all other points in the space between the electrodes, the Laplace equation will hold ( $\nabla^2 \phi = 0$ ). For the remainder of the derivation, we consider the system in cylindrical coordinates  $(r, \theta, z)$  due to the symmetry about the  $z$ -axis. The derivation for the dispersion relation in Eq. 2.20 consists of three main steps:

1. Solving for the electric potential in the two regions above ( $\phi_2(z_2)$ ) and below ( $\phi_1(z_1)$ ) the surface electrons.
2. Employing the appropriate assumptions and boundary conditions at the interface of the two dielectric media  $\varepsilon_0$  and  $\varepsilon_{\text{He}}$  for the two potentials  $\phi_2(z_2)$  and  $\phi_1(z_1)$ .
3. Imposing the time varying external electric field  $\mathbf{E} = \text{Re}(E_r e^{-i\omega t}) \hat{r}$  (of amplitude  $E_r$ ) on the charge layer, which will excite the plasmon modes, and solving the continuity equation and equation of motion with the potentials obtained from (1) and (2).

---

<sup>3</sup>Here we have made the approximation that the height of the electrons and the height of the helium above the bottom electrode are equal.

**(1) Solving for the potentials above and below the electron sheet.** The Laplace equation we must solve, in cylindrical coordinates, is

$$\nabla^2\phi(r, \theta, z) = \frac{1}{r} \frac{\partial}{\partial r} \left( r \frac{\partial \phi}{\partial r} \right) + \frac{1}{r^2} \frac{\partial^2 \phi}{\partial \theta^2} + \frac{\partial^2 \phi}{\partial z^2} = 0. \quad (2.25)$$

If we let  $\phi(r, \theta, z) \equiv R(r)T(\theta)S(z)$ , we get the separated equations and corresponding solutions,

$$\frac{\partial^2 S(z)}{\partial z^2} - q^2 S(z) = 0 \rightarrow S(z) = S_0 \sinh(qz) \quad (2.26)$$

$$\frac{\partial^2 T(\theta)}{\partial \theta^2} + \beta^2 T(\theta) = 0 \rightarrow T(\theta) = A \cos(\beta\theta) + B \sin(\beta\theta) \quad (2.27)$$

$$\frac{\partial^2 R(r)}{\partial r^2} + \frac{1}{r} \frac{\partial R(r)}{\partial r} + (q^2 - \beta^2/r^2)R(r) = 0 \rightarrow R(r) = R_0 J_\beta(qr) \quad (2.28)$$

The solution for  $S(z)$  has the arbitrary constant amplitude  $S_0$  and separation variable  $q$ , with dependence on the  $\sinh(qz)$  from the fact that we require  $\phi(\sinh(qz)) \rightarrow 0$  as it approaches the electron sheet. The solution for  $T(\theta)$  has the arbitrary constant amplitudes  $A$  and  $B$  and has separation constant  $\beta$ . The separation constant  $\beta$  must be single-valued for integer multiples of  $(\theta + 2\pi)$ , with  $\beta = 0, 1, 2, \dots$ . The solution for  $R(r)$  has the arbitrary constant amplitude  $R_0$  and depends on both the  $z$  and  $\theta$  separation constants,  $q$  and  $\beta$ . The radial part is just the solution to the Bessel equation with the Bessel function of the first kind  $J_\beta(qr)$  [63]. Because of the radial component dependence on the angular and axial components, we can absorb constants from the radial ( $R_0$ ) and axial ( $S_0$ ) solutions into the constants ( $A$  and  $B$ ) for the angular solution, which we will solve for with the appropriate boundary conditions in the next part. Then, the analytical solution for the potential takes the form:

$$\phi(r, \theta, z) = \sum_{\beta=0}^{\infty} \sum_{n=1}^{\infty} J_{\beta}(q_n r) \sinh(q_n z) \left[ A_n \sin(\beta\theta) + B_n \cos(\beta\theta) \right] \quad (2.29)$$

and because we have azimuthal symmetry, there will be no  $\theta$  dependence in the potential  $\phi$ , which means we have  $\beta = 0$ . The index  $n$  corresponds to the integer modes that arise in the solution for  $S(z)$ . Finally, this allows us to write the fully reduced analytical form for the potential:

$$\phi(r, z) = \sum_{n=1}^{\infty} C_n J_0(q_n r) \sinh(q_n z). \quad (2.30)$$

Here, we have introduced the constant  $C_n$  to account for all absorbed constants above. We can now write the potentials above and below the electron sheet, such that  $z_1 = z$ ,  $z_2 = (h - z_1)$ , and

$$\phi_1(r, z, t) = \phi_b + \sum_{n=1}^{\infty} C_{1n} J_0(q_n r) \sinh(q_n z) e^{-i\omega t} \quad (2.31)$$

$$\phi_2(r, z, t) = \phi_t + \sum_{n=1}^{\infty} C_{2n} J_0(q_n r) \sinh(q_n (h - z)) e^{-i\omega t}. \quad (2.32)$$

**(2) Employing assumptions and corresponding boundary conditions.** There are two boundary conditions we must consider at the interface  $z = d$ : (I) the potential must be continuous across the interface, i.e.  $\phi_1(d) = \phi_2(d)$  and (II) the divergence of the electric displacement field  $\nabla \cdot \mathbf{D} = \rho$ , which describes how the potential changes across the two discontinuous media  $\varepsilon_0$  and  $\varepsilon_{\text{He}}$  for the free charge density  $\rho$ .

For (I) at  $z = d$ , Eq. 2.31 is set equal to Eq. 2.31 with  $\phi_1(r, d, t) = \phi_2(r, d, t)$ . This equation is satisfied when  $\phi_t$  has a static component that cancels  $\phi_b$  and also a dynamic

component that provides information about the motion of the charges at the interface. For (II) we start with  $\nabla \cdot \mathbf{D} = \rho$ , where we consider a volume element  $V$  at the interface between vacuum and the helium. Integrating over the volume element  $V$  we have

$$\int_V \nabla \cdot \mathbf{D} dV = \int_S \mathbf{D} \cdot \hat{n} dS = \int_V \rho dV = \int_S n_s e dS, \quad (2.33)$$

where  $\hat{n}$  is a normal component at the interface, which gives the difference in the electric displacement  $D_{2z} - D_{1z} = n_s e$ . Since  $\mathbf{D} = \varepsilon \mathbf{E} = -\varepsilon \nabla \phi$ , at  $z = d$  we have:

$$-\varepsilon(\nabla \phi_2 - \nabla \phi_1) = \varepsilon \left( \frac{\partial \phi_1}{\partial z} - \frac{\partial \phi_2}{\partial z} \right) = n_s e. \quad (2.34)$$

**(3) Solving the continuity equation and equation of motion with an external field  $\mathbf{E}(\omega, t)$ .** To consider the dynamical response of the electron system, we impose a time-varying external field in the plane of the electron sheet  $\mathbf{E}(\omega, t) = \text{Re}(E_r e^{-i\omega t}) \hat{r}$ . This will cause the charge density to vary slightly from its equilibrium density  $n_0(\mathbf{r}, t)$  as the radial driving field pushes the charges around,

$$n(\mathbf{r}, t) = n_0 + \delta n(\mathbf{r}, t), \quad (2.35)$$

where  $\delta n(\mathbf{r}, t)$  is the charge density variation from its equilibrium configuration due to  $\mathbf{E}(\omega, t)$ . The velocity of the charges in equilibrium  $\mathbf{v}(\mathbf{r}, t) = 0$  will also be modified by the applied electric field, where  $\mathbf{v}(\mathbf{r}, t) = \delta v_r(\mathbf{r}, t) \cdot \hat{r}$ . Because we are in the vertical ground state and we have azimuthal symmetry,  $\delta v_z = 0$  and  $\delta v_\theta = 0$ , respectively.

We can now rewrite the equations we need to describe the plasma motion:

$$-i\omega\delta n + n_0 \frac{1}{r} \frac{\partial}{\partial r} (r\partial v_r) = 0 \quad (2.36)$$

$$i\omega\partial v_r = \frac{e}{m_e} \frac{\partial}{\partial r} \phi(\mathbf{r}, t). \quad (2.37)$$

Next, we plug Eq. 2.31 into Eq. 2.37 with  $z = d$  at the interface, then impose that at the edge ( $r = R$ ) of the charge sheet,  $\delta v_r(R, d, t) = 0$ , which means that  $J_1(q_n R) = 0$ . From this, we get the three main equations for the potential ( $\phi$ ), velocity change ( $\delta\mathbf{v}$ ), and change in charge density ( $\delta n$ ) at the interface:

$$\phi_b + \sum_{n=1}^{\infty} C_{1n} J_0(q_n r) \sinh(q_n d) e^{-i\omega t} = \phi_t + \sum_{n=1}^{\infty} C_{2n} J_0(q_n r) \sinh(q_n (h - d)) e^{-i\omega t} \quad (2.38)$$

$$\delta v_r(r, d, t) = \sum_{n=1}^{\infty} -\frac{C_{1n} q_n e}{i\omega m_e} J_1(q_n r) \sinh(q_n d) e^{-i\omega t} \quad (2.39)$$

$$\delta n(r, d, t) = \sum_{n=1}^{\infty} n_0 \frac{C_{1n} q_n^2 e}{i\omega^2 m_e} J_0(q_n r) \sinh(q_n d) e^{-i\omega t}. \quad (2.40)$$

Here, we have used the identity  $\frac{\partial}{\partial r} [J_0(q_n r)] = -J_1(q_n r)$  in Eq. 2.39.

Now we can obtain the plasmon dispersion relation using the equations above. From Eq. 2.38, we consider  $r$  over the interval  $0 \leq r \leq R$  and use the Fourier-Bessel series identity<sup>4</sup> to get

$$C_{1n} \sinh(q_n d) - C_{2n} \sinh(q_n (h - d)) = \frac{2e^{i\omega t}}{R^2 J_0^2(q_n R)} \int_0^R r J_0(q_n r) dr (\phi_t - \phi_b). \quad (2.41)$$

---

<sup>4</sup> $f(r) = \sum_{n=1}^{\infty} A_{\nu n} J_{\nu}(x_{\nu n} r/a)$  with  $A_{\nu n} = \frac{2}{a^2 J_{\nu+1}^2(x_{\nu n})} \int_0^a r f(r) J_{\nu}(x_{\nu n} r/a) dr$  over  $0 \leq r \leq a$  [63]

The integral on the right hand side is solved using the Bessel function identity

$$\int_0^R r dr J_0(q_n r) = \frac{r}{q_n} J_1(q_n r) \Big|_0^R = 0, \quad (2.42)$$

which goes to zero due to the same assumption we set for Eqs. 2.38, 2.39, and 2.40 at the edge of the charge sheet ( $\delta v_r(R, d, t) = 0$ ). Then, the relationship for the coefficients reduces to  $\frac{C_{2n}}{C_{1n}} = \frac{\sinh(q_n d)}{\sinh(q_n(h-d))}$ . Next, we impose the boundary condition at the interface from Eq. 2.34 and Eq. 2.40 in Eq. 2.35 to solve for  $\omega$ , which takes the form

$$\omega^2 = \frac{n_0 e^2 q_n}{2\varepsilon_0 \varepsilon_{\text{He}} m_e} \frac{\sinh[q_n d] \sinh[q_n(h-d)]}{\sinh[q_n h] + (1 - \varepsilon_{\text{He}}) \cosh[q_n d] \sinh[q_n(h-d)]}. \quad (2.43)$$

We can neglect the second term in the denominator because  $(1 - \varepsilon_{\text{He}}) \ll 1$  and we get the reduced form of the 2D screened plasmon dispersion relation:

$$\omega^2 = \frac{e^2 n_s}{2m_e \varepsilon_0 \varepsilon_{\text{He}}} q_n F(q_n), \quad F(q_n) = \frac{\sinh[q_n d] \sinh[q_n(h-d)]}{\sinh[q_n h]}. \quad (2.44)$$

This form of the dispersion can be rewritten in terms of rectangular coordinates by recognizing that the radially dependent part of the equation arises in the wavenumber  $q_n$  and in the screening parameter  $F(q_n)$ , for a given mode number  $n$ . For a rectangular geometry, the wavenumber  $q_n$  in cylindrical coordinates is simply the magnitude of the in-plane wavevector  $\mathbf{q} = (q_x, q_y)$  in rectangular coordinates, i.e.  $q = \sqrt{q_x^2 + q_y^2}$ . This means we now have two mode numbers,  $n$  and  $m$ , in the rectangular geometry, such that  $q_x = n\pi/L$  and  $q_y = m\pi/W$ , where  $L$  is the length in the  $x$  and  $W$  is the width across the  $y$ . Putting this all together, we finally arrive at the two-dimensional screened plasmon dispersion relation from Eq. 2.20:

$$\omega_p^2 = \frac{n_s e^2}{2\epsilon_0 m_e} \left[ q_x^2 F(q_x) + q_y^2 F(q_y) \right]^{1/2}, \quad F(q_i) = \frac{\sinh [q_i d] \sinh [q_i (h - d)]}{\sinh [q_i h]}, \quad (2.45)$$

where we have used the subscript  $i$  in the screening factor definition to indicate the  $i = x$  or  $i = y$  wavenumber.

## 2.3 Transport properties of electrons on bulk helium

Transport measurements of electrons on helium provide a highly sensitive tool for measuring the electron system conductivity, enabling a way for detecting various phenomena in low-dimensional electron systems. In particular, transport measurements have been utilized to reveal dynamical ordering of two-dimensional [11, 64] and quasi-one-dimensional electron chains [65, 66], as well as the non-equilibrium and nonlinear response of the strongly correlated low-dimensional electron system in the presence of high-frequency perturbing fields [27, 28, 48, 67, 68]. Electron conductivity measurements also reveal the essential role that scatterers play in the electron mobility  $\mu$ , i.e. how easily the electron system moves along the helium surface when pushed by an external force. As you will see in Chapter 3, transport measurements also allow us to detect microwave frequency plasmon modes due to a resonant response in the conductivity of the electron system when excited by a microwave drive.

### 2.3.1 Mobility

The highest mobility of any 2DES is found in electrons on helium, where mobilities as high as  $10^8$  cm<sup>2</sup>/Vs [45] have been recorded. The current state-of-the-art mobilities in ultra-high-

quality GaAs devices have just reached  $\sim 50 \times 10^6 \text{ cm}^2/\text{Vs}$  [69]. The quality or “cleanliness” of a 2DES is oftentimes parameterized by the mobility  $\mu$ , which is limited by the various defects and scatters in the surrounding medium of the 2DES. The mobility of electrons on helium is limited by two main scatterers – helium vapor atoms and helium surface capillary waves (ripples). The mobility of electrons on helium is described by the Drude model, in which the mobility is a function of the average time  $\tau$  between scattering events.

### 2.3.1.1 The Drude model

#### *The dc Drude model*

For a system of electrons on helium, the Drude model describes the mobility and conductivity of the electrons moving with the average velocity  $\mathbf{v} \equiv \langle \mathbf{v} \rangle$ . The equation of motion for electrons accelerated by an external driving force  $\mathbf{F}$  is given by:

$$m_e \frac{d\mathbf{v}}{dt} = -m_e \frac{\mathbf{v}}{\tau} - e\mathbf{E} \quad (2.46)$$

where  $\tau$  is the relaxation time and  $\mathbf{F} = -e\mathbf{E}$  is the Lorentz force for the case of  $\mathbf{B} = 0$ . For the dc Drude model, we consider a constant electric field  $\mathbf{E}$  and the resulting average electron velocity will be constant. In this case, Eq. 2.46 reduces to

$$\mathbf{v} = \frac{-e\tau}{m_e} \mathbf{E} = -|\mu| \mathbf{E}, \quad (2.47)$$

where the mobility is  $\mu = e\tau/m_e$ . For completeness, we can substitute this steady-state solution for the average velocity into the current density [70],

$$\mathbf{j} = -en\mathbf{v} = \frac{ne^2\tau}{m_e} \mathbf{E} = \sigma_0 \mathbf{E}. \quad (2.48)$$

Here, the dc conductivity is  $\sigma_0 = ne^2\tau/m_e = ne\mu$ , which is a function of the mobility and the density of electrons  $n$ .

### ***The ac Drude model***

In the case where a time-dependent electric field  $\mathbf{E}(t)$  is present, the equation of motion for an electron is  $m_e d\mathbf{v}/dt = -m_e\mathbf{v}(t)/\tau - e\mathbf{E}(t)$  and the steady-state solution for the electron momentum will be of the form  $\mathbf{p}(t) = \text{Re}(\mathbf{p}(\omega)e^{-i\omega t})$ <sup>5</sup>. From this, we get the frequency-dependent current density [70]:

$$\mathbf{j}(\omega) = -\frac{en\mathbf{p}(\omega)}{m_e} = \frac{(e^2n/m_e)\mathbf{E}(\omega)}{(1/\tau) - i\omega}. \quad (2.49)$$

The current density can be written as  $\mathbf{j}(\omega) = \sigma(\omega)\mathbf{E}(\omega)$ , where the ac conductivity  $\sigma(\omega)$  is

$$\sigma(\omega) = \frac{\sigma_0}{1 - i\omega\tau}, \quad \sigma_0 = \frac{ne^2\tau}{m_e} \quad (2.50)$$

which is as a function of frequency and depends on the dc conductivity  $\sigma_0$  introduced in Eq. 2.48. However, this analysis assumes that at any given time  $t$ , the force acting on each electron is the same. By taking into account the spatially-dependent field  $\mathbf{E}(\mathbf{r}, t)$ , and solving Maxwell's equations for the the current density  $\mathbf{j}(\mathbf{r}, \omega) = \sigma(\omega)\mathbf{E}(\mathbf{r}, \omega)$ , we get [70]

$$-\nabla^2\mathbf{E}(\mathbf{r}) = \frac{\omega^2}{c^2}\left(1 + \frac{i\sigma(\omega)}{\omega\varepsilon_0}\right)\mathbf{E}(\mathbf{r}) \quad (2.51)$$

where we have the spatially dependent electric field amplitude  $\mathbf{E}(\mathbf{r})$  and the ac conductivity

---

<sup>5</sup>For a field  $\mathbf{E}(t) = \mathbf{E}(\omega)e^{-i\omega t}$  which oscillates at frequency  $\omega$ , the steady-state solution will have the form  $\mathbf{p}(t) = \mathbf{p}(\omega)e^{-i\omega t}$ . Plugging this into the equation of motion,  $\frac{d\mathbf{p}(t)}{dt} + \frac{1}{\tau}\mathbf{p}(t) = -e\mathbf{E}(t)$ , we get  $(-i\omega + i/\tau)\mathbf{p}(\omega) = -e\mathbf{E}(\omega)$ .

$\sigma(\omega)$ . Equation 2.51 is the wave equation with a complex dielectric constant

$$\varepsilon(\omega) = 1 + \frac{i\sigma}{\varepsilon_0\omega} = 1 + \frac{ine^2\tau}{(1 - i\omega\tau)\varepsilon_0m_e\omega}. \quad (2.52)$$

At sufficiently high frequencies ( $\omega\tau \gg 1$ ), the dielectric constant becomes

$$\varepsilon(\omega) = 1 - \frac{ne^2}{\varepsilon_0m_e\omega^2} = 1 - \frac{\omega_p^2}{\omega^2}, \quad (2.53)$$

where we have defined  $\omega_p^2 \equiv ne^2/\varepsilon_0m_e$ , which is just the plasma frequency term from Eq. 2.18 [70]!

### 2.3.1.2 Scatterers: Vapor atoms and riplons

Electrons on helium have the highest mobilities in condensed matter systems because the electrons have only two primary scatterers: helium vapor atoms and liquid helium surface capillary waves (riplons) [71, 72]. In transport experiments, these scatterers limit the measured electron mobility and conductivity. Phonons in the superfluid helium bulk also play a role in electron energy relaxation in systems of small numbers of electrons, however this energy relaxation mechanism has only weak consequences for the relevant 2DES transport here [57, 73–75].

The total scattering rate  $\tau^{-1}$  for electrons on helium is given by:

$$\frac{1}{\tau(\epsilon_k)} = \frac{1}{\tau_v} + \frac{1}{\tau_r(\epsilon_k)}, \quad (2.54)$$

where  $\tau_v$  is the relaxation time for electron-vapor atom scattering and  $\tau_r(\epsilon_k)$  is the relaxation time associated with electron-riplon scattering, which depend on the electron kinetic energy

$\epsilon_k$ .

The contribution of vapor atom scattering is a function of temperature, where the vapor density of the helium atoms is [48]

$$n_v = \left[ \frac{m_{\text{He}} k_{\text{B}} T}{2\pi \hbar^2} \right]^{3/2} e^{-T_v/T}. \quad (2.55)$$

Here,  $m_{\text{He}}$  is the mass of the helium atom and  $T_v = L_v/k_{\text{B}} = 7.17$  K is the evaporation constant for liquid helium<sup>6</sup>. The vapor atom scattering rate is [48]

$$\frac{1}{\tau_v} = \frac{3\pi \hbar \sigma_s n_v}{8m_e a_E}, \quad (2.56)$$

where  $\sigma_s = 4.98 \times 10^{-20}$  m<sup>2</sup> is the helium atom scattering cross section and  $a_E$  is the effective electron Bohr radius in the presence of an external perpendicular holding field  $E_{\perp}$ <sup>7</sup>. We can write the vapor atom scattering dependent mobility in terms of the temperature-dependent vapor atom scattering rate [77]:

$$\mu_v = \frac{e\tau_v}{m_e} = \frac{8ea_E}{3\pi \hbar \sigma_s n_v}. \quad (2.57)$$

Once vapor atom scattering becomes negligible ( $T < 0.7$  K), the contributions of ripplon scattering becomes dominant. Ripplons are surface phonons of the superfluid helium. In the

---

<sup>6</sup>The evaporation constant comes from the latent heat per atom of liquid helium  $L_v = L_e/N_A$ , where  $L_e = 20.5$  J/mol [76] is the latent heat of evaporation for liquid helium and  $N_A = 6.022 \times 10^{23}$  is Avogadro's number.

<sup>7</sup>This is calculated by solving the 1D Schrödinger (Eq. 2.6) equation and replacing the potential term  $-\Lambda/z$  with the potential in Eq. 2.1. Saitoh gives this parameter  $a_E$  in terms of the effective Bohr radius  $a$  (from Eq. 2.9):  $\frac{a_E}{a} = \frac{4}{3\lambda_E} \sinh\left(\frac{1}{3} \operatorname{arcsinh}\left(\frac{9\lambda_E}{4}\right)\right)$  [48]. Here  $\lambda_E = \sqrt{E_{\perp}/E_C}$  parameterizes the strength of the holding field  $E_{\perp}$  with respect to the characteristic field  $E_C = \hbar^2/2em_e a^3$ .

short wavelength limit<sup>8</sup>, for helium films with thickness greater than 100 nm, the ripplon dispersion relation is given by [49, 54]

$$\omega_r = \sqrt{\frac{\alpha}{\rho}} q^3, \quad (2.58)$$

where  $\alpha = 3.7 \times 10^{-4}$  N/m is the surface tension of the helium,  $\rho \simeq 145$  kg/m<sup>3</sup> is the liquid helium density, and  $q$  is the ripplon wave vector [78]. We can look at the energy of the riplons taking part in electron scattering by considering wave numbers  $q$  that are on the order of the thermal de Broglie electron wave number,  $q = \sqrt{m_e k_B T} / \hbar \sim k_T$  [49], and

$$\hbar\omega_r = \sqrt{\frac{\alpha}{\rho\hbar}} [8m_e k_B T]^{3/4}. \quad (2.59)$$

From Eq. 2.59, we find that  $\hbar\omega_r \ll k_B T$  (for  $T < 0.7$  K), which means the electron-riplon scattering will be in the long wavelength limit. Following the treatment in Ref. [48], the electron-riplon scattering rate is

$$\begin{aligned} \frac{1}{\tau_r(\epsilon_k)} = \frac{T}{4\hbar\alpha a^2} & \left[ \frac{(aeE_\perp)^2}{\epsilon_k} + 2eE_\perp a [\ln(16E_f/\epsilon_k) - 3] \right. \\ & \left. + \frac{3\epsilon_k}{2} [(\ln(16E_f/\epsilon_k) - 19/6)^2 + (\pi^2/3 - 115/36)] \right], \end{aligned} \quad (2.60)$$

where  $\epsilon_k$  is the electron kinetic energy when the electron is in the ground Rydberg level,  $a$  is the effective Bohr radius given in Eq. 2.9 and  $E_f = \hbar^2/2m_e a_E$ . With  $E_\perp = 0$  and at low temperatures where electron-riplon scattering is dominant, the ripplon-limited collision time is on the order of

---

<sup>8</sup>The short wavelength limit here refers to when the surface tension is the primary restoring force and the gravity term ( $gq$ ) in the full dispersion is negligible [49, 54].

$$\tau_r(k_B T) \sim \frac{8\hbar\alpha a^2}{3k_B^2 T^2} \left[ \ln \left( \frac{0.67\hbar^2}{2m_e a^2 T} \right) \right]^{-2}. \quad (2.61)$$

In the limit of a strong holding field ( $eE_\perp \gg k_B T/z$ ), the collision rate has the following energy dependence:

$$\frac{1}{\tau_r(\epsilon_k)} = \frac{k_B T (eE_\perp)^2}{4\hbar\alpha\epsilon_k}, \quad (2.62)$$

which can be used to obtain the holding field dependent average collision time for riplons  $\langle \tau_r(\epsilon_k) \rangle = 8\hbar\alpha/(eE_\perp)^2$ , and the ripplon-limited mobility [49]

$$\mu_r = \frac{e}{m_e} \langle \tau_r(\epsilon_k) \rangle = \frac{8\hbar\alpha}{em_e E_\perp^2}. \quad (2.63)$$

### 2.3.2 Sommer-Tanner transport measurements

The first mobility measurement of electrons on helium was performed by Sommer and Tanner in 1971 [53]. This measurement technique, now known as the Sommer-Tanner technique, has become a standard for electron on helium transport experiments. A sketch of the original Sommer-Tanner measurement setup is shown in Fig. 2.5, with its transmission line equivalent circuit. Three electrodes (labeled (1), (2), and (3); colored green), each of length  $\ell$ , are submerged in the liquid helium, a depth  $\hbar$  below the surface. In these measurements, electrons were deposited by a gas discharge, and the surface charge density  $n_s$  is a function of  $\hbar$  and the potential difference  $V_{\text{dc}}$  between the top electrode and three submerged electrodes. A low-frequency ( $\omega_1$ ) ac modulated bias voltage ( $V_1$ ) is applied to (1) and a lock-in amplifier connected to (3) is referenced at  $\omega_1$ . The ac voltage on (1) drives electrons forward and back across the center grounded electrode (2) as the bias goes from negative to positive at  $2\omega_1$ .

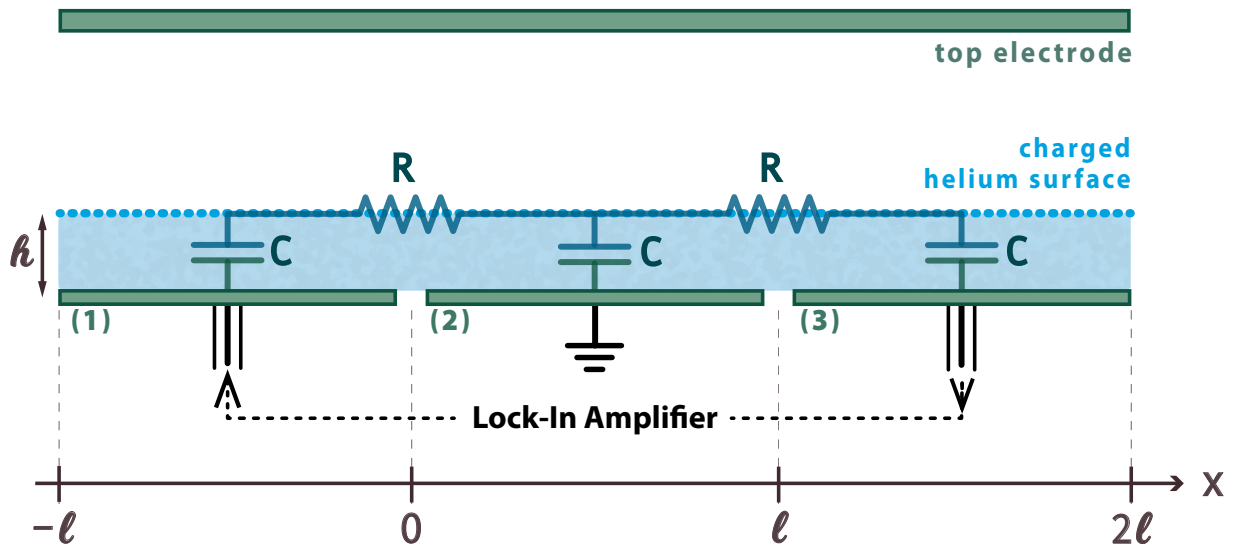


Figure 2.5: Sommer-Tanner transport measurement configuration from Ref. [53]. Electrodes (1), (2), and (3) of length  $\ell$  (colored green) are submerged a depth  $h$  below the liquid helium surface. Here, the ac drive is provided internally from the lock-in amplifier and simultaneously being referenced to that ac drive frequency. The 2DES above the liquid helium surface capacitively couples to the submerged electrodes, with capacitance per unit length  $C$ . When electrons are driven across the electrodes, the electron system will exhibit some resistance per unit length  $R$ .

The surface electrons are capacitively coupled to all three submerged electrodes, and this ac drive induces a current  $I_3$  at (3) that is measured by the lock-in amplifier. In this experiment Sommer and Tanner found an electron mobility of only up to  $2 \times 10^6$  cm<sup>2</sup>/Vs, due to being in a temperature range dominated by vapor atom scattering ( $T = 0.9$  K – 3.2 K).

In the original measurements performed by Sommer and Tanner, a transmission line modeling approach was not used, however, for measurement frequencies  $f$  and device lengths  $L$  such that  $fL \gtrsim 0.1$ , the ac driven electrons are most accurately modeled as a transmission line. In this case, there will be a capacitance per unit length between the surface electrons and the underlying electrodes will be  $C = C_0\ell$ . As the electron system is driven across the electrodes, it can be modeled as having a resistance per unit length  $R = R_0\ell$ , which is related to the electron mobility  $\mu$ . From this, we can write

$$R = \frac{1}{n_s e \mu \mathcal{L}} \quad (2.64)$$

$$C = \frac{\varepsilon_{\text{He}} \varepsilon_0 \mathcal{L}}{\hbar}, \quad (2.65)$$

where we see the resistance  $R$  is simply just the inverse of the electron conductivity from the dc Drude model we saw in Sec. 2.3.1.1, with the total length across all three underlying electrodes  $\mathcal{L} = \ell_1 + \ell_2 + \ell_3$ . We can calculate the current through the electron layer  $I_3$  following the transmission line analysis given by Mehrotra and Dahm [79]. One can find the relationship between the voltage  $V_1$  and current  $I_1$  at the input on (1) are related to the voltage  $V_3$  and current  $I_3$  at the output on (3) from the following relation in transmission line theory [80]:

$$\begin{pmatrix} V(x) \\ I(x) \end{pmatrix} = \begin{pmatrix} \cosh(\gamma x) & -Z_c(\gamma x) \\ -\frac{1}{Z_c} \sinh(\gamma x) & \cosh(\gamma x) \end{pmatrix} \begin{pmatrix} V(0) \\ I(0) \end{pmatrix}, \quad (2.66)$$

where  $\gamma$  is the propagation constant of the ac signal and  $Z_c$  is the characteristic impedance:

$$\gamma^2 = i\omega_1 C(R + i\omega_1 L) \quad (2.67)$$

$$Z_c^2 = \frac{R + i\omega_1 L}{i\omega_1 C} \quad (2.68)$$

and  $L = m_e/n_s e^2 \mathcal{L}$  is the inductance per unit length, which arises as a result of the inertia of the electrons. At low frequency in the Sommer and Tanner experiment the small inductance term can be ignored, such that the output current  $I_3$  is

$$I_3 = V_1 \left[ \sqrt{\frac{i\omega_1 C}{R}} \frac{\sinh(\sqrt{\gamma} \ell_1) \sinh(\sqrt{\gamma} \ell_3)}{\sinh(\sqrt{\gamma}(\ell_1 + \ell_2 + \ell_3))} \right]. \quad (2.69)$$

Here, it is assumed  $R$  and  $C$  are constant over the entire electrode region due to negligible edge effects because  $\hbar \ll$  dimensions of the electrodes.

In general, one can determine  $R$  and  $C$  of the electrons in the transmission line model by fitting Eq. 2.69 to phase sensitive lock-in measurement data. Additionally, these Sommer-Tanner transport measurements also allow us to estimate an electron density  $n_s$ , and if the density is known, together with the fit value for  $R$ , an estimate for  $\mu$  can be made, following Eq. 2.64. In the device shown in Fig. 2.5, an estimation of the density can be done if the center electrode (2) is negatively biased such that the region of (2) looks like a barrier to the electrons in regions (1) and (3). This creates a depleted region above (2) where no electrons exist and all electrons are in the regions above (1) and (3). As a result, during a

transport measurement, the output current  $I_3$  sharply decreases as electrons can no longer being driven across the device. The voltage at which the barrier into region (2) is decreased enough such that electrons can traverse across all three electrodes on electrode is called the threshold voltage  $V_{\text{th}}$ . For the device shown in Fig. 2.5, the threshold voltage on electrode (2),  $V_2^{\text{th}}$ , allows us to estimate an electron density  $n_s$ ,

$$n_s = -V_2^{\text{th}} \frac{e\hbar}{\epsilon_{\text{He}}\epsilon_0}. \quad (2.70)$$

A more in depth discussion of measuring the electron density via transport is provided in Sec. 2.4.

### 2.3.3 Transport of the Wigner crystal

Let us briefly return to a discussion of Wigner crystallization. At this point, we have addressed crystallization as a consequence of the large interelectron interaction strengths compared to the small thermal kinetic energy at low temperatures. In the previous section, we considered electron transport across a Sommer-Tanner device mainly in the context of an electron fluid but what happens in a transport experiment when the electron system crystallizes?

To answer this question, we start with the situation depicted in Fig. 2.6, where an electrode is submerged in the superfluid helium and a single electron floats above the helium surface. When the electrode is biased positively, the electric field points away from the electrode and the electron moves closer to the surface to lower its electrostatic energy. This, together with the image potential beneath the surface and the short-range repulsion from the Pauli exclusion principle for the helium atoms, induces a depression in the helium sur-

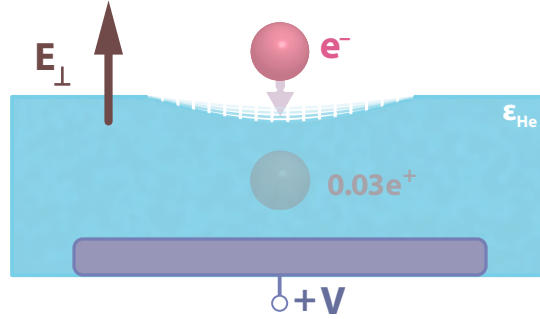


Figure 2.6: An electron (pink) above the surface of superfluid helium. A positive voltage on the electrode beneath ( $+V$ , purple) pulls the electron down towards the helium surface as an induced electric field points away from the surface  $E_{\perp}$ . This creates a dimple in the helium surface in the vicinity of the electron.

face. This depression is called a “dimple” and when the 2D electron system crystallizes, it will create what is referred to as a “dimple lattice”. The dimple lattice will have a lattice spacing that corresponds to the interelectron spacing and reciprocal lattice vectors  $\mathbf{G}$  of the solid. In the electron fluid phase, there is no well-defined dimple lattice because of the fast and irregular electron motion. Moreover, like every fluid with surface tension, when the liquid helium surface is disturbed, it will host short-wavelength surface waves called capillary waves, which are quantized for liquid helium. These quantized surface waves – or vibrational surface excitations – on superfluid helium are called ripples or surface phonons, and like any quantum of energy, they can be emitted or absorbed. The same way an electron disturbs the helium surface by forming a dimple, a ripplon can perturb the electron system – this interaction is known as electron-ripplon coupling – and the energy exchange between the two are central to understanding the transport of the Wigner crystal.

To illustrate the coupling between the quantized surface waves of the liquid helium and the electron crystal, it is instructive to remind ourselves what it means for two things to exchange vibrational or acoustic quanta of energy. The quantum mechanical process by which two systems exchange quanta of energy is well intuited when thinking about an atom

absorbing and emitting a photon. An incoming photon with energy corresponding to the quantized energy level difference of the atom's ground to first excited state allows the atom to absorb the photon, thus putting the atom into its first excited state. While there are many different ways in which that atom will eventually emit a photon, the resulting photon that is emitted will always correspond to that quantized energy lost by the atom. The way photons are electromagnetic quanta of energy, phonons are vibrational quanta of energy, and both require a medium to exist in. Ripplons can be emitted and absorbed by the 2D Wigner solid and when performing transport experiments, the mobility of the 2D Wigner solid will ultimately be limited by these interactions.

The ripplon scattering properties of the 2D Wigner crystal of electrons on helium are also distinct from those effecting the electron liquid. As discussed previously, the mobility of the 2D electron fluid at temperatures ( $T > 0.9$  K) is determined by temperature dependent helium atom scattering events and at lower temperatures ( $T < 0.7$  K) a function of ripplon scattering events.

### **2.3.3.1 Bragg-Cherenkov scattering**

The first experimental demonstration of Wigner crystallization detected resonant coupled ripplon-plasmon modes [34]. However another method for detecting Wigner crystallization is through transport measurements. In fact, in the 1971 experiment by Sommer and Tanner [53], they remark about a strange behavior in the measured mobility at low temperatures and high electron densities. In retrospect, it was possible they were seeing signatures of Wigner crystallization eight years before the landmark Grimes and Adams result [7]! Due to the temperature dependence of the electron mobility, at temperatures greater than those that would correspond to crystallization but in the ripplon scattering limit, one should ex-

pect to see the highest electron mobilities. Early mobility measurements near the Wigner solid transition [21, 46, 71] show a sharp increase in the mobility as the temperature decreases towards crystallization temperatures. The increase in mobility of a 2D electron liquid makes sense, as the decrease in temperature should reduce the number of scatterers. As the temperature continues to decrease, the plasma parameter  $\Gamma$  (Eq. 2.17) tells us that the system electrons should crystallize – below  $T \simeq 500$  mK, typical surface electron densities ( $n_s \gtrsim 4.5 \times 10^{12} \text{ m}^{-2}$ ) will correspond to crystallization.

The drop in mobility that is seen in transport measurements as a signature of Wigner crystallization is described by the framework of Bragg-Cherenkov scattering. In the electron fluid phase, there is no long-range periodic order in the electron system, however, when the system crystallizes, the electron lattice creates a Bragg condition such that constructive interference with ripplon scatterers can occur [70]. Bragg-Cherenkov scattering is a many-electron scattering process that results from the coherent emission and absorption of helium surface waves by the 2D electron crystal. As its namesake suggests, it involves the combination of two main processes: Bragg scattering and Cherenkov emission. Cherenkov emission occurs for single electrons when the electron velocity  $\mathbf{v}$  is greater than the phase velocity of the irradiated waves  $v_{\text{ph}}(q)$  and the momentum transferred  $\hbar\mathbf{q}$  is small compared to the electron momentum. When the electrons form a Wigner crystal, the many-electron system emits Cherenkov radiated waves that interfere constructively with each other. The periodic crystal lattice of the 2D electron solid provides a means for Bragg scattering these waves and when the wave vectors of the radiated waves are equal to the reciprocal lattice vectors of the electron solid  $\mathbf{G}$ , the interference is constructive. When the velocity of the electron solid  $(\mathbf{v} \cdot \mathbf{G}/G) \sim v_{\text{ph}}(G)$ , the emission rate increases dramatically [81].

### 2.3.3.2 The unresolved microscopic picture: crystal sliding versus melting

The underlying microscopic model describing the sharp decrease in conductivity upon the formation of a Wigner solid and then again increases for stronger driving fields is largely unresolved. Two main models have been introduced to describe the phenomena seen in transport experiments:

1. In the presence of weak to intermediate drive fields, the electron crystal deforms the superfluid helium surface by forming a lattice of dimples. As the electrons are driven, they must drag their corresponding dimple lattice with them, causing an increase in the effective mass of the electron system and thus a decrease in the conductivity [71]. As the Wigner solid is driven faster than the ripplon phase velocity, the electron system decouples from the dimple lattice, resulting in an increase in the measured conductivity as the electron system *slides* across the helium surface [27, 57].
2. In the presence of weak to intermediate drive fields, the decrease in mobility is entirely a Bragg-Cherenkov scattering effect, where the emission of ripples with a phase velocity  $v_{\text{ph}}(q)$  on the order of the Wigner solid reciprocal lattice vector  $G$  constructively interfere. At stronger driving fields, the jump in mobility is due to heating the crystal out of equilibrium with the liquid helium, effectively *melting* the crystal into its 2D electron fluid state [36, 81, 82].

A model by Vinen [83] presents an attempt to unify the dimple lattice and Bragg-Cherenkov scattering picture, where at low driving fields, the mobility is limited by a coherent deepening of the dimple lattice from the Bragg-Cherenkov effect. For increased driving forces, it is speculated that the electrons decouple from the dimple lattice causing the dimple lattice to fully disappear – the electron velocity  $v \gg v_{\text{ph}}$  and the conductivity is on the order of the

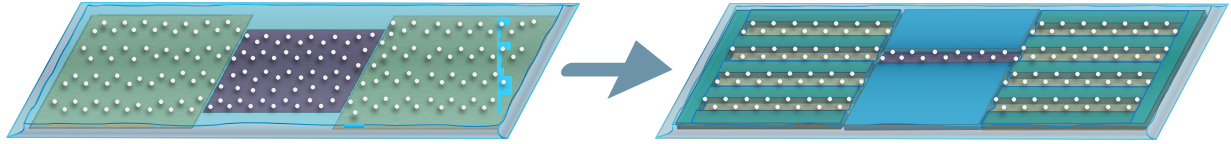


Figure 2.7: The typical Sommer-Tanner device (left) with additional channeled structures patterned on top of the electrodes (right) to enable precise control over the electron system and support a more stable helium surface with higher electron densities. Electrodes on the top surface of the dielectric channeled structures (blue and green) provide additional control over the confinement.

electron fluid conductivity. Many experiments have been performed to observe the nonlinear transport behavior of the electron on helium Wigner crystal and to attempt to resolve the underlying mechanism [25, 28, 65, 66, 82, 84–89]. The non-linear transport properties of the Wigner solid in the context of Bragg-Cherenkov scattering and the unresolved microscopies are discussed further in Section 3.2.1 in the context of subjecting the electron crystal to an additional microwave field.

## 2.4 Microchannel devices for electrons on helium

The simple Sommer-Tanner device architecture, while great for simple low density transport measurements, lacks the ability to produce precise spatial control over the electron system. To combat this, in 1986 Marty [90] proposed creating micro-structured channels on top of the Sommer-Tanner electrodes (see Fig. 2.7). The addition of these structures provides many experimental benefits for investigating surface state electrons on helium. These benefits include the ability to achieve higher densities of electrons. Additionally, the small patterned channel sizes can help suppress ripplons, and patterning electrodes on top of the structures enables a high level of confinement and spatial control over the electron system.

The first microchannel device introduced by Marty [90] aimed to study electron systems

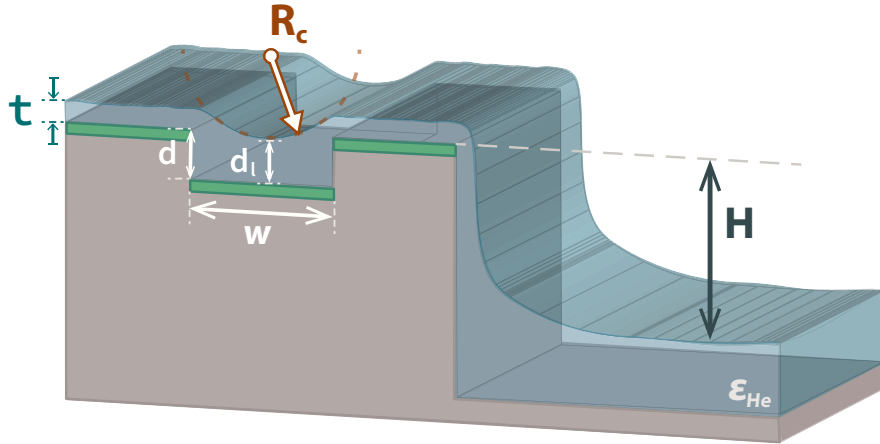


Figure 2.8: Cross section of a typical microchannel device filled with superfluid helium via capillary action. The bulk helium sits a height  $H$  below the microchannel features and a van der Waals film of thickness  $t$  covers the top surfaces. At superfluid helium temperatures, a channel width  $w$  less than the superfluid helium capillary length  $l_c \simeq 0.5$  mm, a helium meniscus in the channel will form with a radius of  $R_c$ . The distance of the bottom point of the meniscus to the bottom of the channel is  $d_l$  and the total depth of the channel is  $d$ . The tan color represents an arbitrary dielectric substrate (typically Si) and the green features in the microchannel region are metallic electrodes.

at high densities corresponding to quantum melting of the Wigner crystal [19] as well as for detecting the formation of the Wigner crystal under geometric confinement [90]. In 2000, Glasson introduced the micro-structures into a Sommer-Tanner-like device architecture to investigate the transport properties of one-dimensional electron chains [91]. In recent years, this microchannel device architecture has been shown to be a unique way to facilitate investigations of the properties of highly correlated low-dimensional electron behavior [13, 85, 92], the melting behavior of quasi-1D electron systems [25, 86], and Wigner crystallization under various driving fields and spatial constrictions [28, 87, 88, 93].

### 2.4.1 Superfluid helium as a substrate in microchannel devices

A cross section of the typical microchannel device geometry is shown in Fig. 2.8. The zero viscosity of superfluid helium allows the superfluid to creep up all the exterior walls,

covering all the structures throughout the device due to the van der Waals forces between the surfaces and the superfluid helium. In the cross section, a small microchannel of width  $w$  and depth  $d$  fills via capillary action. Below, we discuss the concepts of microchannel devices to inform their general operation and highlight why they are an ideal platform for studying low-dimensional electron behavior.

The thickness of the van der Waals helium film  $t$  that covers all the surfaces of the device depends on the height  $H$  of the surface from the bulk liquid helium below. The chemical potential of the film at  $z = H$  is [94]

$$\mu_f = \mu_0 + \rho g H - \beta/t^\xi, \quad (2.71)$$

where  $\beta$  is the van der Waals coupling constant and the thickness of the film can be calculated by using the equilibrium condition  $\mu_f = \mu_0$ , where  $\mu_0$  is the chemical potential of the bulk helium. The term  $\beta/t^\xi$  describes the van der Waals potential of the substrate for either large film thicknesses ( $\xi = 4$ ) or thin film thicknesses ( $\xi = 3$ ) [95]. From this, the thickness of the film is given by [96],

$$t = \left( \frac{\beta}{\rho g H} \right)^{1/\xi}, \quad (2.72)$$

where  $\rho$  is the superfluid helium density and  $g$  is the gravitational constant.

When electrons are introduced above the superfluid surface, the electrostatic pressure of the electrons reduces the helium film thickness, creating a more unstable surface. This pressure will be a result of: i) gravity pulling down on the fluid surface, ii) the van der Waals interaction with substrate, iii) the surface tension of of the superfluid, iv) the electrostatic pressure from any external electric fields, v) and the electrorestrictive pressure produced by

the surface electron density. Thus, the total pressure on the superfluid surface is

$$P = \rho g H - \frac{\beta}{t^\xi} - \alpha \nabla^2 t - \frac{\varepsilon_0}{2} (\varepsilon_{\text{He}} - 1) (\varepsilon_{\text{He}} E_\perp^2 + E_\parallel^2) + n_s e \nabla \phi_e \quad (2.73)$$

where  $\alpha$  is the liquid helium surface tension,  $E_\perp$  and  $E_\parallel$  are external electric fields perpendicular and parallel to the helium surface, respectively, and  $\phi_e$  is the electric potential from the charged surface [97–99]. For an uncharged helium surface with no external fields, there is no net pressure,  $P = 0$ , in Eq. 2.72. In contrast, in the case of a charged helium surface and when the film is covering a metallic surface, the electric potential takes the form of a parallel plate capacitor  $\phi_e = n_s e z / 2 \varepsilon_{\text{He}} \varepsilon_0$  and the thickness in Eq. 2.72 becomes

$$t = \left( \frac{\beta}{\rho g H + \frac{n_s e}{z} \phi_e} \right)^{1/\xi}. \quad (2.74)$$

With small channels embedded into the surface at  $H$  above the bulk with metal electrodes on the surfaces, the sharp corners of the channel lead to strong capillary forces in the superfluid due to surface tension. This simplifies the equilibrium condition to

$$\rho g H - \frac{\alpha}{R_c} + \frac{n_s^2 e^2}{2 \varepsilon_{\text{He}} \varepsilon_0} = 0, \quad (2.75)$$

where we have defined the radius of curvature of the helium film in the channel  $R_c \equiv 1/\nabla^2 t$ . The capillary length of superfluid helium is  $l_c = \sqrt{\alpha/\rho g}$ , where for a channel width  $w \ll l_c$ , a meniscus feature will cover the feature as shown in Fig. 2.8. The radius  $R_c$  of this meniscus feature formed at the surface of the helium in the channel can be calculated from Eq. 2.75,

$$R_c = \frac{\alpha}{\rho g H + \frac{n_s^2 e^2}{2 \varepsilon_{\text{He}} \varepsilon_0}}. \quad (2.76)$$

For the case depicted in Fig. 2.8, the film covering the channel creates a liquid helium depth in the center of the channel  $d_l$  given by

$$d_l = d - R_c \left( 1 - \sqrt{1 - \frac{w^2}{4R_c^2}} \right), \quad (2.77)$$

where  $d$  is the total depth of the channel set by the etched substrate and the thickness of the metal electrode. When the radius of curvature is much larger than the width of the channel, i.e. when  $w/R_c \ll 1$ , we get the following approximation for the height at the center of the channel:

$$d_l = d - \frac{w^2}{8R_c}. \quad (2.78)$$

### 2.4.2 Critical electron density

Microchannel devices like the one in Fig. 2.8 are useful for increasing the electron surface densities above those typically achievable in larger area devices. The critical density  $n_c$  is the electron density at which the surface electrons put too much local electrostatic pressure on the helium surface and punch through the liquid due to an electrohydrodynamic instability [100].

To calculate the critical density at which the helium surface reaches this hydrodynamic instability, we can turn to the dispersion relation for riplons. In the presence of surface charges, the frequency of the riplons  $\omega_r$  decrease with increasing electron density  $n_s$ . For the case of bulk helium, with the ratio of the ripplon wave number  $k$  to the electron surface density,  $(k/2\pi)^2/n_s \ll 1$ , the ripplon frequency will be limited by the electron density such that [98]

$$\omega_r^2 = gk + \frac{\alpha}{\rho}k^3 - \frac{e^2 n_s^2}{\rho \varepsilon_{\text{He}} \varepsilon_0} k^2. \quad (2.79)$$

From this, we see that superfluid surface will become unstable at wave numbers given by  $k_c = \sqrt{g\rho/\alpha}$ , where  $\omega_r^2 < 0$ , and we can calculate the electron critical density  $n_c$  that corresponds to the hydrodynamic instability:

$$n_c = \frac{(4\alpha g\rho)^{1/4}}{\sqrt{e^2/\varepsilon_{\text{He}}\varepsilon_0}}. \quad (2.80)$$

This gives the standard bulk helium critical density of  $n_s \simeq 2 \times 10^{13} \text{ m}^{-2}$ . On the other hand, in the microchannel device structures, there exists a minimum wave vector  $k_{\text{min}} \simeq \pi/l_0$  for helium surface deformations to exist within a feature size  $l_0$  set by the fixed boundary conditions at the edges of the channel. Following the treatment in Ref. [90], this gives the critical density in a microchannel structure

$$n_c = \sqrt{\frac{\alpha \varepsilon_{\text{He}} \varepsilon_0 \pi}{e^2 l_0}}. \quad (2.81)$$

The relevant microchannel feature sizes for the experiments described in this thesis ( $l_0 \sim 10^{-6} \text{ m}$ ) correspond to critical densities of  $n_c \sim 5 \times 10^{14} \text{ m}^{-2}$ , an order of magnitude larger than in the bulk case. While this is a good estimation, the electronic pressure that creates the radius of curvature  $R_c$  of the helium in the microchannel will slightly reduce this critical density. To find the critical density for the charged surface with a helium surface radius of curvature  $R_c$  in the channel of width  $w$  for  $w/R_c \ll 1$ , we plug Eq. 2.76 into Eq. 2.78 and we get

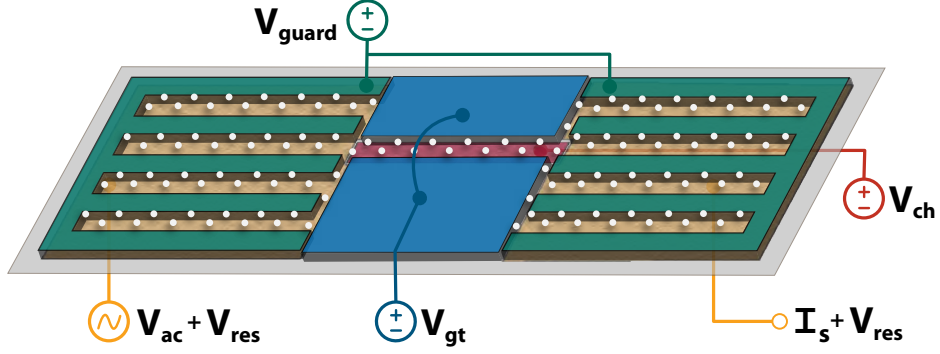


Figure 2.9: A simplified sketch of a microchannel device architecture with Sommer-Tanner electrodes embedded. The Sommer-Tanner electrodes are the yellow and red colored electrodes at the bottom, where the left side yellow electrode corresponds to (1) in Fig. 2.5, the middle red electrode corresponds to (2), and the right side yellow electrode corresponds to (3). Yellow electrodes are the reservoir electrodes and have a dc bias voltage  $V_{\text{res}}$  and red electrode in the center is the channel electrodes with a dc bias voltage  $V_{\text{ch}}$ . Helium fills the channels created by the etched down area around the green (guard electrode,  $V_{\text{guard}}$ ) and blue (gate electrode,  $V_{\text{gt}}$ ) electrodes, where the green and blue electrodes are dc biased to provide strong electrostatic confinement for the electron system. The ac drive  $V_{\text{ac}}$  is modulated at frequency  $f_{\text{ac}}$  on the left reservoir electrode and the resulting electron current  $I_s$  is read out on the right reservoir electrode via lock-in amplifier.

$$d_l = d - \frac{w^2}{8\alpha} \left( \rho g H + \frac{n_s^2 e^2}{2\epsilon_{\text{He}} \epsilon_0} \right) \quad (2.82)$$

for the center of the channel. At the critical density,  $d_l \rightarrow 0$  and here  $\rho g H \ll (n_s^2 e^2 / 2\epsilon_{\text{He}} \epsilon_0)$ , which then gives

$$n_c = \sqrt{16 \frac{\alpha d \epsilon_{\text{He}} \epsilon_0}{w^2 e^2}}. \quad (2.83)$$

For a microchannel of width  $w = 7 \times 10^{-6}$  m and a channel depth  $d = 1.4 \times 10^{-6}$  m (the dimensions of the microchannel device used for the experiments outlined in Ch. 3) the critical density is  $n_c = 2.5 \times 10^{14} \text{ m}^{-2}$ , or about half of that estimated by Eq. 2.81.

### 2.4.3 Transport measurements in microchannel devices

The standard microchannel device architecture used in the experiments discussed in this thesis is shown in Fig. 2.9. In this device, Sommer-Tanner electrodes (yellow and red) are patterned such that transport measurements of electrons on helium in an electrostatically confined long and narrow region in the center (called the central microchannel) can be performed. The channeled structures throughout (the cross section of which resembles Fig. 2.8) provide a more stable helium surface that can support high electron densities, in particular, providing stability in the large reservoir regions on the left and right side. Additionally, the electrostatic confinement of the electron system can be finely tuned with dc voltages on the surrounding electrodes (green and blue), allowing precise spatial control over the 2DES and investigations into 2D and quasi-1D electron system behavior in various transport regimes (see Sec. 2.4.4). In the devices described in this thesis, after condensing helium in the sample cell such that the superfluid fills the channels, electrons are deposited via thermal emission of a tungsten filament [101].

A standard transport measurement in a device of this type is performed as follows: An ac drive  $V_{ac}$  (at frequency  $f_{ac} \sim 20 \text{ kHz} - 4 \text{ MHz}$ ) is superimposed onto the dc bias voltage  $V_{res}$  applied to the reservoir electrode via a bias tee. Simultaneously, on the other reservoir, the same dc bias voltage  $V_{res}$  is applied along with the lock-in amplifier measurement referenced to the ac drive frequency  $f_{ac}$ . The gate and guard electrodes have a fixed dc bias voltages ( $V_{gt}$  and  $V_{guard}$ , respectively) to provide another level of electrostatic confinement over the electron system. At sufficiently large dc bias voltage on the channel electrode,  $V_{ch} \geq V_{ch}^{th}$ , an electron current will be induced through the device and detected via the lock-in amplifier as  $I_s$ . This is referred to as the channel threshold voltage  $V_{ch}^{th}$ . This process is outlined in

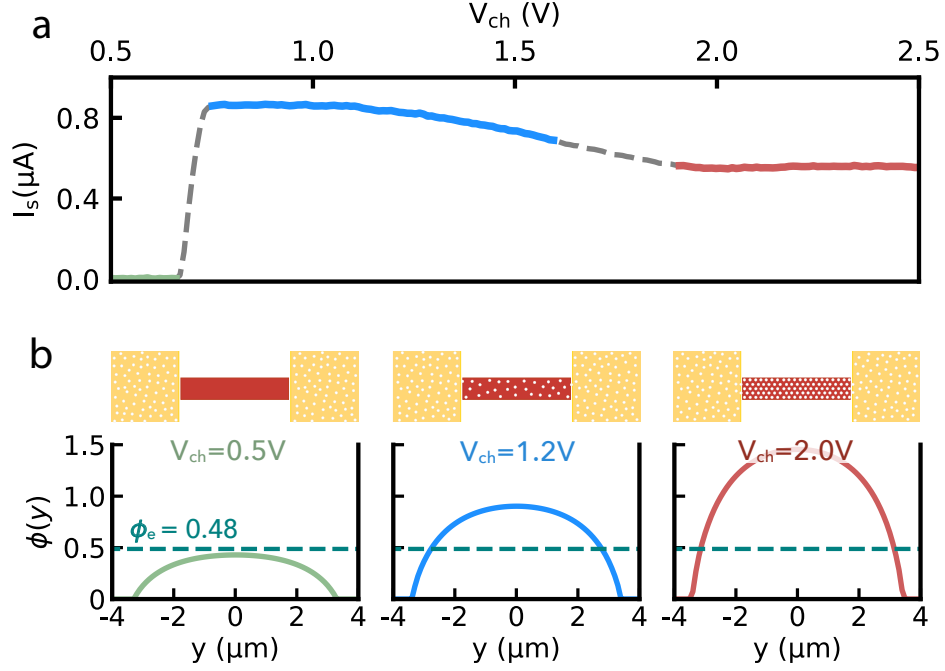


Figure 2.10: (a) Typical transport measurement sweeping  $V_{\text{ch}}$  with  $V_{\text{res}} = 0.5$  V,  $V_{\text{gt}} = -0.15$  V,  $V_{\text{ac}} = 30$  mV, and  $f_{\text{ac}} = 43.33$  kHz at temperature  $T = 750$  mK. Here the threshold voltage  $V_{\text{ch}}^{\text{th}} = 0.67$  V, below which no transport can occur (light green region). This plot shows the three transport regimes: (I, light green) no transport, (II, dodger blue) low density high conductivity, (III, red) Wigner crystal. (b) Sketches show the corresponding configuration of electrons in the reservoirs (yellow region) and channel (red region) in each regime (I, II, and III). Plots show the potential  $\phi(y)$  at the center of the channel across the width of the channel in each regime from (a). The chemical potential  $\phi_e = 0.48$  V (teal dashed line) shows the minimum  $\phi(y)$  necessary for transport through the channel to occur. Below the threshold at  $V_{\text{ch}} = 0.5$  V, no electrons can enter the channel, at the low density corresponding to  $V_{\text{ch}} = 1.2$  V the electron system in the channel resembles an electron fluid, and at high densities  $V_{\text{ch}} = 2.0$  V the electron system in the channel crystallizes.

Fig. 2.10.

Similarly to the standard Sommer-Tanner architecture, this microchannel device provides a way to perform transport experiments via the three embedded electrodes and to estimate the electron density in the central channel by sweeping the voltage on the channel electrode  $V_{\text{ch}}$  and by finding the threshold value at which electrons can enter the channel  $V_{\text{ch}}^{\text{th}}$ . A first order approximation of the areal density of the electron system in the central channel is

$$n_s = \frac{\varepsilon_{\text{He}} \varepsilon_0}{ed} (V_{\text{ch}} - \alpha_{\text{ch}}^0 V_{\text{ch}}^{\text{th}}). \quad (2.84)$$

The density of electrons at a given channel voltage  $V_{\text{ch}}$  depends on the average distance of the electron system above the channel electrode  $d$ , the threshold voltage  $V_{\text{ch}}^{\text{th}}$ , and the capacitive coupling constant between the electron system and the channel electrode at the center of the channel  $\alpha_{\text{ch}}^0$ . In general, the electron system is capacitively coupled to each  $i^{\text{th}}$  electrode by some amount parameterized by  $\alpha_i = C_i/C_{\Sigma}$ , where the total capacitance between the electrons and each corresponding electrode is  $C_{\Sigma} = \sum_i C_i = C_{\text{ch}} + C_{\text{gt}} + C_{\text{res}} + C_{\text{gu}}$  (see Fig. 2.11 for an illustration of this capacitive coupling). The second term in parentheses  $\alpha_{\text{ch}}^0 V_{\text{ch}}^{\text{th}} \equiv \phi_e$  is the chemical potential. These coupling constants  $\alpha_i$  can be found from finite element modeling (FEM) simulations of the central region of the device. Furthermore, a more accurate estimate of the electron density in the channel can be made through FEM simulations of the 2D cross section in the center of the channel (see Fig. 2.11). For a complete description of the FEM techniques used to find these parameters, see Appendix C.

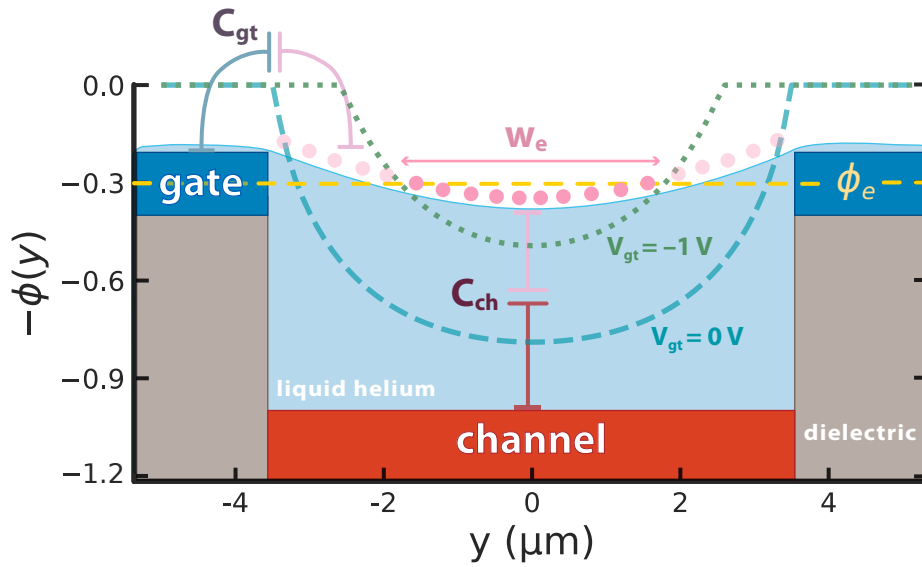


Figure 2.11: Cross section of the central microchannel region showing the electrostatic potential confinement on the electron system (electrons represented by pink dots). The confinement across the  $y$ -direction of the channel is defined by the potential profile  $\phi(y)$  (see Eq. 2.86), which is a function of the capacitive coupling between the electron system and the electrodes ( $C_{ch}$  and  $C_{gt}$ ) as well as the dc voltages on the channel and gate electrodes ( $V_{ch}$  and  $V_{gt}$ ). Here we plot the potential as  $-\phi(y)$  for visualization purposes. The potential profile with  $V_{ch} = 1$  V is shown for two different gate electrode voltages,  $V_{gt} = 0$  V (teal dashed line) and  $V_{gt} = -1$  V (green dotted line). The chemical potential  $\phi_e = 0.3$  V (yellow dashed line) defines the effective width  $w_e$  of the electron system for a given potential profile.

### 2.4.4 Confinement

The gate and guard electrodes defined atop the microchannel structures provide an added level of precision control over the electrostatic confinement of the electron system in the channel. In general, at a given position in the device, the electron system will experience an electrostatic potential given by

$$\phi(x, y) = \sum_i \alpha_i(x, y) V_i, \quad (2.85)$$

where  $\alpha_i(x, y)$  is the capacitive coupling of the electron at position  $(x, y)$  with the corresponding  $i^{th}$  electrode and  $V_i$  is the voltage on that  $i^{th}$  electrode. For a long and narrow channel, the capacitive coupling constant of the electrons to the guard and reservoir electrodes will be negligible at the center of the channel ( $x = 0$ ). Thus, we can estimate the potential at the center ( $x = 0$ ) of the microchannel across the width ( $y$ ) as

$$\phi(y) = \alpha_{\text{ch}}(y)V_{\text{ch}} + \alpha_{\text{gt}}(y)V_{\text{gt}}. \quad (2.86)$$

As shown in Fig. 2.11, the voltage on the gate electrode  $V_{\text{gt}}$  will control the effective width  $w_e$  of the electron system in the channel, where  $w_e$  increases with increasingly positive bias  $V_{\text{gt}}$ . The electrostatic potential profile for  $V_{\text{gt}} = 0$  V (teal dashed line) and  $V_{\text{gt}} = -1$  V (green dotted line) is plotted. The electron system forms an effective width of  $w_e \simeq 4$   $\mu\text{m}$  in the  $V_{\text{gt}} = -1$  V,  $V_{\text{ch}} = 1$  V potential for a chemical potential of  $\phi_e = 0.3$  V (yellow dashed line). These additional electrodes provide another knob for spatially controlling the electron system and precisely tuning the confinement such that 1D and quasi-1D electron chains can be investigated [25, 66, 86, 93, 102].

## 2.5 Quantum devices with electrons on helium

Efforts to utilize single electrons on helium for quantum hardware involves the integration of quantum circuits with standard electron on helium devices. Early work integrating quantum devices with electrons on helium involved single electron transistors (SETs) in order to detect a single trapped electron as well as charge-coupled devices (CCDs) [103] for the possibility of high mobility transport of single electron qubits. Additionally, architectures integrating both ensembles [39] and single electrons on helium [104] with superconducting coplanar waveguide (CPW) resonators have been realized in order to study electron ensemble dynamics as well as to establish the readout and manipulation of qubits based on single electrons.

### 2.5.1 Qubits with trapped electrons on helium

A large motivation for why the system of trapped electrons on helium is interesting to understand (beyond investigating fundamental physics) has to do with its potential as a platform for quantum computation, however, this is not a thesis about how to quantum compute or how to build a quantum processor with electrons on helium. Before the contemporary quantum computing revolution<sup>9</sup>, quantum computing was envisioned as a way to better understand quantum physics. Nearly 80 years after the conception of quantum mechanics, Feynman gave the historic keynote [105] first proposing quantum computing, where the most straightforward platform for a qubit was a single spinful particle such as the electron.

The formation of a low density electron crystal and the ultra high mobilities of trapped electrons above the surface of liquid helium motivated the theoretical work of Platzman and Dykman in 1999 [73] who proposed using the vertical states of single trapped electrons

---

<sup>9</sup>I'm referring to the current decade of writing this as the quantum computing revolution, which is not so crazy considering the UN just declared 2025 the International Year of Quantum Science and Technology.

as quantum bits (qubits) for analog quantum computation. In this work, they estimated a ripplon scattering dominated energy relaxation time of  $\approx 0.1$  milliseconds and today efforts to realize qubits from the vertical positions of electrons on helium are ongoing [38, 41, 50, 106–109]. Following this initial theoretical proposal, in 2003 Lyon [110] proposed an architecture that utilizes the spin degree of freedom of the electron as a qubit, estimating coherence times on the order of many seconds. The higher coherence time for the spin degree of freedom makes it particularly attractive and results from the ultra clean, defect free helium substrate and reduced spin-orbit interactions compared to what is typical in semiconductor spin systems [110]. The third and final proposed degree of freedom for an electron on helium qubit is the lateral motional (orbital) state of the electron when the electron is confined to an in-plane potential well. This platform [111] utilizes circuit quantum electrodynamics (cQED) [112] to control and readout the lateral motional states of the confined electrons. Efforts to demonstrate a lateral motional state qubit are ongoing, with early work integrating electrons on helium with standard cQED devices such as superconductor coplanar waveguide (CPW) resonators. The first demonstration integrating a CPW resonator with a system of trapped electrons above a superfluid helium surface showed the collective charge motion of the electron ensemble coupling to the superconducting coplanar waveguide (CPW) resonator [39], which manifested as a shift in the frequency of the resonator. A later device demonstrated single electron trapping in an electrostatic potential well and showed coupling of single electron motional states to a CPW resonator [104]. Technology based on this work [104] is being further developed to manipulate and readout the electron spin degree of freedom [113, 114]. It is also important to note here that electrons on *helium* are not the only trapped electron system being pursued for quantum information science. Architectures based on Ref. [104] have demonstrated high coherence charge qubits with electrons on *solid*

*neon*, with coherence times on the order of 0.1 ms [115, 116].

## 2.5.2 Single electron transistors

In Sec. 2.1.2.2 the metal-oxide-semiconductor field-effect transistor (MOSFET) was introduced to illustrate the advantages of studying 2DESs on helium and the unconventional analog of the FET using electrons on helium [52] was introduced. For qubits based on single trapped electrons on helium, an early proposal suggested the use of a single electron transistor (SET) for the electronic charge state readout [117], due to its high charge sensitivity. Similarly to the FET, the operation of an SET relies on source, drain, and gate electrodes. However, rather than an induced current from the conducting electrons across a channel, the source and drain electrodes, separated by an SET island or quantum dot, have tunnel junctions on either side, and the state of the device is determined by whether or not electrons tunnel through the quantum dot. Operationally, this follows from the Coulomb blockade [118]. The gate electrode controls the electric potential of the quantum dot through a capacitive coupling and by positively tuning the gate voltage, a tunneling current can be achieved across the source and drain<sup>10</sup> [18]. When an SET is submerged beneath the surface of superfluid helium and an electron is present above the SET island, a charge will be induced on the SET island, providing a way to detect the presence of single electron charge states.

Using an SET to detect electrons above the helium surface was first demonstrated by Papageorgiou in 2003 [119] and in 2005, Papageorgiou [120] demonstrated the ability to trap

---

<sup>10</sup>The total capacitance on the island  $C_\Sigma$  must be small enough such that the bias voltage across the source and drain  $V_b < e/C_\Sigma$  and the electrostatic energy required to put a charge carrier on the island is much larger than  $k_B T$ , i.e.  $e^2/2C_\Sigma \gg k_B T$ , so thermally excited charge carriers cannot pass through the island. [18]

and detect single electrons with an SET device architecture. In these devices, the SET is placed within an electron trapping region (an electrostatic potential well), where electrons are transferred from an adjacent reservoir region to the trap region through surrounding patterned gate electrodes. As the electrons are introduced into the trapping region, each individual electron induces a change in the charge  $\Delta Q$  on the SET island such that  $\frac{\Delta Q}{e} > 0$ .

SETs have also been used to study noise in quantum devices. As quantum devices, such as qubits for quantum computing, continue to improve, the seemingly unavoidable low-frequency noise, known as  $1/f$  noise, continues to be a limiting factor in charge sensitive devices. In these types of devices,  $1/f$  noise results from two-level fluctuators (TLFs) [121, 122] – quantum two-level systems that arise from microscopic degrees of freedom in amorphous solids, e.g. in the oxide layer of a Josephson junction [123–125], shown to be a primary source of decoherence in superconducting qubits [124, 126–129]. In particular, noise from TLFs in and around an SET tunnel junction add a layer of difficulty in performing sensitive quantum measurements. As efforts to integrate SETs with electrons on helium for single trapped electron qubits progress, work has been done to investigate how immersing an SET in superfluid helium effects the noise performance of the SET [130]. In this work [130], it is found that the frequency of charge fluctuations from TLFs near the SET tunnel junctions are reduced when submerged in superfluid helium, presenting a unique advantage for utilizing SETs in quantum devices with electrons on helium.

### 2.5.3 Charge-coupled devices

Charge-coupled devices (CCDs) are commonly associated with the technology that enabled digital imaging capabilities in early digital cameras, however the fundamental operation of the device make it quite convenient for transporting small ensembles and single electrons on

helium. A single CCD channel is comprised of a one dimensional array of electrodes along the channel, where each electrode corresponds to a pixel across which charge packets are transferred and at the last electrode, the charge packet is converted into a voltage signal. The efficiency of a single charge transfer  $\eta$  is defined as the ratio of the charge arriving at electrode 2 to the charge originally stored in the neighboring electrode 1 [131, 132]. Incorporating individual arrays of CCDs into microchannel architectures enables greater single electron control as well as a pathway towards realizing mobile single electron on helium spin qubits.

The first measurement of charge transfer efficiency in electrons on helium using a CCD array was demonstrated in 2006 by Sabouret and Lyon [133]. In this work, electron transfer between gates was governed by diffusion, ultimately limiting the operating frequencies (at 13 Hz,  $\eta = 0.9974$ ), however the charge transfer efficiency remained high at low electron densities. Large improvements in transport efficiency have been made by integrating CCD arrays into microchannel structures, where the narrower underlying gates facilitate the strong fringing fields that help electron transfer and also provide more relatively uniform holding fields [103]. In an electron on helium CCD-microchannel architecture, electron packets down to single electrons were clocked over  $10^9$  pixels, corresponding to 9 km without any transfer errors detected, with transport efficiencies reported to be four orders of magnitude better than state of the art semiconductor CCDs [14]. Continued work in developing these CCD integrated microchannel devices have enabled a pathway towards high precision single electron detection and spatial control for mobile spin qubits [113, 134–136].

# Chapter 3

## Plasmon mode engineering with microchannel devices

Circuit quantum electrodynamics (cQED) [112] has enabled the development of sophisticated quantum control and measurement protocols for a wide variety of quantum systems ranging from superconducting circuits [137] and semiconductor spins [138], to systems of trapped electrons [104, 115, 116], as well as nano- and micromechanical oscillators [139–141]. These techniques can also be leveraged as powerful experimental tools for investigating microwave frequency *collective* phenomena in quantum systems composed of many interacting particles or degrees of freedom [142]. For example, when coupled with superconducting circuits, these approaches have been used to study collective modes in magnonic [143–147] and phononic [148–151] systems and to investigate the dynamics of spin ensembles [152, 153].

Electrons trapped above the surface of condensed noble gas substrates, such as superfluid helium or solid neon, are emerging as promising systems for integration with cQED architectures and microwave frequency devices for quantum information processing [73, 110, 154, 155]. At the level of single electrons, cQED techniques have been used to investigate the in-plane orbital states of electrons on helium [104, 156] and have recently been utilized to realize high-coherence charge qubits on the surface of solidified neon [115, 116]. In contrast to single electron dynamics, these systems can also host a wide variety of collective charge modes

including plasmonic [7, 34] and magneto-plasmonic excitations [30, 35, 40, 157, 158], as well as hybrid modes coupling the dynamics of multiple degrees of freedom [41–43]. Additionally, ensembles of electrons on helium have been strongly coupled to three-dimensional microwave cavities to study cyclotron resonance [37, 44] and integrated into hybrid circuits in which an electron ensemble is placed above a planar microwave resonator [39]. Fully leveraging cQED-type techniques to study the high-frequency dynamics of electrons on helium requires the development of devices that have not only an optimized microwave environment [39], but also the ability to engineer and manipulate the collective modes of the electron system via precise spatial control. In this work, we address the latter of these aspects by realizing a device that enables precision control over the spatial distribution of electrons in a microchannel geometry, providing the ability to engineer, excite, and detect plasmonic excitations with frequencies in a range compatible with cQED-based systems. Local microwave excitation resonantly couples to the plasmon modes, which we detect via changes in the electron conductance determined by simultaneous transport measurements. By precisely varying the electron density in the microchannel, we can tune the frequency of the modes by several GHz. Analyzing the power dependent plasmon response allows us to investigate possible mechanisms leading to plasmon dephasing and energy loss. Finally, we highlight how this type of device and our results demonstrate the overall system control necessary to integrate with future low-loss microwave cQED architectures.

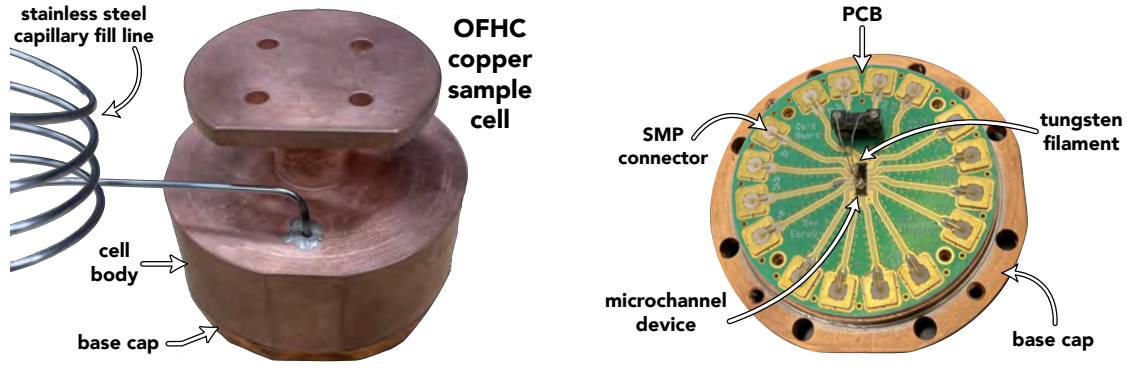


Figure 3.1: Oxygen-free high thermal conductivity (OFHC) copper sample cell with stainless steel capillary fill line and assembled base cap with custom printed circuit board (PCB). The PCB is mounted and electronically connected via SMP connectors. The microchannel device is adhered to the PCB with GE varnish and wirebonded to the PCB coplanar waveguide lines. The two wires of the tungsten filament are soldered to a 2-pin dual in line package (DIP) integrated circuit (IC) socket and the DIP IC socket is soldered to the PCB. The tungsten filament wires are manipulated such that the filament hovers  $\approx 2 - 5$  mm above the center of the microchannel device.

### 3.1 Experimental setup

#### 3.1.1 Microchannel device for plasmon confinement

Microchannel device architectures, like the one we employ, are widely used to study the effect of geometric confinement on the thermodynamic ground state and transport properties of electrons on helium. Typically in these devices, micron-scale deep channels are filled with superfluid helium via capillary forces and electrons are deposited above the superfluid surface. Metallic electrodes around the channels are used to precisely shape the electrostatic environment to control the spatial distribution of surface state electrons and perform transport experiments [13, 90]. These types of channeled devices have been used to reveal dynamical ordering of two-dimensional [11, 64] and quasi-one-dimensional electron chains [65, 66], and perform ultra-efficient clocking of electrons in microchannel-based CCD arrays [14, 103]. Here we leverage a microchannel architecture to engineer the spatial structure of the two-

dimensional electron system in order to host and investigate charge density oscillations, i.e. plasmons.

The device is fabricated on a  $7 \text{ mm} \times 2 \text{ mm}$  high resistivity silicon chip, onto which hard-baked resist is deposited and selectively etched to create  $h \simeq 1.4 \text{ }\mu\text{m}$  deep channels (see Appendix B). The device is wire-bonded onto a custom-made printed circuit board (PCB) that is placed into a superfluid-leak-tight copper sample box that mounts to the mixing chamber plate of a cryogen-free dilution refrigerator (see Fig. 3.1). A stainless steel capillary fill line is hard soldered into the sample cell, which extends to a room temperature volume containing helium gas for filling the microchannels with liquid. The sample cell contains a tungsten filament for thermionic electron emission, which is achieved by applying a  $-2 \text{ V}$  amplitude,  $300 \text{ ms}$  duration, square pulse to the filament. As shown in Fig. 3.2, four electrodes are lithographically patterned to define two reservoir areas connected via a central microchannel region having a length of  $L = 90 \text{ }\mu\text{m}$  and a width of  $w = 7 \text{ }\mu\text{m}$ .

The high degree of spatial control and confinement over the electrons in the reservoirs and microchannel regions are enabled by voltages ( $V_i$ ) applied to the four electrodes:  $V_{\text{gt}}$  (gate),  $V_{\text{ch}}$  (channel),  $V_{\text{res}}$  (reservoirs), and the guard electrode. These voltages allow us to control the two-dimensional electrostatic environment experienced by the electrons in the plane of the helium surface  $\phi(x, y) = \sum_i V_i \alpha_i(x, y)$  (see Fig. 3.3a), where the constant  $\alpha_i(x, y)$  describes the capacitive coupling between the electrons and the corresponding  $i^{\text{th}}$  electrode. To design a given confinement profile, we numerically solve the Laplace equation using finite element modeling (FEM) techniques [86]. This allows us to extract  $\alpha_i$  and construct the potential by applying appropriate values of  $V_i$ . This numerical procedure also allows us to calculate the areal electron density  $n_s(x, y)$  for a given potential.

By controlling the electrostatic environment in this fashion, we can effectively create a

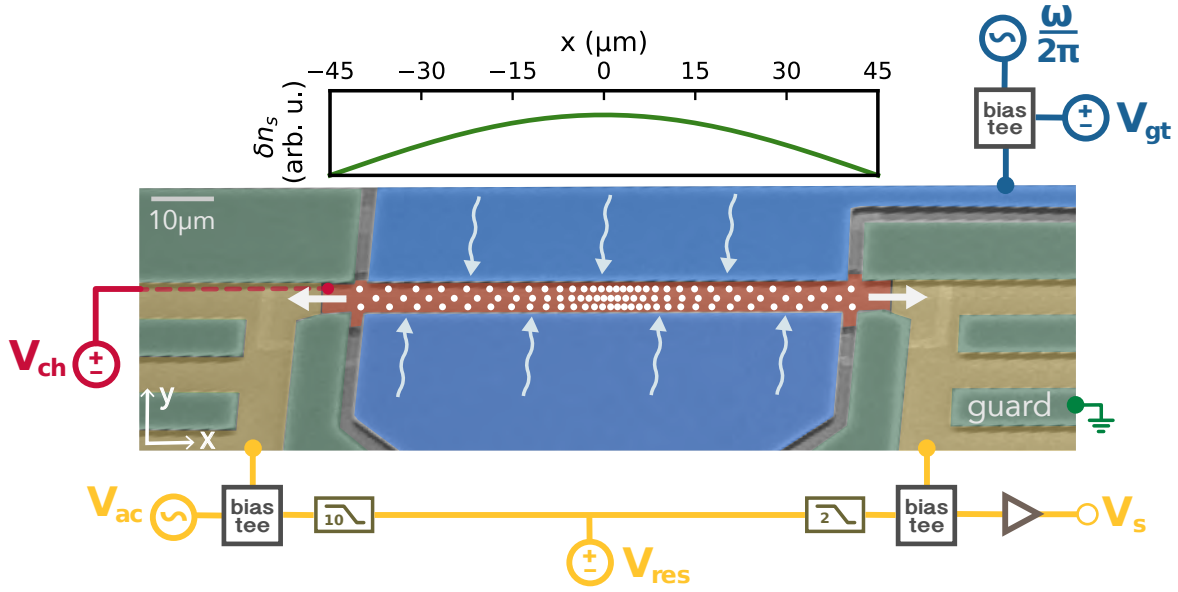


Figure 3.2: False color scanning electron micrograph of the microchannel device. Grounded guard electrodes (green) patterned above a resist layer surround reservoir electrodes (yellow) located beneath. The central microchannel region between the two reservoirs consists of a channel electrode (red) and top side gate electrode (blue). A dc voltage source biases the two reservoir electrodes with low pass filters corresponding to a  $\leq 2$  kHz passband and a  $\leq 10$  kHz passband. An ac voltage  $V_{ac}$  at frequency  $f_{ac}$  drives the electrons (white dots) through the channel and the resulting transport signal  $V_s$  is detected via a lock-in amplifier. A microwave signal with a frequency  $\omega/2\pi$  is applied to the gate electrode to generate longitudinal plasmons in the central channel (the first mode of which is shown schematically by the  $\delta n_s$  plot).

resonant cavity for confined plasmonic modes, i.e. oscillations of the charge density  $\delta n_s$  along the length of the central channel. At the boundaries of the microchannel, electrons are free to enter and exit into the reservoir regions, enforcing charge density nodes at the ends of the channel, as depicted in Fig. 3.2. Because the number of electron rows is  $\gtrsim 10$  in the density regime in which we investigate plasmons, the electrons in the central channel can be modeled as a two-dimensional sheet of charge defined by the electrostatic confinement produced by the electrode voltages. The long and narrow geometry ( $L \gg w$ ) of the central channel ensures a large separation in frequency between plasmons along versus perpendicular to the channel. This allows us to consider only longitudinal plasmon standing-waves along the channel length, which have the following dispersion relation [34, 49, 54],

$$\omega_p^2 = \frac{n_s e^2}{2\varepsilon_0 m_e} \sqrt{q_x^2 F(q_x)}, \quad (3.1)$$

where  $\omega_p$  is the density-dependent frequency of a plasmon having wavevector  $q_x = n\pi/L$  and mode number  $n$ ,  $m_e$  is the electron mass,  $e$  is the electron charge, and  $\varepsilon_0$  is the vacuum permittivity. The wavevector-dependent factor  $F(q_x)$  takes into account the reduction in the electron-electron interaction due to the presence of the nearby metallic electrodes. This screening factor will correspondingly reduce the plasmon frequency [34], and for the geometry of our device we utilize the following phenomenological form for  $F(q_x)$ ,

$$F(q_x) = \frac{1}{2}(\tanh q_x l + \tanh q_x h), \quad (3.2)$$

where  $l = w - w_e$  parameterizes the effective distance of the electron sheet from the surrounding side gate electrodes and  $h = 1.4 \mu\text{m}$  is the height of the electrons above the

bottom channel electrode. The effective width  $w_e$  of the electron system is defined where the parabolic confinement potential of the channel is equal to the chemical potential  $\phi_e$ , i.e.  $\phi(y = w_e/2) = \phi_e$ , as shown in the bottom panel of Fig. 3.3a, which we extract from FEM. For our specific device geometry, which includes laterally defined side gate electrodes, an analytical solution for the screening factor is lacking. However, we find that the phenomenological form presented in Equation (??) captures to good approximation the screening contributions in the long wavelength limit ( $q_x h, q_x l \ll 1$ ), as well as in the limiting case, in which the screening electrodes are moved infinitely far from the electrons in the channel and the unscreened plasmon dispersion is recovered, i.e.  $F(q_x) = 1$ . Using Equation (3.1) and FEM calculations, we find a fundamental ( $n = 1$ ) plasmon mode frequency of  $\omega_p/2\pi \simeq 1.0$  GHz at  $n_s \simeq 2.3 \times 10^{12} \text{ m}^{-2}$ . This lowest frequency mode corresponds to a half-wavelength standing wave of the time-varying change in density  $\delta n_s$  along the channel, as shown in the top panel of Fig. 3.2. In the following section, we discuss how these modes are generated using an additional microwave drive and detected using transport techniques.

### 3.1.2 Transport measurements & microwave excitation

To characterize the electron system in the central microchannel, and its collective dynamics, we utilize a conventional ac transport measurement scheme [65]. In these measurements, an ac voltage  $V_{ac}$  is superimposed on the left reservoir electrode driving electrons from one reservoir to the other via the central channel at a frequency  $f_{ac}$ . The resulting electron transport through the channel is detected from the voltage  $V_s$  induced on the right reservoir electrode, which we measure using standard phase-sensitive lock-in techniques. As described previously, a dc voltage  $V_{ch}$  applied to the channel electrode controls the population of electrons in the central microchannel. In Fig. 3.3b we show a standard transport map as

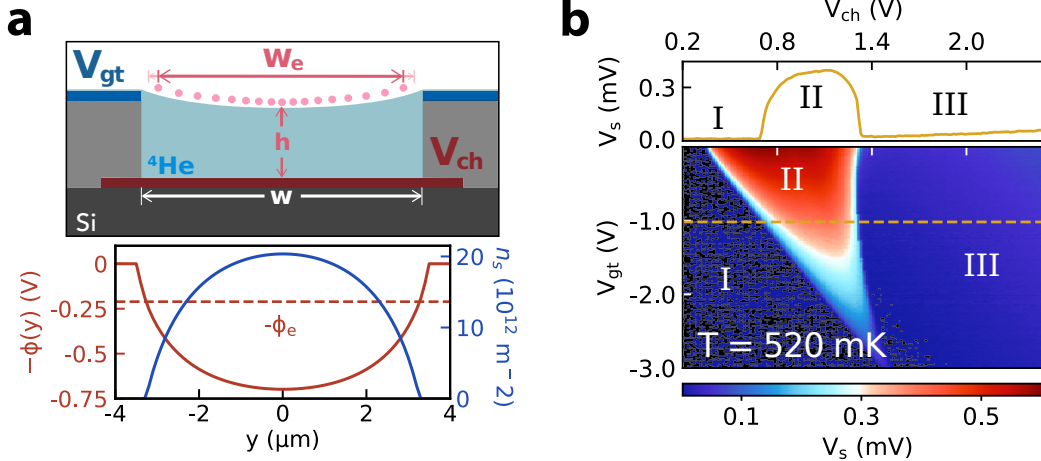


Figure 3.3: (a) Top panel: Schematic cross section view across  $x = 0$  of the channel with a fixed dc bias voltage (i.e. no microwave drive) on the side gate electrode  $V_{\text{gt}}$ . Bottom panel: Electrostatic potential profile,  $\phi(x = 0, y)$ , transverse to the channel (solid red line), with chemical potential  $\phi_e$  (dashed red line), and the distribution of electron density  $n_s(y)$  along the  $y$ -direction (blue line). (b) Transport measurements performed at various values of  $V_{\text{gt}}$ , showing the three characteristic transport regimes. Here,  $V_{\text{res}} = 0.9 \text{ V}$ ,  $V_{\text{ac}} = 20 \text{ mV}$ ,  $f_{\text{ac}} = 1.408 \text{ MHz}$ . See main text for complete description.

we tune the electron density and confinement potential in the central channel. This type of measurement reveals three transport regimes depending on the density of electrons in the central microchannel. In regime I,  $\phi(y = 0) < \phi_e$ , and electrons cannot enter the channel from the reservoirs. When  $\phi(y = 0) = \phi_e$ , the channel threshold voltage  $V_{\text{ch}}^{\text{th}}$  condition is met and electrons can enter the microchannel for  $V_{\text{ch}} \geq V_{\text{ch}}^{\text{th}}$ . In this regime (regime II), the electrons form a highly conducting state in which the electrons interact weakly with the helium surface, resulting in a large transport signal [11]. At sufficiently high density, the electrons in the microchannel form a low-conductivity Wigner solid (regime III) [81]. These measurements also allow us to calculate the electron density in the central microchannel  $n_s$  from the potential in the center of the channel  $\phi^0 \equiv \phi(x = 0, y = 0)$  and the chemical potential  $\phi_e$ , as

$$n_s = \frac{\epsilon_{\text{He}} \epsilon_0}{eh} (\phi^0 - \phi_e), \quad (3.3)$$

where  $\varepsilon_{\text{He}} = 1.057$  is the dielectric constant of liquid helium. Here, the chemical potential is calculated using  $\phi_e = V_{\text{ch}}^{\text{th}} \alpha_{\text{ch}}^0$  [85] and the capacitive coupling constant in the center of the microchannel,  $\alpha_{\text{ch}}^0 \equiv \alpha_{\text{ch}}(x = 0, y = 0) \simeq 0.7$ , is obtained through FEM calculations of the device [66].

To generate plasma oscillations in the electron sheet, we apply a high-frequency signal onto the gate electrodes located on either side of the microchannel as shown in Fig. 3.2. The microwave power modulates the otherwise static confinement potential throughout the microchannel, which leads to a periodic modulation of the effective width  $w_e$  of the electron system (see top panel Fig. 3.2b) and creates charge density oscillations of the electrons in the central microchannel due to the strong Coulomb interaction. The frequency and amplitude of these oscillations are controlled by the gate modulation frequency  $\omega/2\pi$  and microwave signal power  $P$ , which is measured from the output of the high-frequency source. This microwave signal is attenuated by an additional 28 dB before entering the cryostat.

## 3.2 Detection and analysis of plasmon modes

### 3.2.1 Plasmon detection

In Fig. 3.4, we show how the GHz-frequency plasmonic modes of the electrons in the central microchannel are imparted on the transport signal by monitoring  $V_s$  as a function of  $V_{\text{ch}}$  as we increase the power  $P$  of a fixed  $\omega/2\pi = 5.5$  GHz signal applied to the gate electrodes. In these measurements, we observe the three characteristic transport regimes described in the previous section, corresponding to (I) no electrons, (II) a low-density, highly conducting electron state, and (III) a high-density, low-conductivity Wigner solid within the central channel. At increasing microwave power, the electron density  $n_s$  that corresponds to the

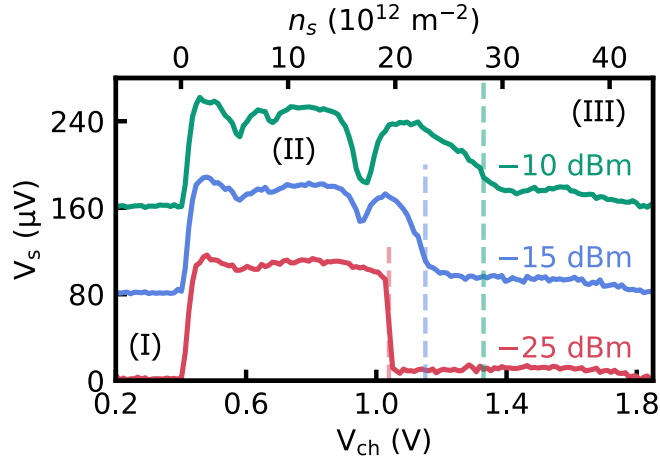


Figure 3.4: Transport detected plasmon resonances. Microchannel transport measurements in the presence of a  $\omega/2\pi = 5.5$  GHz microwave excitation signal on the gate electrode for increasing values of microwave power  $P$ . Traces are offset vertically for clarity and color coded with the corresponding  $P$ . Vertical dashed lines indicate the transition into a low-conductivity Wigner crystal electron state, which increases with increasing  $P$ . At  $P \gtrsim -15$  dBm, resonance-like features appear in regime II, indicating plasmon modes generated along the length of the channel as described in the main text. Measurements were performed at  $T = 18$  mK, with  $V_{\text{gt}} = 0$  V,  $V_{\text{ac}} = 6$  mV,  $f_{\text{ac}} = 3$  MHz, and  $V_{\text{res}} = 0.4$  V.

transition into the low-conductivity Wigner solid regime increases [159], as shown by the vertical dashed lines for each trace, and we find that this type of effect occurs independent of the microwave drive frequency.

More interestingly, with increasing microwave power, we observe the emergence of resonance-like features in the transport signal when the electrons in the microchannel are in the highly conducting state (regime II). Three resonances are clearly visible in the green trace in Fig. 3.4 at  $V_{\text{ch}} = 0.58, 0.68, 0.96$  V corresponding to densities of  $n_s = 5.7, 8.6, 16.9 \times 10^{12} \text{ m}^{-2}$  in the central channel. The resonances appear as local minima in the transport signal indicative of a reduction in the conductivity of the electron system in the central channel.

To understand these experimental features, we must consider the non-linear transport phenomena arising from the coupling of the electrons to the helium surface when the system is subjected to the effects of the ac driving and microwave excitation fields, which drive the

electrons out of equilibrium [50, 67, 68]. We begin by noting that, at  $T \simeq 20$  mK, in the absence of microwave excitation and at low ac drive, the electron system would remain in the low-conductivity regime (III) for all values of the electron density shown in Fig. 3.4. In other words, the *equilibrium* state of the electrons in this case would correspond to the low-conductivity Wigner solid<sup>1</sup>. In this regime, the electrons coherently emit riplons whose wavevectors match the reciprocal lattice vectors of the electron crystal. This phenomenon is known as the resonant Bragg-Cherenkov scattering effect [81]. This effect results in an increased frictional force on the electrons and a saturation of their velocity at the phase velocity of the emitted riplons  $v_{\text{ph}} = \omega_{\text{r}}(G_1)/G_1$ , where  $\omega_{\text{r}}(k) = \sqrt{\sigma_t/\rho \cdot k^3}$  is the ripplon dispersion relation,  $\sigma_t = 358 \mu\text{N/m}$  is the liquid helium surface tension,  $\rho = 145 \text{ kg/m}^3$  is the liquid helium density, and  $G_1 = (8\pi^2 n_s/\sqrt{3})^{1/2}$  is the first reciprocal lattice vector of the Wigner solid. When subjected to high driving fields, the electron system can heat [48] and transition to a non-equilibrium state which has a high conductivity (regime II). This state has been interpreted as the formation of either a disordered electron liquid state [160] (*melting* model) or as a depinning transition of the Wigner solid [11, 27, 28, 159] (*sliding* model). In the sliding model, the transition to the Wigner solid state is associated with the formation of static surface deformations appearing under each electron, referred to as a dimple lattice, which moves together with the electron lattice. When subjected to a sufficiently strong drive, the electron solid can decouple from the underlying dimple lattice and move at higher velocities. In contrast, the melting model does not involve the concept of a dimple lattice; instead, the transition to a high-conductivity regime is interpreted as a transition to a disordered state. Despite the lack of an unambiguous microscopic description of these

---

<sup>1</sup>In this regime the electron system is in equilibrium with the helium bath, thus for an electron temperature  $T_e = 20$  mK the critical density to form a Wigner solid ( $n_s^{\text{cr}} = 8 \times 10^9 \text{ m}^{-2}$ ) is reached for  $(V_{\text{ch}} - V_{\text{ch}}^{\text{th}}) > 0.2 \text{ mV}$ .

nonlinear effects, the transition into the high-conductivity regime (II) strongly depends on the positional order of the electrons in both models. Reducing this order weakens the Bragg-Cherenkov scattering effects and lowers the critical ac driving field required to transition into the high-conductivity state. For the experimental data presented in Fig. 3.4, transport measurements were performed at ac driving fields sufficiently high enough to promote the electrons into the non-equilibrium high-conductivity state for densities  $n_s < 18.8 \times 10^{12} \text{ m}^{-2}$ .

### 3.2.2 Non-equilibrium transport in the presence of microwave excitation

To characterize the non-equilibrium transport response of the electron system in the presence of the microwave excitation field, we perform a series of ac drive dependent transport measurements with and without simultaneous microwave power applied to the side gate electrodes. Fig. 3.5a shows the density dependent transport through the central microchannel with increasing ac drive amplitude and with no microwave excitation on the side gate electrode. At low ac drive ( $V_{ac} < 12 \text{ mV}$ ), the electron system remains in a low-conductivity Wigner solid state for all values of the electron density shown in Fig. 3.5a. In this regime, the electron velocity saturates at the ripplon velocity. At  $V_{ac} \simeq 12 \text{ mV}$ , the electron system conductivity abruptly increases, indicative of the transition into a high-conductivity state of the electron system, which can be interpreted as either an unpinned Wigner solid or a disordered electron liquid [11, 27, 28, 48, 159, 161, 162].

In Fig. 3.5b we present a similar ac drive dependent transport measurement but with a  $\omega/2\pi = 5.5 \text{ GHz}$  microwave tone applied to the side gate electrode. The presence of the  $n = 3$  plasmon mode appears as a reduction in the measured transport signal (solid purple

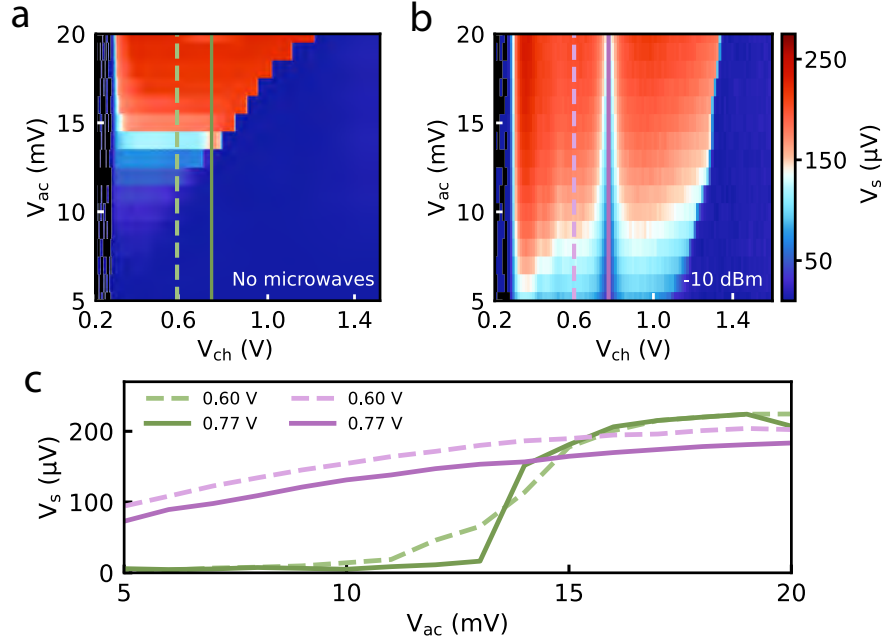


Figure 3.5: Drive-dependent transport measurements at  $T = 16$  mK with and without microwave side gate excitation. (a) Density-dependent microchannel transport with increasing ac drive voltage,  $V_{\text{ac}}$ , with no microwave power applied to the side gate electrode. This measurement was performed at  $f_{\text{ac}} = 3$  MHz,  $V_{\text{res}} = 0.7$  V, and  $V_{\text{gt}} = 0$  V. Green dashed ( $V_{\text{ch}} = 0.6$  V) and solid ( $V_{\text{ch}} = 0.77$  V) lines correspond to the linecuts plotted in (c). (b) Transport measurements similar to those presented in panel a) except with the additional application of a  $\omega/2\pi = 5.5$  GHz microwave tone applied to the side gate electrode with  $P = -10$  dBm. Purple dashed ( $V_{\text{ch}} = 0.6$  V) and solid ( $V_{\text{ch}} = 0.77$  V) lines correspond to the linecuts plotted in (c). (c) For additional clarity we show vertical line cuts of the transport signal from panel (a) (green dashed and solid) and panel (b) (purple dashed and solid).

line). Additionally, and in contrast to the case with no microwave excitation (Fig. 3.5a), the non-linear Bragg-Cherenkov regime is not observed down to the lowest levels of ac drive for which we are able to perform transport measurements. Rather, we observe a steady increase in the transport signal with increasing ac drive amplitude both on and off resonance (see purple linecuts in Fig. 3.5c), which is consistent with the heating of an underlying electron liquid state.

The application of the additional microwave excitation field onto the side gate electrodes further perturbs the electron system. In the Wigner solid state, these perturbations induce high-frequency electron motion, which in a quasi-static approximation ( $\omega \gg \omega_T$ ) can be viewed as a weakening of the positional order of the electron solid. As a result, the transition into the low-conductivity Bragg-Cherenkov scattering regime shifts to higher in densities with increasing amplitude of the perturbing field. This effect is analogous to raising the temperature of the electron system  $T_e$ , which characterizes the melting of the solid. Due to the large electron-electron collision rate ( $10^{11} \text{ s}^{-1}$ ) and small energy relaxation rate ( $10^5 - 10^6 \text{ s}^{-1}$ ), the electron system temperature can be raised above that of the helium bath [163]. In this way, the perturbing field effectively melts the Wigner solid leading to a transition into the high-conductivity regime. The ultimate electron temperature produced by the microwave field is determined by a balancing of the incident microwave and ac drive field powers with the energy transferred into the helium bath via the emission of short-wavelength ripplons and phonons. Due to the complex geometry of the device, which includes multiple regions with varying electron density, and the lack of information about how much of the incident microwave power is absorbed by the electron system, estimating  $T_e$  is unfeasible. Nonetheless, a qualitative approach can be employed to interpret the decrease in the measured transport signal at the position of the resonances shown in Fig. 3.4.

Independent of the underlying microscopic state of the electron system in regime II, the microwave energy absorbed by the electrons increases when plasmons are resonantly excited, which results in additional heating of the electron system on resonance. Since the resonances appear in the high-conductivity regime (II), an additional increase in  $T_e$  can be understood as producing an increase in the electrons' momentum transfer rate to ripplons, leading to a reduction in the mobility of the electron liquid state [48]. This is consistent with the observed decrease in the measured signal on resonance. We note that, in principle, the reduction in the measured transport signal on resonance could also be interpreted as a transition from a unpinned Wigner solid into the Bragg-Cherenkov non-linear regime. However, our experiments indicate that in the presence of microwave excitation, the high-conductivity regime consistently remains in a linear transport regime, indicative of an electron liquid state.

The transport measurements presented in Fig. 3.4, conducted with an additional perturbing microwave field, reveal the high sensitivity of the measured signal to the presence of plasmonic excitations in the electron system confined within the microchannel. These experiments underscore the complex nature of the non-equilibrium and nonlinear response of this strongly correlated low-dimensional electron system coupled to the helium surface excitations and enrich the extensive body of research on these topics [27, 28, 48, 67, 68]. Despite the absence of an unequivocal microscopic picture of the electron conductivity in these regimes, we can leverage the sensitivity of these measurements to investigate the plasmonic excitations we generate in the central microchannel. Finally, we note a similar technique has recently been employed to detect the excitation of Rydberg-like resonances of electrons on helium due to resonant microwave heating [50].

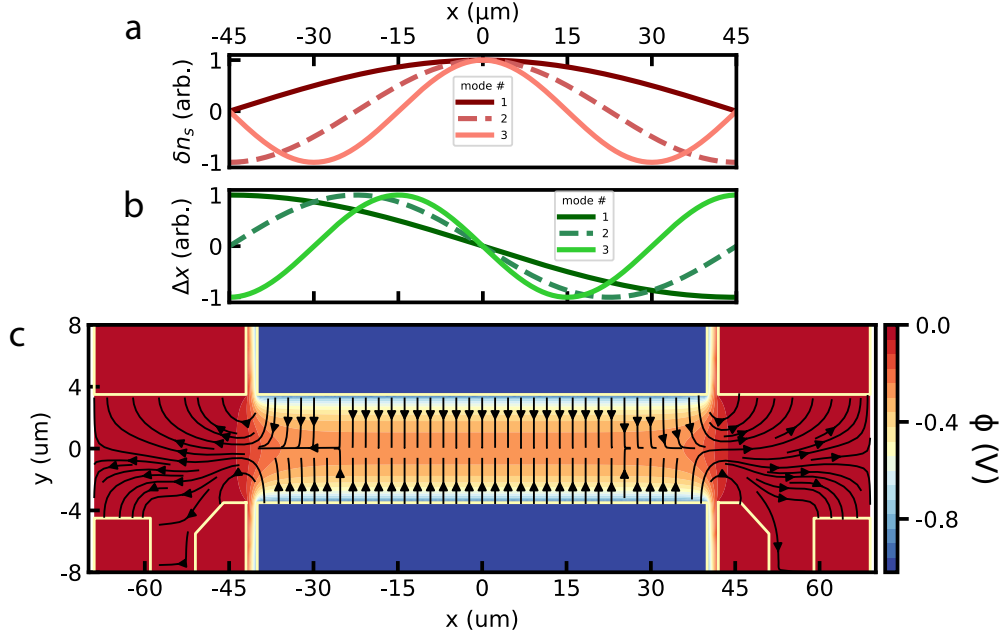


Figure 3.6: Plot of how the first three plasmon modes will manifest (a) in terms of the change in areal electron density  $\delta n_s$  along the channel and (b) in terms of the change in electron displacement  $\Delta x$  along the channel. The odd modes ( $n = 1$  and  $n = 3$ ) are represented by solid lines and the even mode ( $n = 2$ ) by a dashed line. (c) Plot of the microwave potential in the region of the central microchannel with corresponding electric field lines (black lines with arrows) calculated from FEM simulations. The plot shows how the field lines terminate on the various areas of the device, promoting a stronger coupling to odd versus even plasmon modes.

### 3.2.3 Plasmon mode generation and coupling

In the experiments, plasmons are generated via a microwave excitation signal applied to the gate electrode (colored blue in Fig. 3.6c). The coupling between the microwaves and plasmons in the central channel is determined by the dot product of the electric field distribution generated by top gate electrodes and electron displacement field  $\int(\vec{E} \cdot \vec{\Delta x})dx dy$ . In Fig. 3.6 we schematically plot the spatial distribution of the charge density displacement  $\delta n_s$  (Fig. 3.6a) and corresponding electron position displacement  $\Delta x$  (Fig. 3.6b) for the first three longitudinal plasmon modes along the channel, as well as the electric field distribution calculated using FEM (Fig. 3.6c). For longitudinal plasmon standing-waves along the chan-

nel length, the primary contribution to the coupling comes from the regions near the channel ends, where the  $x$ -component of the microwave electric field is nonzero. The symmetry of the electric field also determines which modes couple more efficiently: modes with position displacement values of opposite sign at the channel ends — corresponding to odd-numbered modes — are more readily excited by microwave fields applied to the gate electrode. We also note that, in principle, the electric field configuration within the channel allows for the excitation of transverse modes. These plasmons correspond to the optical branch of the plasmon excitation spectrum, with frequency increasing as the wavevector increases and a finite frequency gap in the limit of small wavevector, which is set by transverse confining potential frequency  $\omega_t$  (for number of rows  $N_y \geq 2$ ) [164]. For the voltage ranges used in our experiments, we estimate  $\omega_t/2\pi > 10$  GHz, making the excitation of transverse modes unlikely.

### 3.2.4 Analysis of plasmon mode structure

In Fig. 3.7a we show the full channel density and microwave frequency dependence of the transport signal through the device. In regime II, we observe a family of density-dependent resonances in the channel, which are consistent with the long-wavelength two-dimensional longitudinal plasmons described by Eq. (3.1). To analyze these plasmon modes, we extract the local transport minima along each of the first seven resonances (blue dots in Fig. 3.7b) and compare them to the calculated values of  $\omega_p$  using Eq. 3.1 and our device geometry parameters (red dashed lines). In this calculation, the effective width  $w_e$  of the electron system and the corresponding central microchannel electron density  $n_s$  are calculated using FEM for each value of  $V_{\text{ch}}$ . As shown in Fig. 3.7b, we find good agreement between our data and the two-dimensional screened plasmon model for the fundamental mode and its first six

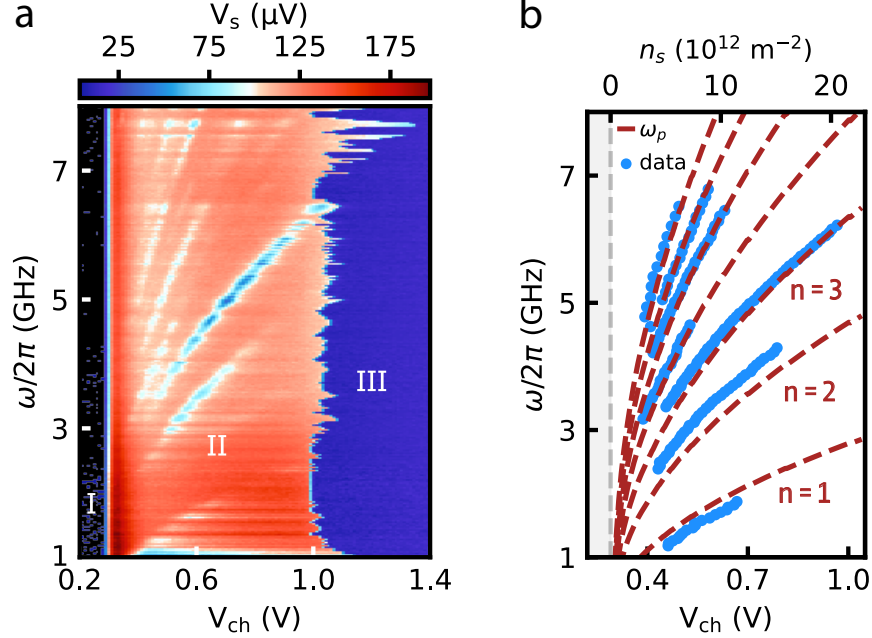


Figure 3.7: Characterization and tuning of plasmon modes. (a) Microwave frequency dependent transport map. Transport measurements are performed by sweeping  $V_{\text{ch}}$  to control the electron density in the central channel while simultaneously applying a microwave signal  $\omega/2\pi$  to the gate electrodes. For  $V_{\text{ch}} \lesssim 0.29$  V, the channel is empty (I). Above  $V_{\text{ch}}^{\text{th}}$  electrons can enter the microchannel and form a low-density high-conductivity state (II) and high-density low conductivity Wigner solid (III). The transport signal  $V_s$  reveals a family of density and frequency dependent plasmon resonances that manifest as local minima in regime II. Measurements were performed at  $P = -15$  dBm, with  $V_{\text{gt}} = 0$  V,  $V_{\text{ac}} = 8$  mV,  $f_{\text{ac}} = 3$  MHz,  $V_{\text{res}} = 0.29$  V, and  $T = 26$  mK. (b) Blue dots are the extracted local minima from the first seven resonances in (a). Red dashed lines correspond to the first seven longitudinal plasmon modes along the channel, calculated using the dispersion relation given in Equation (??) with our device design parameters. Grey shaded region indicates the empty channel (I) and grey dashed line indicates  $V_{\text{ch}}^{\text{th}} = 0.29$  V.

harmonics. The results reveal plasmon modes in a frequency range compatible with cQED systems, and that their frequency can be electrostatically tuned over an extremely broad range ( $\simeq 2 - 3$  GHz) by controlling the areal density of electrons. We note that the most pronounced modes in Fig. 3.7a correspond to odd harmonics. This effect can be understood as arising from a preferential coupling between the microwave excitation field and plasmon modes that have charge density nodes at the ends of the microchannel, as discussed in the previous section.

The data show the resonances appearing only in regime II, and not in the low-conductivity Wigner solid (regime III). This is consistent with a significant reduction of the charge density oscillation frequency arising from the phononic modes of the crystal when they are coupled to the elementary excitations of the helium surface (rippions). In the long wavelength limit, this coupling to ripples reduces the bare longitudinal plasmon frequency by a factor of  $\sqrt{m/m^*}$  [57], where  $m^* \gtrsim 100m_e$  parameterizes the effective mass of electrons on helium in the Wigner solid state [22]. Finally, we note the data in Fig. 3.7b show the transition to the low-conductivity Wigner solid state is significantly non-uniform as a function of microwave drive frequency. This non-resonant effect could be associated with the absorption of microwave energy by other parts of the device, e.g. the resist layer between the top and bottom electrodes or variable microwave transmission due to impedance mismatches in the drive line.

### 3.2.5 Power dependence of plasmon modes

The measurements presented in Fig. 3.8a show how increasing microwave power modifies the transport characteristics and plasmon response at a fixed microwave excitation frequency of 5.5 GHz. Here, the transition between the high-conductivity (regime II) and Wigner solid (regime III) states shifts to higher electron density as the microwave power increases, indicating a weakening of the positional order of the Wigner solid, as discussed earlier. Additionally, as the channel density is varied, the 5.5 GHz microwave drive generates the  $n = 7, 5,$  and  $3$  plasmon modes (from left to right, respectively), which manifest and broaden with increasing power. As it is the most prominent, we will focus on the  $n = 3$  mode centered at  $V_{\text{ch}} \simeq 0.96$  V for the remainder of the analysis in this section.

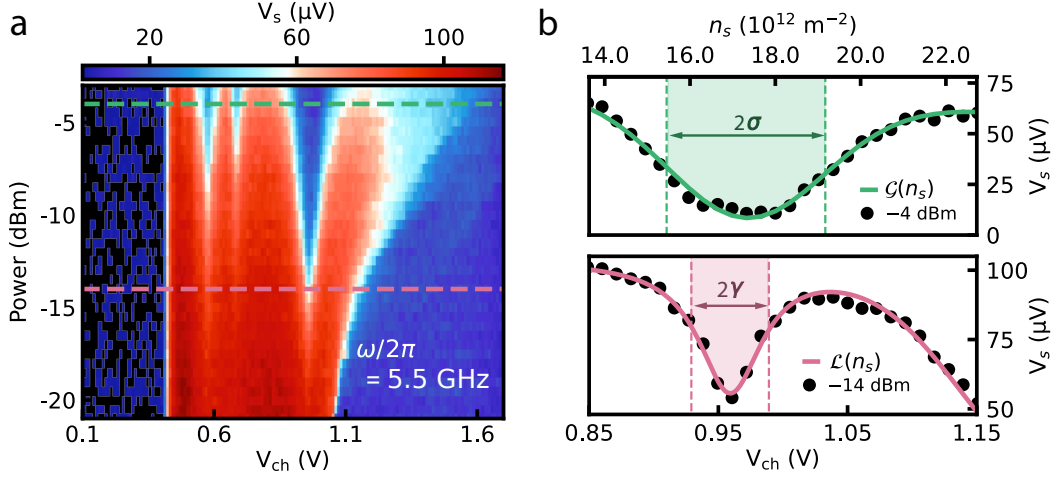


Figure 3.8: (a) Microwave power dependent transport measurements at fixed excitation frequency  $\omega/2\pi = 5.5$  GHz. With increasing power the resonant plasmon modes broaden significantly. Measurements were performed at  $V_{ac} = 6$  mV,  $f_{ac} = 3$  MHz,  $V_{gt} = 0$  V,  $V_{res} = 0.4$  V, and  $T = 18$  mK. (b) Linecuts of the  $n = 3$  plasmon mode, corresponding to the horizontal dashed lines in (a). Depending on the applied microwave power, the plasmon resonances are fit to either a Lorentzian or Gaussian, superimposed on a smoothly varying background function (see Supplementary Information, section IV).

### 3.2.5.1 Evolution of the plasmon lineshape

In Fig. 3.8b, we show linecuts of the data at low and high microwave power. At low power ( $P = -14$  dBm), we find the data is well described by a Lorentzian of width  $2\gamma$  while at high power ( $P = -4$  dBm) the resonance is captured by a Gaussian having a linewidth of  $2\sigma$ . We also take into account the background transport signal with the addition of a logistic function, which we find phenomenologically captures the smoothly varying density-dependent background. The composite fitting function containing the Lorentzian distribution has the following form,

$$\mathcal{L}(n_s) = \frac{\gamma}{\pi[(n_s - n_{s0})^2 + \gamma^2]} + A \left[ 1 - \frac{1}{1 - e^{(n_s - n_{s1})/\alpha}} \right], \quad (3.4)$$

where  $2\gamma$  is the full-width at half-maximum of the Lorentzian,  $n_{s0}$  is the density at which

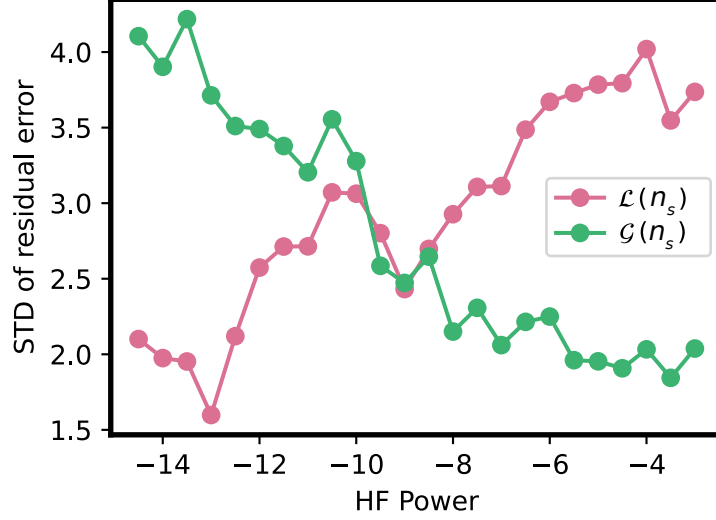


Figure 3.9: Standard deviation of the residual error from fitting each transport linecut from  $P = -14.5$  dBm to  $P = -3$  dBm of Fig. 3.8 to  $\mathcal{G}(n_s)$  (green dots) and to  $\mathcal{L}(n_s)$  (pink dots).

the resonance feature is centered and  $\{A, n_{s1}, \alpha\}$  are phenomenological fitting parameters describing the logistic function. The electron densities are mapped from the corresponding values of  $V_{\text{ch}}$  in the transport data, calculated using Eq. 3.3. The composite function containing the Gaussian distribution, which we find fits the high power data better, has the form

$$\mathcal{G}(n_s) = \frac{e^{-(n_s - n_{s0})^2 / 2\sigma^2}}{\sigma\sqrt{2\pi}} + A \left[ 1 - \frac{1}{1 - e^{(n_s - n_{s1})/\alpha}} \right]. \quad (3.5)$$

where  $2\sigma$  is the linewidth of Gaussian distribution and the second term describes the background signal in a similar way as in Eq. 3.4. In Fig. 3.9, we show how the standard deviation of the residual error evolves when fitting all the microwave power-dependent transport data (Fig. 3.8) to  $\mathcal{L}(n_s)$  (pink) and to  $\mathcal{G}(n_s)$  (green). We find that plasmon resonance features measured at microwave powers  $P < -10$  dBm are better represented with the Lorentzian-like function, while at higher powers, the Gaussian-like lineshape provides a better description of the data.

### 3.2.5.2 Sources of plasmon broadening

In general, the spectral linewidth and its power dependence contain information about intrinsic and inhomogeneous sources of plasmon broadening. In what follows, we discuss possible sources of broadening including static and dynamic density inhomogeneity of the charge carriers in and around the channel as well as plasmon energy loss.

To begin, the application of the microwave field can lead to a non-equilibrium redistribution of charge carriers inside the channel and could be responsible for the plasmon broadening we observe with increasing microwave power. In fact, previous experiments with electrons on helium have demonstrated a transient redistribution of electrons arising from resonant photovoltaic effects [165]. We also note that the long and narrow aspect ratio of the central channel creates an electron density profile that varies transverse to the length of the channel as shown in Fig. 3.3a, where we plot the density along the y-direction determined from FEM. If we ascribe the broadening of the low power plasmon spectrum exclusively to static inhomogeneity in the electron density, the observed linewidth of the resonance feature corresponds to a density variation of  $1.8 \times 10^{12} \text{ m}^{-2}$ . This is significantly smaller than the full density variation transverse to the channel, indicating that a static density inhomogeneity is likely not the dominant mechanism contributing to the plasmon broadening at low powers. However, it is possible that non-uniform heating of the electron system by the microwave excitation could enhance static density inhomogeneities in the channel and contribute to the plasmon broadening we observe with increasing power.

Additionally, collective excitations such as plasmons are naturally sensitive to the boundary conditions imposed by their environment. The boundary conditions for longitudinal plasmons excited along the channel are determined by the difference in density and con-

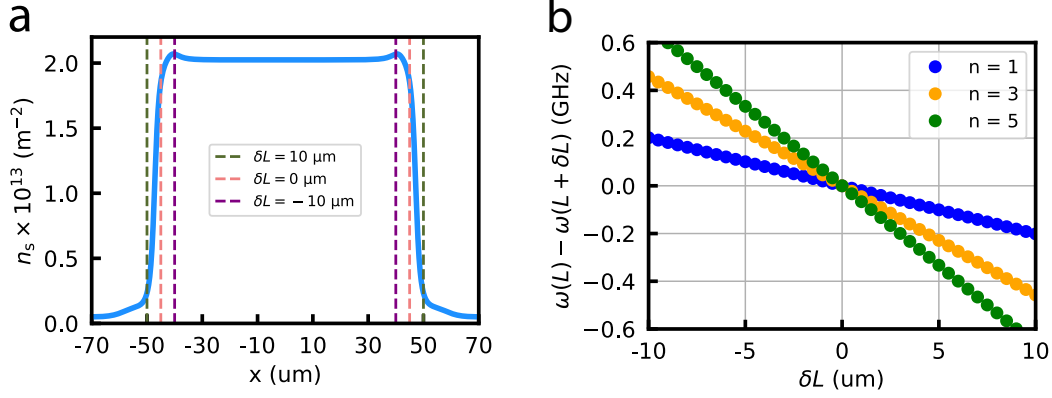


Figure 3.10: (a) Plot of the density along the length of the channel for  $V_{\text{ch}} = 0.96$  V with vertical dashed lines indicating the change in the channel length. The pink dashed vertical line corresponds to the actual length of the channel,  $L = 90$   $\mu\text{m}$ . (b) Plot showing how the plasmon frequency for a given mode ( $n = 1, 3,$  or  $5$ ) will vary for different variations in channel length  $\delta L$  using Eq. 3.6.

ductivity between the electrons in the central channel and those in the reservoir regions of the device. At the ends of the central channel, the electron density varies smoothly over a distance of approximately  $\delta L = 10$   $\mu\text{m}$ , leading to an uncertainty in the plasmon wavelength (see Fig. 3.10a). Using the plasmon dispersion relation in Eq. 3.1, which depends on the length of the channel,  $\omega_p(L)$ , we can understand how perturbations in the channel length will effect the plasmon frequency for a given mode by Taylor expanding  $\omega_p(L)$  up to the first term in  $\delta L$ . This Taylor expansion is given by

$$\omega_p(L + \delta L) = \omega_p(L) - \frac{n_s e^2}{4m_e \epsilon_0 \omega_p(L)} \left[ \frac{q_x}{L} \sqrt{F(q_x)} + \frac{q_x^2}{4L \sqrt{F(q_x)}} \left( l \operatorname{sech}^2(lq_x) + h \operatorname{sech}^2(hq_x) \right) \right] \delta L. \quad (3.6)$$

The difference in plasmon frequency for a given mode from Eq. 3.6 is plotted in Fig. 3.10b. For a  $\delta L = 10$   $\mu\text{m}$ , the corresponding uncertainty in the plasmon frequency would be approximately 400 MHz, which is the same order of magnitude as the plasmon linewidth we observe

at low microwave power. In particular, if we use the plasmon dispersion relation to convert the width of the plasmon mode in  $V_{\text{ch}}$  to a frequency, at low power ( $P = -14$  dBm) the  $n = 3$  mode linewidth corresponds to  $2\gamma = 280$  MHz, while for the high power ( $P = -4$  dBm)  $n = 3$  mode, the linewidth corresponds to  $2\sigma = 570$  MHz. Furthermore, as the microwave drive power is increased, additional broadening could result from a dynamical redistribution of charge carriers in the vicinity of this boundary. Another possible broadening mechanism is the finite transparency at the boundary on either end of the microchannel. In this scenario, plasmon damping results from a leakage of the charge density wave from the central channel to the electron system in the reservoirs and subsequent thermalization [166]. In addition, it has been proposed that plasmon damping can arise from the difference in the conductivity between the channel and reservoir electron systems [167].

Lastly, it is also important to consider the intrinsic energy losses of the plasmon modes. In this system, energy loss can arise from the screening currents in the lossy resistive metallic gate electrodes, as well as from interactions with the helium surface vibrational modes (ripples) and phonons in the liquid, which are the dominant energy and momentum relaxation mechanisms at the relevant experimental temperatures ( $T \lesssim 0.8$  K). In the absence of inhomogeneous effects these losses should dominate the plasmon linewidth. If we assume that the low power ( $P = -14$  dBm) broadening arises predominately from intrinsic losses, we estimate a lower bound for the plasmon lifetime  $\tau_p \sim 1$  ns.

### 3.2.6 Reservoir dependence of the resonance features

To instill confidence that the plasmon resonances we observe in the transport are occurring only in the central microchannel region, we can perform reservoir dependent transport at fixed microwave frequency. This measurement is shown in Fig. 3.11 at  $\omega/2\pi = 4.22$  GHz.

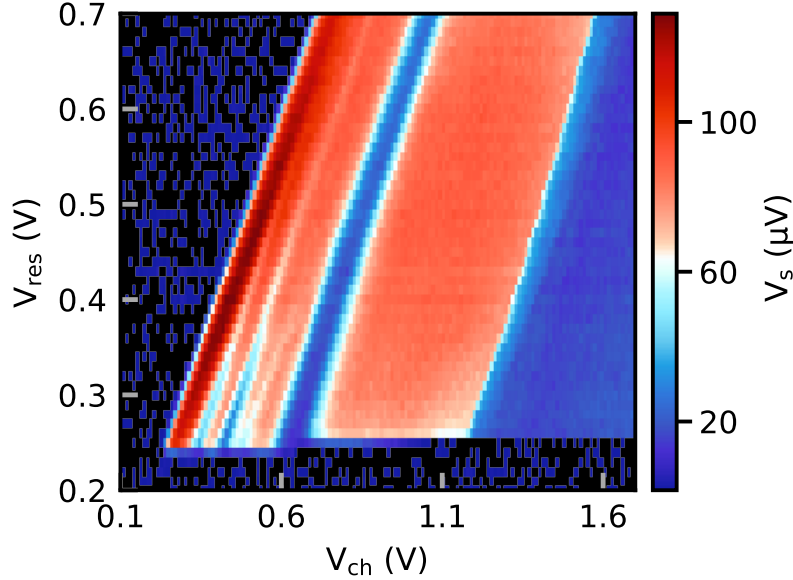


Figure 3.11: Reservoir dependent microwave frequency transport data. Transport measurements are performed at fixed microwave frequency  $\omega/2\pi = 4.22$  GHz, while the reservoir voltage  $V_{\text{res}}$  is varied. Here we see as the reservoir voltage decreases, the channel threshold  $V_{\text{ch}}^{\text{th}}$  decreases, as expected. We also see the plasmon resonance features follow the threshold, confirming the plasmon modes are occurring within the central microchannel. At  $V_{\text{res}} = 0.24$  V, we lose electrons. This measurement was taken at  $T = 17$  mK, with  $f_{\text{ac}} = 3$  MHz,  $V_{\text{ac}} = 5$  mV, and  $P = -8$  dBm.

As the reservoir voltage is decreased, we see the threshold decrease as expected, and we also see the plasmon resonance features follow that threshold line. This indicates that we are exciting plasmons only in the central microchannel.

Throughout this section thus far, we have only presented data showing the plasmon resonance features manifesting in the transport data as an overall decrease in the electron conductivity. However, we have also observed these features manifest as an overall increase in the electron conductivity. This is shown in the data presented in Fig. 3.12. We find that the conductivity response of the resonance signal depends on the electron system saturation in the reservoirs. In Fig. 3.12a-b, we perform microwave power dependent transport data (similar to the data in Fig. 3.8), where in Fig. 3.12a we see the plasmons appear as increases in the conductivity and in Fig. 3.12 they appear as the familiar decrease in conductivity.

Both measurements were performed at the same microwave frequency and reservoir voltages, however between the measurement in panel (a) and the measurement in panel (b), some amount of electrons were lost from the reservoir regions of the device. This is indicated by the shift in the threshold voltage between the two sets of data (vertical white dashed line).

In general, we have understood the manifestation of the plasmon features as a response to the resonantly heated electron system, where the system melts and we see the resulting increase in conductivity on resonance. However, in our attempt to understand the transport signal response, we neglected the significance of the state of the electrons in the reservoirs. From the data in Fig. 3.12a-b, we find that the reservoir electrons play an integral role in the transport signal we observe. When the electron system in the reservoirs is saturated, we expect higher overall densities, while at lower saturation we expect lower densities. We speculate that the difference in observed plasmon features between the high versus low saturation is a consequence of how efficiently the thermally excited plasmons in the channels heat the electrons in the reservoirs. In particular, if the reservoir electrons are in the highly dense crystallized state, when the crystallized electrons are heated, that will correspond to an increase in the electron mobility. In contrast, if the electrons in the reservoirs are in the liquid state, the heating would cause the mobility to decrease [54]. This physical picture is consistent with what we observe in the highly saturated reservoir case in Fig. 3.12a, where we see the signal increase on resonance, as well as with what we observe in the low saturated reservoir case in Fig. 3.12b, where we see the signal decrease on resonance.

These measurements provide deeper insight into how we are able to detect the plasmons via transport measurements and indicate the significant role the reservoirs play in transport measurements. We also point out that further measurements of this type could help uncover the unresolved microscopics of the sliding versus melting of the electron crystal discussed in

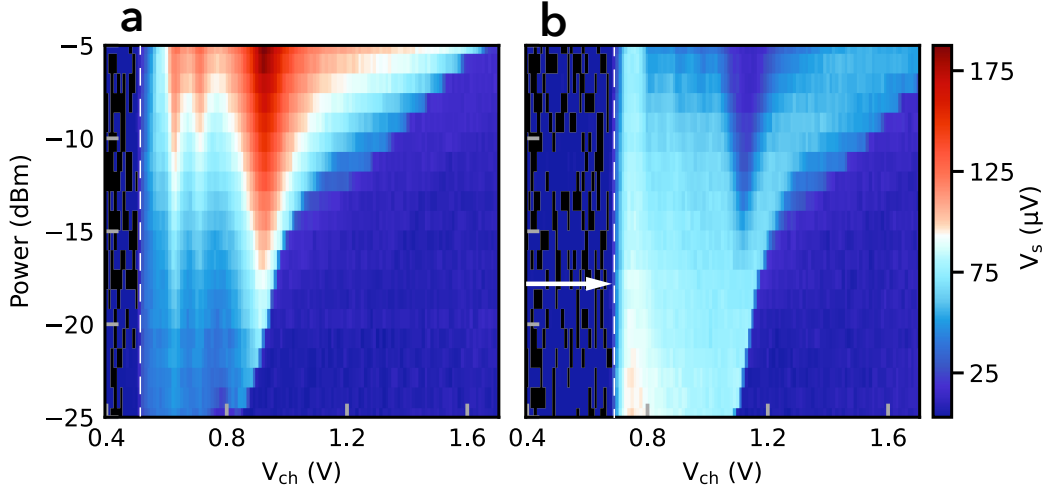


Figure 3.12: Microwave power dependent transport measurements at fixed frequency  $\omega/2\pi = 5.22$  GHz, with  $V_{\text{res}} = 0.7$  V and at  $T = 17$  mK. (a) Plot shows the plasmon mode resonance features manifesting as an *increase* in transport signal with a  $V_{\text{ch}}^{\text{th}} = 0.5$  V (vertical white dashed line). (b) Microwave power dependent transport data taken again after losing some amount of electrons from the reservoirs, indicated by the shift in the threshold ( $V_{\text{ch}}^{\text{th}} = 0.7$  V, vertical white dashed line). Plot shows plasmon mode resonance features manifesting as a *decrease* in transport signal.

Sec. 2.3.3.1.

### 3.2.7 Consideration of the one-dimensional dispersion relation

Throughout the analysis here, we have utilized a two-dimensional plasmon dispersion relation (Eq. 3.1) to study the density dependence of the plasmon resonance frequencies extracted from the experimental data (as shown in Fig. 3.7). While this expression is relevant for the density range over which we observe plasmons in the microchannel device, it is instructive to also discuss the case of a one-dimensional plasmon, which could in principle be realized in the limit of low electron density and tight spatial confinement.

In the low-density limit, the electron system can form a single electron chain due to the constraints imposed by the confining potential of the central microchannel. The problem of the plasmon dispersion for a single linear row of electrons is analytically solvable [164] and,

for a screened Coulomb interaction, is given by:

$$\omega_1^2(q) = \frac{e^2}{4\pi\epsilon_0 m_e} n_l q^2 \left[ \frac{3}{2} + \ln \frac{n_l}{\kappa} \right]. \quad (3.7)$$

Here,  $q = n\pi/L$  is the plasmon wave number associated with mode number  $n$  and channel length  $L$ ,  $n_l$  is the linear density of the electron chain, and the parameter  $\kappa = 1/\lambda$  is the reciprocal of the screening length  $\lambda$ . This expression only strictly applies for the case of a single electron chain and we note that in our experiments the number of electron chains increases with increasing channel electrode bias voltage  $V_{\text{ch}}$ . However, for the sake of comparison, we can assume that at low density (i.e. in the vicinity of the threshold voltage  $V_{\text{ch}} \gtrsim V_{\text{ch}}^{\text{th}}$ ) the plasmons in the microchannel can be described by the excitations of individual electron chains having a dispersion given by Eq. 3.7. This simplification allows us to compare a quasi-one-dimensional model with our experimental data as well as the two-dimensional plasmon dispersion given by Eq. 3.1 in the main manuscript. In Fig. 3.13a, we plot Eq. 3.7 along with the data and the two-dimensional screened dispersion relation  $\omega_p$  from Eq. 3.1. As shown in the figure, we find that the simplified single electron chain model and the two-dimensional plasmon dispersion tend to converge at low electron density. As expected, we also find that as the density increases, and the system becomes more two-dimensional, the simplified single electron chain model only very roughly agrees with our data. In particular the scaling of the plasmon harmonics and the density dependence are not well-captured by the one-dimensional dispersion. In contrast, the fully two-dimensional plasmon dispersion relation more accurately captures the observed resonances. These results are also consistent with the dimensionality of the electron system inferred from the melting properties of a microchannel confined Wigner solid. The ground state electron configuration

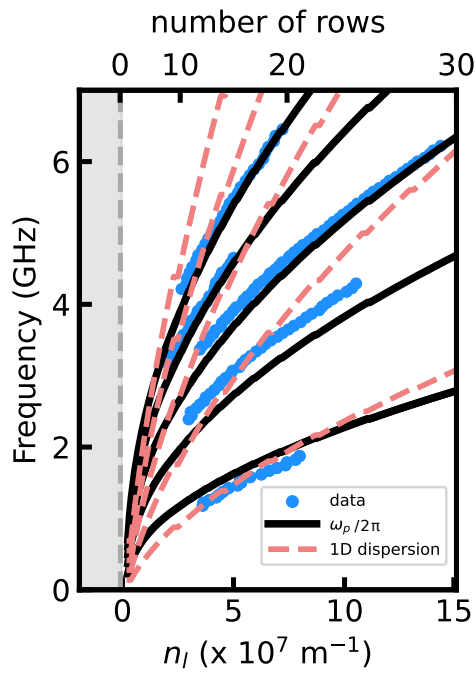


Figure 3.13: Comparison of the one-dimensional plasmon dispersion relation from Eq. 3.7 to the dispersion relation used in the main text  $\omega_p$  (solid black lines) along with the data (blue dots) for the first five plasmon modes. The linear electron density  $n_l$  and the number of electron rows are calculated using FEM.

of a non-degenerate two-dimensional electron system is determined by the plasma parameter  $\Gamma = e^2 \sqrt{\pi n_s} / 4\pi \epsilon_0 k_B T$  – the ratio of the Coulomb potential energy to the mean kinetic energy. When  $\Gamma < \Gamma_c^{2D} = 130$ , the thermal fluctuations dominate and the electron system behaves like a fluid, while above the critical value of  $\Gamma_c^{2D}$ , a two-dimensional Wigner solid forms. Previous transport experiments on microchannel confined electron systems [66, 161] have shown that the melting of the Wigner solid is well-described by a value of  $\Gamma_c^{2D}$  for a number of electron rows in the channel  $N_y \gtrsim 10 - 20$ , while for small numbers of rows the critical plasma parameter is suppressed. Finally we note that, in our experiments we do not observe plasmons until  $V_{\text{ch}} \simeq 0.45$  V, which corresponds to an electron row number across the channel of  $N_y \simeq 10$  according to FEM calculations. For this number of rows the thermodynamic properties of the electrons in the microchannel are consistent with the properties of a two-dimensional electron system.

### 3.3 Summary of results

In summary, we have demonstrated a microchannel device architecture that enables us to precisely engineer spatially-confined microwave frequency plasmonic modes in electrons on helium. The generation of these plasmons resonantly drives the electron system out of equilibrium, which we detect via low-frequency ac transport measurements of the device conductivity. Precise control over the electrostatic environment of the microchannel-confined electrons enables a tunability of the plasmon modes over a frequency range of  $\sim 3$  GHz and we find good agreement between the observed plasmonic mode structure and the two-dimensional screened plasmon dispersion relation. Power-dependent measurements allow us to explore the interplay between the microwave drive and the non-equilibrium plasmon

response in the device and could open the door to investigate plasmon dynamics in the hydrodynamic regime [168].

The high degree of spatial control and broad microwave frequency tunability provided by this type of microchannel device offers a compelling framework for integrating charged collective oscillations of electrons on helium with circuit quantum electrodynamic systems. Devices utilizing an improved and optimized microwave environment will ultimately be needed for future cQED experiments with ensembles of electrons on helium. Placing many-electron on helium systems into high-quality factor microwave cavities opens entirely new avenues for exploring cavity optoplasmonics with collective modes in both the Coulomb liquid and solid phases. Similarly, integration with charge sensitive superconducting qubits [169] would enable fast readout of individual and collective electron dynamics and could be used to reveal the microscopic breakdown in the coupling of the electrons to the quantum field of helium surface waves [11, 162]. Alternatively, hybrid systems composed of electrons on helium coupled to superconducting qubits could be used as a model system for understanding qubit decoherence produced by charged fluctuators [170, 171] in a systematic and tunable fashion.

# Chapter 4

## Coupling plasmons in electrons on helium to superconducting resonators

Circuit quantum electrodynamics (cQED) has been an effective framework to investigate light-matter interactions at the single particle level, coupling two-level systems to high quality factor superconducting resonators [112, 172, 173]. Due to the quantum mechanical nature of these types of hybrid systems, the ability to manipulate the two-level systems via the cavity, and the realization of strong coupling, cQED-based superconducting qubits have been a successful platform for building quantum processors [174–178]. Moreover, as discussed in Sec. 2.5.1, the cQED architecture has also been used to develop charge qubits based on single trapped electrons on helium and on solid neon [74, 104, 113–116]. More broadly, these techniques can be used to investigate light-matter interactions and extended to investigate many-body condensed matter systems, by coupling collective degrees of freedom to quantum circuits [179]. This has been done in a variety of systems, including spin ensembles in nitrogen vacancy centers [152, 153] and in semiconductor systems [180], as well as in trapped ion ensembles [181–183], and with superconducting qubits and phononic modes [151, 184]. We also note early work demonstrating electrons on helium in superconducting resonator devices has been investigated in Ref. [39].

Here, we present progress on developing a novel many-body cQED architecture, coupling

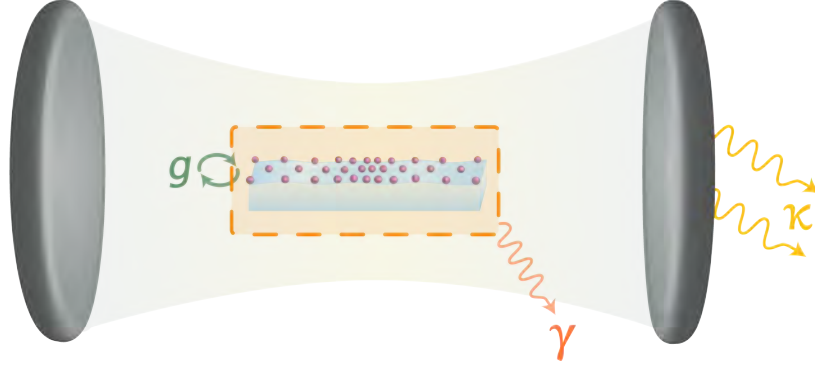


Figure 4.1: Depiction of a charge density wave (i.e. plasmon) in electrons on helium coupled to a microwave cavity field. The plasmon and cavity are coupled with coupling rate  $g$ , and the plasmon and cavity have loss rates  $\gamma$  and  $\kappa$ , respectively.

highly-tunable microwave frequency plasmons in electrons on helium to superconducting coplanar waveguide (CPW) resonators. Fig. 4.1 shows how one might think about this hybrid ensemble system, where the collective excitations of a many-body electron on helium system interact with a microwave cavity field with an interaction strength  $g$ . The microwave cavity has a fundamental frequency  $\omega_r$  and loss rate  $\kappa$ , and similarly, the collective mode of the electrons has a frequency  $\omega_p$  and loss rate  $\gamma$ . This work aims to understand microwave frequency plasmonic excitations in electrons on helium using circuit quantum electrodynamics and explore how the superconducting resonator influences the electron system transport response. These experiments lay the groundwork for developing novel hybrid systems of strongly coupled microwave frequency plasmons and superconducting resonators, opening the door to a new field of cavity optoplasmonics.

# 4.1 Integrating superconducting resonators with microchannel devices

## 4.1.1 Superconducting coplanar waveguide resonators

Superconducting coplanar waveguide resonators (CPWRs) are high quality factor planar resonators, typically operating in the frequency range of several GHz. CPWRs are most notably used in superconducting qubit systems, where the resonators are able to host a small number of photons and coherently couple to the superconducting qubits. Here, we briefly discuss these resonators, which we employ to investigate electron on helium ensemble systems.

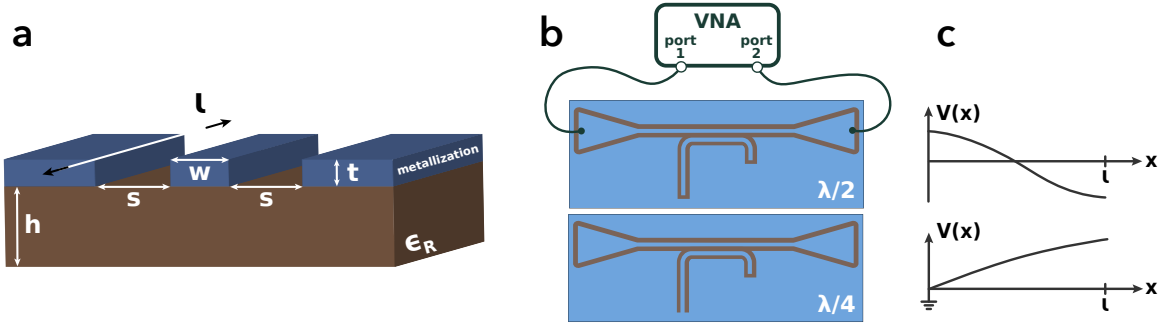


Figure 4.2: (a) Cross section of a superconducting coplanar waveguide resonator. The dielectric substrate (with relative dielectric constant  $\epsilon_R$ ) is colored brown and the metalized areas are colored blue. The width of the center conductor  $w$  and the spacing  $s$  between the center pin and ground plane define the characteristic impedance ( $Z_0$ ) and effective permittivity ( $\epsilon_{\text{eff}}$ ) of the resonator. The total length  $l$  of the center conductor sets the fundamental frequency  $\omega_r/2\pi$  of the resonator. (b) Sketch of a half-wavelength (top) and quarter-wavelength (bottom) CPW resonator capacitively coupled to a feedline. The two ends of the feedline are connected to ports 1 and 2 of a vector network analyzer (VNA) to measure the resonator transmission. (c) Voltage mode structure of the microwave excitations trapped in the respective CPW resonators.

A superconducting coplanar waveguide resonator has a planar geometry, as depicted in the cross section in Fig. 4.2a. The fundamental frequency of the resonator is defined in

fabrication by the resonator wavelength  $\lambda$ ,

$$f_0 = \frac{c}{\lambda\sqrt{\epsilon_{\text{eff}}}}. \quad (4.1)$$

Here, the term  $c/\sqrt{\epsilon_{\text{eff}}}$  is the phase velocity of the propagating electromagnetic wave in the cavity, which depends on the speed of light  $c$  and the effective permittivity  $\epsilon_{\text{eff}}$  of the CPW, where  $\epsilon_{\text{eff}}$  is determined by the geometry of the metallic center pin, its spacing to the ground plane (as depicted in Fig. 4.2a), and the permittivity of the substrate ( $\epsilon_R$ ). Depending on how the resonator is terminated at either end, the wavelength of the fundamental mode will be either a quarter-wavelength  $\lambda = 4l$  or a half-wavelength  $\lambda = 2l$  [185]. As shown in Fig. 4.2b, a  $\lambda/2$  resonator is open on both ends, whereas a  $\lambda/4$  resonator has one end shorted to ground. CPW resonators will have some geometric inductance  $L_r$  and geometric capacitance  $C_r$ , based on the dielectric material and the geometry of the center pin and the ground plane. These geometric parameters, as well as the effective permittivity, can be calculated using finite element modeling (FEM) or with an online coplanar waveguide resonator calculator, such as Ref. [186]. CPWRs are often approximated by a resonant  $LC$ -oscillator circuit, with fundamental frequency  $\omega_r = 1/\sqrt{L_r C_r}$  and characteristic impedance  $Z_0 = \sqrt{L_r/C_r}$  [185]. The resonators shown in Fig. 4.2b are capacitively coupled to a feedline, which allows one to perform resonator spectroscopy with a vector network analyzer (VNA). An  $S_{21}$  measurement of the feedline shows the resonator transmission as a function of frequency.

In the experiments presented in this section, we utilized a  $\lambda/4$  CPWR in the device. The choice for a quarter-wavelength resonator is two-fold: (1) the resonator has an inherently smaller spatial footprint, making it easy to fit both the microchannel devices and CPWRs onto a single chip; and (2) the well-defined voltage anti-node at  $l = L$  (see Fig. 4.2c) provides

a straightforward way to couple the voltage of the microwave signal to the electron system. This also allows us to see how the electron system influences the resonator transmission when the electrostatic environment at that boundary of the resonator is changed.

Additionally, we note that because the effective permittivity plays a role in defining the frequency of the resonator, a CPW resonator can be used as a tool to measure how much helium has condensed in the electron on helium device. This is a consequence of the dielectric liquid helium ( $\epsilon_{\text{He}} = 1.057$ ) increasing the overall effective dielectric  $\epsilon_{\text{eff}}$  of the CPWR, causing the resonator frequency to decrease as helium fills throughout the device. This helium-level sensor functionality will be discussed in further detail in Chapter 5. As discussed in the previous chapter, we can design microchannel geometries that host GHz-frequency charge density oscillations, i.e. plasmons. By strategically integrating a superconducting resonator with this microchannel device architecture, we can investigate how microwave excitations in the resonator affect the electron transport signal and, conversely, how the collective excitations of the electron system affect the resonator response.

## 4.1.2 Composite resonator and microchannel device

### 4.1.2.1 General device architecture

Quarter-wavelength ( $\lambda/4$ ) superconducting coplanar waveguide resonators are integrated with the microchannel device architectures as shown in Fig. 4.3<sup>1</sup>. The device is fabricated onto a 250  $\mu\text{m}$  thick high-resistivity silicon wafer. To create the microchannel structures, a reactive ion etching process was used to etch into the silicon substrate. A combination of electron beam lithography and photolithography was used to pattern microchannel electrodes,

---

<sup>1</sup>This device was designed at Michigan State University and fabricated by Dr. Heejun Byeon in the Pritzker Nanofabrication Facility at the University of Chicago.

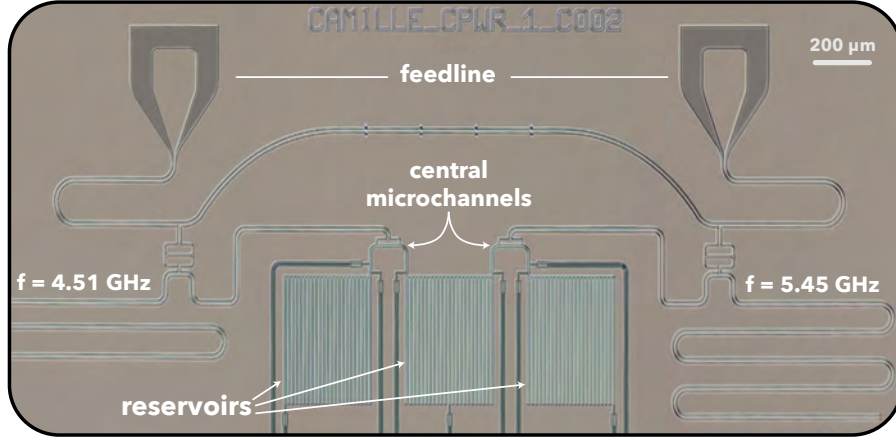


Figure 4.3: Optical microscope image of the superconducting coplanar waveguide resonator integrated microchannel device. The full chip contains two separately operable CPW-microchannel devices. The left side device (LSD) consists of the left most reservoir, left central microchannel, and middle reservoir, with the  $f = 4.51$  GHz resonator capacitively coupled to the left central channel region. The right side device (RSD) consists of the right most reservoir, right central microchannel, and middle reservoir, with the  $f = 5.45$  GHz resonator capacitively coupled to the right central channel region. Both microchannel devices have the same geometry.

CPW resonators, and air bridges (the structures seen across the feedline, which connect the floating ground to the main ground plane of the device). Niobium metal is evaporated onto the device so that the lithographically defined regions are all metalized. The complete fabricated device consists of three reservoirs, two central microchannels, and two CPW resonators situated in close proximity to the central microchannel regions. Both resonators have a center conductor of width  $w_r = 4 \mu\text{m}$ , spacing to the ground plane  $s = 8 \mu\text{m}$ , and niobium metal thickness  $t = 80 \mu\text{m}$ . At the open end of the CPW resonators, both center conductors have a foot of length  $L_f = 80 \mu\text{m}$  that extends parallel along the center of the central microchannel regions. The resonator on the left side was designed to have a frequency of  $\omega_L/2\pi = 4.5$  GHz and a linewidth of  $\kappa_L/2\pi = 1$  MHz. The resonator on the right side was designed to have a frequency of  $\omega_R/2\pi = 5.48$  GHz and a linewidth of  $\kappa_R/2\pi = 15$  MHz. The linewidths of the resonators are set by their coupling geometry to

the feedline, where here we have used a capacitive coupling scheme.

The two central microchannels have the same geometry, with total channel length  $L = 283 \mu\text{m}$  and width  $w = 8 \mu\text{m}$ . The three reservoirs also all have the same geometry, where each reservoir is  $310 \mu\text{m}$  wide and  $400 \mu\text{m}$  tall. The reservoirs are made up of 23 individual  $7 \mu\text{m}$  wide channels and each channel is separated by  $7 \mu\text{m}$ . For the left side central microchannel, either end of the channel lets out into the left and middle reservoir regions and similarly, for the right side central microchannel, either end of the channel lets out into the middle and right reservoir regions. This creates the two separate microchannel devices, where the left side channel, left side reservoir, and middle reservoir regions make up what we will call the left side device (LSD), whereas the right side device (RSD) consists of the middle reservoir, right side central microchannel and right reservoir regions (see Fig. 4.3).

The  $2 \text{ mm} \times 7 \text{ mm}$  chip is wirebonded to a PCB similar to the one shown in Fig. 3.1 and is housed in the same oxygen-free high thermal conductivity (OFHC) copper sample cell used for the previous device described in Chapter 3. The sample cell is mounted onto the mixing chamber plate of a dilution refrigerator and helium is condensed in the cell at  $T \simeq 150 \text{ mK}$  through a stainless steel capillary fill line from a room temperature volume. When helium fills the microchannel structures, it shifts the resonator frequency due to the change in the resonator effective dielectric  $\epsilon_{\text{eff}}$ . This affect will be discussed in more detail in Chapter 5, however we note here that the resonator provides a useful tool to monitor the helium level in the device. Spectroscopy of the resonators is performed via transmission measurements through the feedline using a VNA (connected as described in Fig. 4.2b). For the quarter-wavelength resonators used here, we perform  $S_{21}$  measurements through the feedline, which correspond to measurements of the reflected signal off the resonator. These transmission measurements are continuously monitored as helium fills the channels. We find

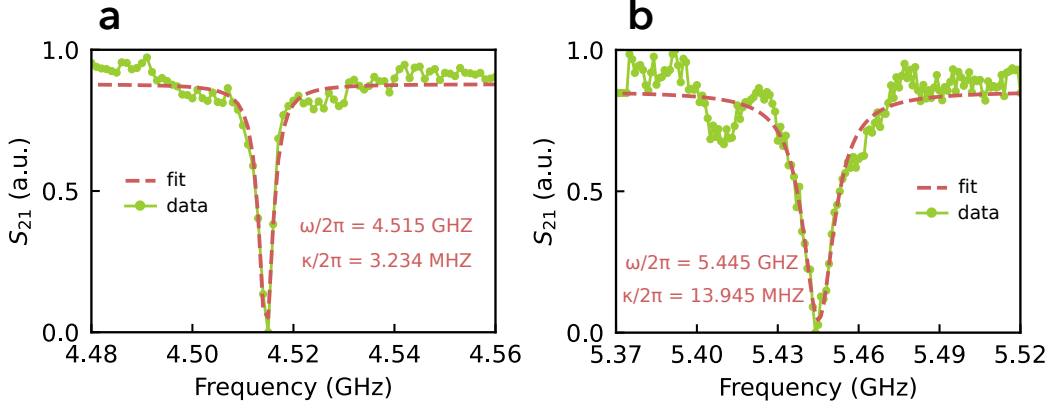


Figure 4.4: Resonator spectroscopy of the two quarter-wavelength CPWRs in the device. The  $S_{21}$  measurements through the feedline correspond to the reflected signal off the resonator. Both measurements were performed with microchannels filled with helium, with no electrons present on the device, and with microwave power  $P = -56$  dBm, at temperature  $T = 60$  mK. (a) Resonator spectroscopy of the left side resonator (see Fig. 4.3). Fit to a Lorentzian distribution gives the resonator frequency  $\omega_L/2\pi = 4.515$  GHz and the resonator linewidth  $\kappa_L/2\pi = 3.234$  MHz. (b) Resonator spectroscopy of the right side resonator (see Fig. 4.3). Fit to a Lorentzian distribution gives the resonator frequency  $\omega_R/2\pi = 5.445$  GHz and the resonator linewidth  $\kappa_R/2\pi = 13.945$  MHz.

that a frequency shift of  $\Delta f \simeq -2$  MHz corresponds to fully filled microchannels. When too much helium is condensed in the device, such that the helium level in the microchannels corresponds to a bulk helium level and the channels are no longer filled via capillary action, we find a frequency shift of  $\Delta f \gtrsim -10$  MHz (see Appendix A.4.1). In Fig. 4.4, we show the resonator transmission for the case of helium filled channels and no electrons yet present on the device. In Fig. 4.4a, we fit the LSD resonator spectroscopy to a Lorentzian distribution and find the resonator frequency  $\omega_L/2\pi = 4.515$  GHz and the resonator linewidth  $\kappa_L/2\pi = 3.234$  MHz. We do the same for the RSD resonator, and find the resonator frequency  $\omega_R/2\pi = 5.445$  GHz and the resonator linewidth  $\kappa_R/2\pi = 13.945$  MHz.

Once helium is condensed in the device, a tungsten filament, located  $\sim 3$  mm above the center of the device, is used to deposit electrons via thermal emission (see Appendix A.2.3 for a description of electron emission). We find that we can successfully deposit electrons onto

the device at  $T \simeq 50 \text{ mK}$ <sup>2</sup>. Fig. 4.5a shows an example of what happens to the resonator spectroscopy when we initially fire electrons into the general region of the LSD. The blue trace shows the typical  $S_{21}$  measurement response in the absence of electrons on the device, with helium filled in the channels. The pink trace shows the resonator response after electrons are fired with the RSD electrodes biased negatively – here, the right reservoir and right channel electrodes are biased together, where  $V_{\text{RSD}} = -0.9 \text{ V}$  – while the LSD electrodes are biased positively – here, the left and middle reservoir electrodes are biased together with  $V_{\text{res,L}} = V_{\text{res,M}} = 1.0 \text{ V}$  and the left channel electrode is biased with  $V_{\text{ch,L}} = 0.2 \text{ V}$ . In this firing procedure, we see that the emitted electrons preferentially land on the general region of the LSD, indicated by the weakened LSD resonator signal due to the presence of electrons in and around the resonator. Due to the negatively biased electrodes corresponding to the RSD, we see the resonator signal remains, indicative of no electrons in that region of the device. In order to actually utilize the microchannel-resonator device, however, we need to remove electrons from the region in and around the resonator to re-establish the resonator signal.

To remove electrons from the resonator and restore its quality factor, we have developed a cleaning protocol. In this procedure, we incrementally increase the microwave power on the feedline while measuring  $S_{21}$  until the resonator signal returns to its original amplitude and linewidth. This cleaning protocol is shown in Fig. 4.5b for the LSD resonator. During these measurements, the RSD electrodes are biased negatively to prevent electrons from entering that region ( $V_{\text{RSD}} = -2.0 \text{ V}$ ) of the device, and bias the middle reservoir positively ( $V_{\text{res, M}} = 1.2 \text{ V}$ ) to have electrons preferentially held in that general region, with  $V_{\text{res, L}} =$

---

<sup>2</sup>Previous microchannel devices showed to be unstable for electron trapping below temperatures of  $\simeq 400 \text{ mK}$

$V_{\text{ch,L}} = 0$  V. During this procedure, no ac transport drive is applied. As the microwave power is increased, we see the resonator return to its original signal amplitude (at  $P \simeq -55$  dBm), indicating that electrons have been removed from the resonator. At the highest power  $P = -46$  dBm shown in Fig. 4.5b, we fit the transmission to a Lorentzian and find the resonator returns to nearly its original frequency and linewidth,  $\omega_L/2\pi = 4.514$  GHz and  $\kappa_L/2\pi = 3.557$  MHz, respectively. With electrons in the appropriate regions of the device, both transport and resonator spectroscopy measurements can be performed. The same firing and cleaning protocol procedures follow for the RSD region. We note, however, that we can also simply move the electrons already in one side of the device to the other by strategically biasing the corresponding regions of electrodes. In the example shown here, where we have fired electrons into the LSD region, we can move them to the RSD by putting negative voltages on the left reservoir and channel electrodes ( $V_{\text{res,L}} = V_{\text{ch,L}} = -0.5$  V), while simultaneously applying positive voltages to the middle reservoir, right reservoir, and right channel electrodes ( $V_{\text{res,M}} = V_{\text{res,R}} = V_{\text{ch,R}} = 0.8$  V). For the remainder of this chapter, all measurements presented are on the RSD.

#### 4.1.2.2 Microchannel-CPW resonator device operation

Standard transport measurements on can be performed as described in Chapter 3. Fig. 4.6a shows a false colored optical microscope image of the RSD in the region surrounding the central microchannel, along with the corresponding transport circuit. The middle reservoir electrode voltage  $V_{\text{res,M}}$  is modulated by an ac drive voltage  $V_{\text{ac}}$  at frequency  $f_{\text{ac}}$ , which induces transport across the device once electrons are introduced into the channel ( $V_{\text{ch}} \gtrsim V_{\text{ch}}^{\text{th}}$ ). In all transport experiments described here, the dc voltage applied to the right reservoir electrode and middle reservoir electrode is the same,  $V_{\text{res,R}} = V_{\text{res,M}}$ . The resulting transport

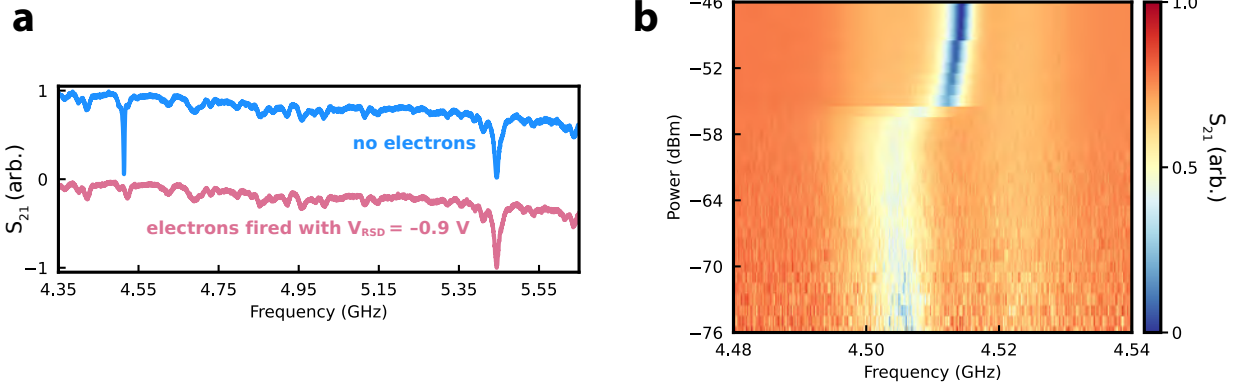


Figure 4.5: (a) Resonator  $S_{21}$  spectroscopy before firing electrons onto the device (dodger blue) and immediately after firing electrons onto the device (pink). Data is offset for visualization. Electrons were fired with all electrodes corresponding to the right side device (RSD) having voltage  $V_{\text{RSD}} = -0.9$  V, and with positive voltages applied to the electrodes corresponding to the LSD ( $V_{\text{res,L}} = V_{\text{res,M}} = 1.0$  V,  $V_{\text{ch,L}} = 0.2$  V). Comparing the two plots shows the precise control over firing electrons onto a particular region of the device (in this case, the LSD). (b)  $S_{21}$  resonator spectroscopy showing the resonator cleaning protocol. By incrementally increasing the power on the VNA (while storing all microchannel device electrons in the middle reservoir region), the electrons that cover the resonator device can be removed. Here, the resonator power removes electrons from the center pin at  $P \simeq -55$  dBm. At the highest power  $P = -46$  dBm, we fit the data to a Lorentzian and find the resonator returns to its original frequency and linewidth,  $\omega_L/2\pi = 4.514$  GHz and  $\kappa_L/2\pi = 3.557$  MHz, respectively.

signal is measured as the voltage induced on the right reservoir, which is amplified by 40 dB and detected using a high frequency (25 kHz – 200 MHz) lock-in amplifier (SR844, see Appendix A). The pinch-off gate electrodes (green, Fig. 4.6a) are biased negatively to prevent electrons from escaping into the electrode bias lines ( $V_{\text{pinch}} = -0.2$  V for all measurements presented here). Additional channel gate electrodes ( $V_{\text{chgt}}$ ) provide an added level of confinement over the electron system in the channel and add another voltage barrier to separate the electrons in the central microchannel from those in the reservoir regions. For all transport measurements discussed in this chapter, they are biased together with the central channel electrode ( $V_{\text{chgt}} = V_{\text{ch}}$ ). The open end of the RSD CPWR is shown in blue in Fig. 4.6a, where the resonator foot spans 80  $\mu\text{m}$  along the central microchannel region to facilitate

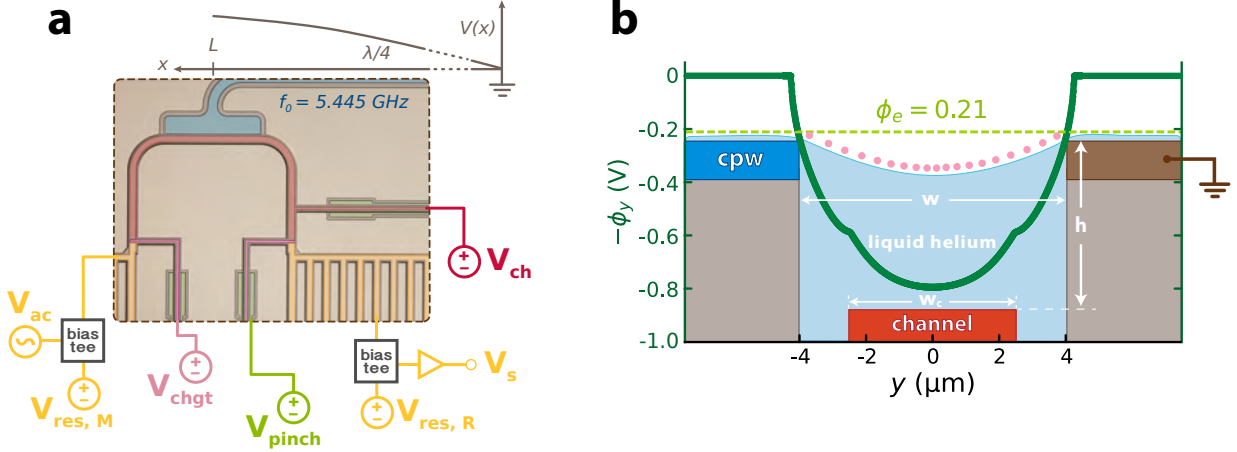


Figure 4.6: (a) False colored optical microscope image of the central microchannel region of the RSD along with a depiction of the transport measurement circuit. The open end of the CPW resonator (blue) is capacitively coupled to the central microchannel region (red). When electrons are present in the device, transport is performed by applying an ac drive  $V_{ac}$  on the middle reservoir and the induced voltage on the right reservoir is amplified by +40 dBm and measured with a lock-in amplifier. (b) Cross-section of the center of the central microchannel. The channel is filled superfluid helium and covered with electrons (pink dots). The potential  $-\phi_y$  across the channel (green) is plotted for  $V_{ch} = 1.0$  V, along with the chemical potential  $\phi_e = 0.21$  V. The central channel has a total width of  $w = 8$   $\mu\text{m}$ , a depth of  $h = 1.17$   $\mu\text{m}$ , and the channel electrode has width  $w_c = 5$   $\mu\text{m}$ .

capacitive coupling to the channel (red) as discussed in Chapter 3, Sec. 3.2.3.

Fig. 4.6b shows a cross section of the device taken at the middle of the central microchannel. The potential profile,  $\phi_y$ , is plotted to indicate the corresponding electrostatic confinement. The depth of the channel is  $h = 1.17$   $\mu\text{m}$  and the width is  $w = 8$   $\mu\text{m}$ . The channel electrode is centered ( $y = 0$ ) at the bottom of the channel and has a width of  $w_c = 5$   $\mu\text{m}$ . A voltage applied to the central channel electrode  $V_{ch}$  will shape the electrostatic potential profile  $\phi(x, y)$  (dark green line). Here,  $V_{ch} = 1.0$  V and the chemical potential  $\phi_e = 0.21$  V (light green dashed line) corresponds to  $V_{ch}^{th} = 0.265$  V and a capacitive coupling constant  $\alpha_{ch} = 0.795$ . To perform transport measurements using the RSD, the LSD electrodes are all biased negatively – similarly, for measurements using the LSD, the RSD electrodes would be biased negatively. We found RSD transport measurements were most stable with the LSD

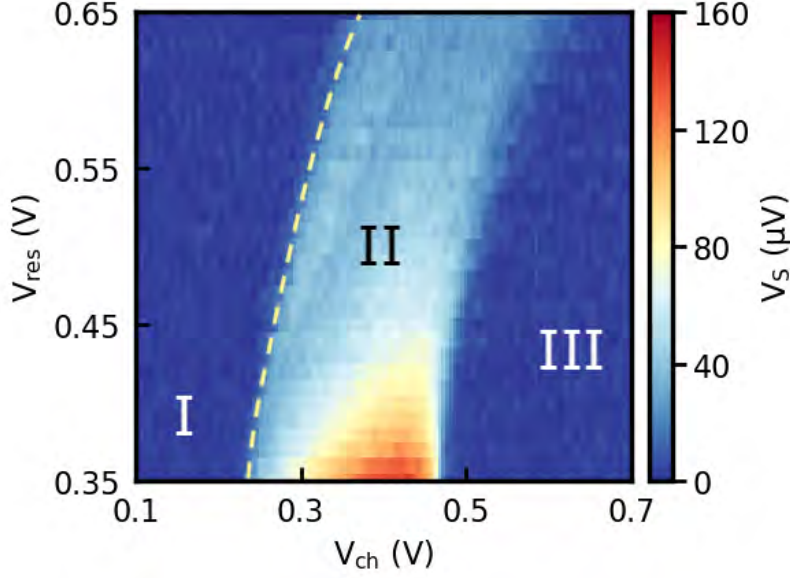


Figure 4.7: Standard transport phase diagram. As  $V_{\text{res}}$  increases, the threshold voltage ( $V_{\text{ch}}^{\text{th}}$ ) increases (yellow dashed line) due to the change in the chemical potential  $\phi_e$ . Three transport regimes are observed: (I) no electrons in the channel, (II) high-conductivity low-density regime in the channel, and (III) low-conductivity Wigner solid. In this measurement, no microwave power was applied to the resonators,  $V_{\text{ac}} = 6$  mV,  $f_{\text{ac}} = 4.013$  MHz,  $V_{\text{pinch}} = -0.2$  V,  $V_{\text{LSD}} = -0.4$  V, and  $T = 55$  mK.

electrodes having voltages  $V_{\text{ch,L}} = V_{\text{chgt,L}} = V_{\text{res,L}} = -0.4$  V.

## 4.2 Standard transport measurements and transport assisted cavity spectroscopy

Typical transport measurements in the absence of a microwave drive on the resonator can be performed to characterize the electron system in the central microchannel region. Fig. 4.7 shows a series of transport measurements at varying  $V_{\text{res}}$  (throughout this chapter, the convention  $V_{\text{res}}$  is used to refer to  $V_{\text{res, M}} = V_{\text{res, R}}$ ). This measurement can be used to find the channel threshold voltage ( $V_{\text{ch}}^{\text{th}}$ ) and the electron density  $n_s$  in the central channel for different values of the reservoir voltages. The three typical transport regimes are observed in

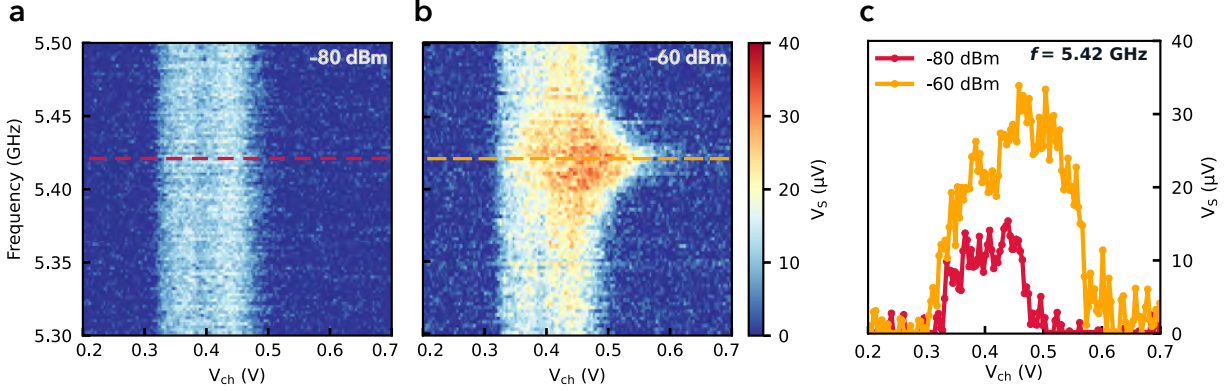


Figure 4.8: (a) Microwave resonator drive frequency dependent transport measurements at low microwave power ( $P = -80$  dBm). Each transport measurement is performed by with the resonator drive signal applied to the feedline, and performing a sweep of the voltage on  $V_{\text{ch}}$ , while measuring the corresponding transport signal on a lock-in amplifier. (b) Similar measurement as in (a), however with higher microwave power,  $P = -60$  dBm. Both measurements were performed at  $T = 55$  mK, with  $V_{\text{ac}} = 4$  mV,  $f_{\text{ac}} = 4.013$  MHz,  $V_{\text{res}} = 0.5$  V,  $V_{\text{pinch}} = -0.2$  V, and  $V_{\text{LSD}} = -0.4$  V. (c) Transport linecuts from (a, red) and (b, orange) corresponding to the frequency  $f = 5.42$  GHz. At high power at the CPW resonator resonance frequency, the transport signal doubles in amplitude, indicative of electron heating.

this measurement: (I) at low channel voltage ( $V_{\text{ch}} < V_{\text{ch}}^{\text{th}}$ ) the channel is empty so no electron transport occurs through the device, (II) at voltages just above the threshold ( $V_{\text{ch}} \gtrsim V_{\text{ch}}^{\text{th}}$ ), the electron system is in a low-density, high-conductivity regime characteristic of an electron liquid or a sliding Wigner solid, and (III) at  $V_{\text{ch}}$  corresponding to a sufficiently high electron density, the electrons crystallize into a low-conductivity Wigner solid. As expected, the channel threshold  $V_{\text{ch}}^{\text{th}}$  increases with increasing  $V_{\text{res}}$  and the electron density  $n_s$  in the channel is constant along the slope of the threshold (yellow dashed line in Fig. 4.7).

To investigate how the CPW resonator drive changes the electron transport signal, we perform a series of transport measurements at varying frequency applied to the resonator. These measurements are shown in Fig. 4.8a. At low microwave power (panel a,  $P = -80$  dBm), the transport signal does not appear to be affected by the microwave drive. In contrast, at high microwave power (panel b,  $P = -60$  dBm), the transport signal amplitude increases in

the frequency range near the microwave resonator fundamental mode. In particular, we see the greatest increase in the electron conductivity at the frequency of the CPW resonator, indicative of microwave photons heating the electron system. In Fig. 4.8c, we compare the two transport signals at low power (red) and high power (orange) for the corresponding horizontal linecuts in panels (a) and (b) at a frequency  $f = 5.42$  GHz. The data show that the increased number of resonator photons doubles the electron transport signal. We also see the channel voltage ( $V_{\text{ch}}$ ) at which the system enters into regime (II) increases, as we saw for the previous device discussed in Chapter 3. This further indicates that the microwave drive is heating the electron system, due to the increased thermal energy of the electrons from the microwave photons necessitating higher electron densities in order to form a Wigner crystal. This follows from the condition that the plasma parameter  $\Gamma \gtrsim 130 \propto \sqrt{n_s}/T$  (from Chapter 2, Sec. 2.1.3) in order for crystallization to occur.

Additionally, we show the dependence of the microwave frequency applied to the feedline at low versus high power for fixed electron density (corresponding to vertical linecuts in the data at fixed  $V_{\text{ch}}$  in Fig. 4.9a-b). In Fig. 4.9c, the transport signal just above the threshold ( $V_{\text{ch}}^{\text{th}} = 0.32$  V) is plotted for both low and high power. At low electron density ( $V_{\text{ch}} = 0.325$  V), for both low and high power measurements, no increase in electron conductivity is observed as a result of the applied microwave power. In Fig. 4.9d, we compare the microwave power effects at a constant high electron density in the channel ( $V_{\text{ch}} = 0.545$  V). At low power (red), the transport signal indicates that the electron system remains in the low conductivity Wigner crystal state for all microwave frequencies. In contrast, at high microwave power (orange), the electron system appears to heat in the vicinity of the resonance frequency of the CPW resonator. We note, this may also be interpreted as the microwaves promoting a sliding Wigner crystal, however further transport data as a function of ac drive voltage, with and

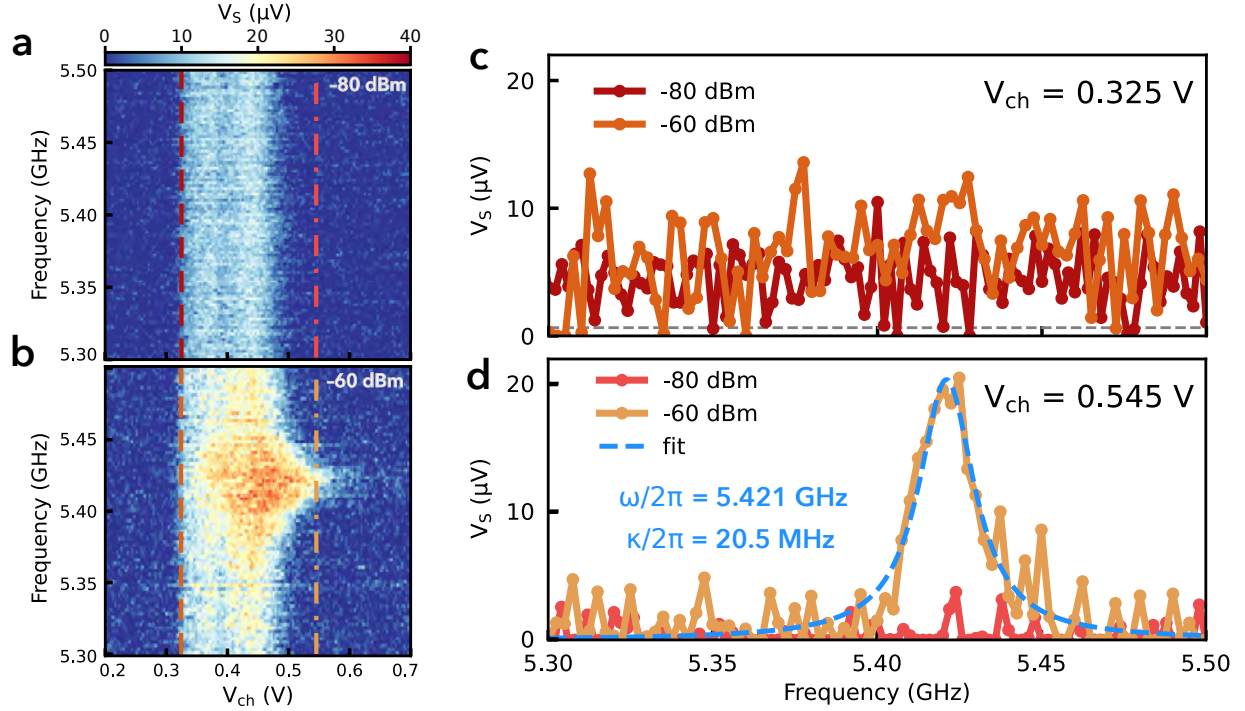


Figure 4.9: (a),(b) Same data shown in Fig. 4.8. Vertical dashed lines in (a) and (b) correspond to the linecuts presented in panels (c) and (d). (c) Transport signal as a function of the resonator drive frequency at  $V_{\text{ch}} = 0.325$  V from (a, red) and (b, orange) showing the frequency dependence at constant low electron density in the channel. At both low and high microwave power, the electron system is insensitive to the microwave signal for all frequencies. Grey dashed line indicates the lock-in signal in the no-electron region. (d) Transport signal as a function of resonator drive frequency at  $V_{\text{ch}} = 0.545$  V from (a, red) and (b, orange) showing the frequency dependence at constant high electron density in the channel. At low microwave power, for all frequencies, the electron system is in the low conductivity Wigner solid state. At high microwave power, the electron system conductivity jumps at the frequency of the CPW resonance frequency, indicative of a non-equilibrium heating of the electron system. The transport signal is fit to a Lorentzian (blue dashed line) and the resonance frequency of the CPW resonator in the presence of electrons is resolved ( $\omega/2\pi = 5.421$  GHz) as well as a broadened resonator linewidth  $\kappa/2\pi = 20.5$  MHz.

without a microwave drive on the resonator, would be needed in order to say definitively. By fitting the high power data in Fig. 4.9d to a Lorentzian distribution, we find the data peak at frequency,  $\omega/2\pi = 5.421$  GHz and have a linewidth  $\kappa/2\pi = 20.5$  MHz. As we will see in the next section (Sec. 4.3.1), this frequency and linewidth are in agreement with the frequency and linewidth of the resonator when electrons are present in the central microchannel. This measurement is consistent with microwave induced non-equilibrium heating of the electron system.

## 4.3 Plasmon-resonator coupling

### 4.3.1 Spectroscopy of the coupled resonator-plasmon system

To investigate the coupled plasmon-resonator system, we perform  $S_{21}$  measurements of the CPW resonator at varying channel electrode voltage ( $V_{\text{ch}}$ ). Tuning  $V_{\text{ch}}$  corresponds to tuning the density, where  $\omega_p \propto \sqrt{n_s(V_{\text{ch}})}$ , and we can anticipate tuning the electron density such that a plasmon mode becomes resonant with the CPW resonator,  $\omega_r = \omega_p$ . Data from this type of measurement is shown in Fig. 4.10a. Here, we perform spectroscopy measurements at each increment in  $V_{\text{ch}}$  to monitor the resonator response as electrons populate the central channel. This measurement is performed at fixed reservoir voltage,  $V_{\text{res}} = 0.5$  V, and with no ac transport drive.

At  $V_{\text{ch}} = 0.374$  V, the data show an avoided crossing like feature. To confirm that this avoided crossing feature is the result of electrons within the central microchannel, the same measurement is performed for varying reservoir voltages  $V_{\text{res}}$  (see Appendix [] for all reservoir dependent spectroscopy data). As the reservoir voltage  $V_{\text{res}}$  changes, the threshold voltage  $V_{\text{ch}}$  changes, as shown in the phase diagram in Fig. 4.7. Because the electron density in the

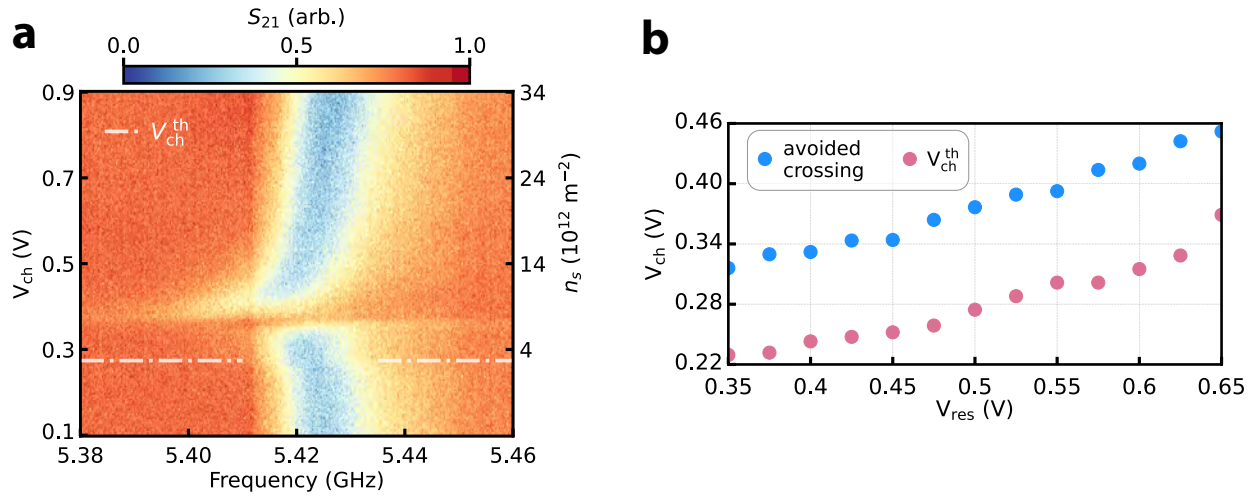


Figure 4.10: (a)  $S_{21}$  resonator spectroscopy measurements as a function of the central microchannel voltage  $V_{\text{ch}}$ . Electrons enter into the central channel at the threshold voltage  $V_{\text{ch}}^{\text{th}} = 0.274$  V (white dash dotted line) and with increasing channel voltage, the electron density  $n_s$  in the channel increases. At  $V_{\text{ch}} \simeq 0.374$  V, the data show an avoided crossing, indicative of the channel reaching an electron density that corresponds to a plasmon mode resonant with the CPW resonator  $\omega_p \simeq \omega_r$ , such that the plasmon and resonator hybridize. Measurements here were taken at  $V_{\text{res}} = 0.5$  V and  $P = -80$  dBm. (b) Extracted avoided crossing points (blue) taken from similar spectroscopy measurements as (a) at varying  $V_{\text{res}}$  plotted with the channel threshold voltages  $V_{\text{ch}}^{\text{th}}$  at each corresponding  $V_{\text{res}}$  (pink). Threshold data is taken from Fig. 4.7.

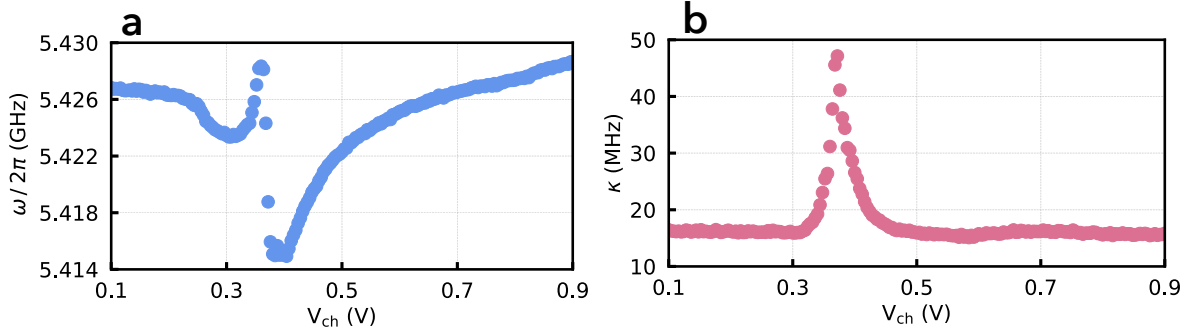


Figure 4.11: (a) Extracted frequencies  $\omega/2\pi$  of the resonator as a function of  $V_{ch}$  from fits to a Lorentzian distribution for the data shown in Fig. 4.10a. In the region of the avoided crossing, the frequency has the largest shift per  $V_{ch}$ . (b) Extracted linewidths  $\kappa/2\pi$  of the resonator as a function of  $V_{ch}$  from the fit performed in (a). At the avoided crossing, the linewidth is the largest

channel is proportional to the threshold,  $n_s \propto (V_{ch} - V_{ch}^{th})$ , the voltage  $V_{ch}$  at which the avoided crossing occurs should shift, as the reservoir voltage is changed, to meet the resonant plasmon density condition. The transport threshold voltage  $V_{ch}^{th}$  for each corresponding  $V_{res}$  is extracted from Fig. 4.7 and plotted in Fig. 4.10b (pink dots), along with the extracted avoided crossing centers in  $V_{ch}$  for each spectroscopy measurement.

## 4.3.2 Plasmon-resonator interaction: two classical coupled oscillators

### 4.3.2.1 Electric field coupling and boundary conditions

To understand the origin of the avoided crossing feature seen in the data in Fig. 4.10a and how the electron system and resonator might couple, we perform finite element modeling (FEM) calculations of the device in the general region of the central microchannel. Because the open end (i.e. voltage anti-node) of the resonator is placed adjacent to the channel electrode, when electrons populate the channel, they experience the electric field produced by the resonator. The contribution to the electric field from the resonator is shown in

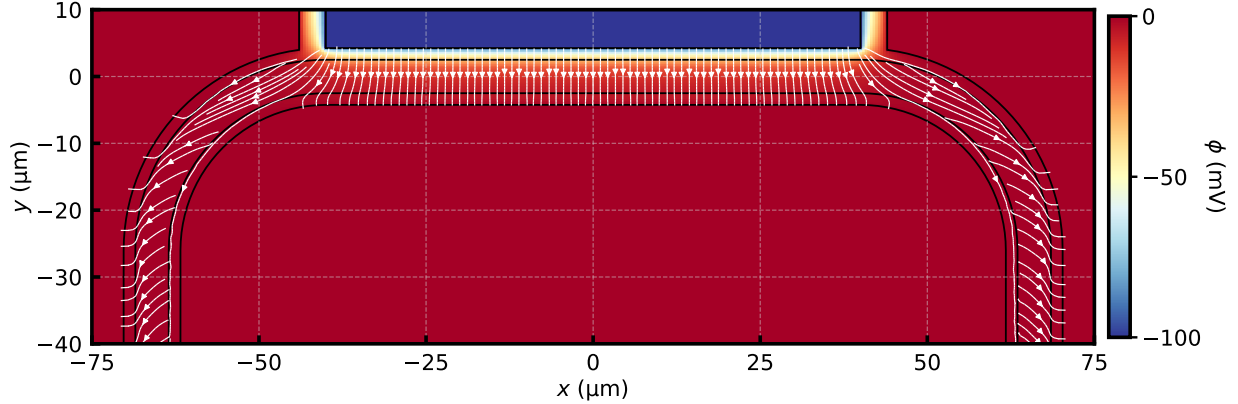


Figure 4.12: Microwave potential in the central microchannel region near the open-end of the resonator center pin with corresponding electric field lines (white arrows) calculated from FEM simulations.

Fig. 4.12, where the white arrows indicate the electric field lines calculated from FEM. On either edge of the resonator center pin ( $x = \pm 40 \mu\text{m}$ ), the electric field distribution in the channel has a non-zero  $x$ -component. This enforces odd-mode longitudinal plasmons along the length of the channel to be the most strongly coupled, as discussed for the previous device in Chapter 3. In Fig. 4.13a, we plot the half-wavelength electron displacement profile  $\Delta x$  for the  $n = 1, 3,$  and  $5$  modes and compare them to the  $x$ -component of the electric field. Fig. 4.13b shows the  $x$ -component of the electric field  $E_x$  from the resonator for each point along the center of the channel, where each point (pink) represents a point along the pink dotted line in Fig. 4.14a. Here, we see for a half-wavelength odd mode, the maximum displacement amplitude aligns with the maximum electric field amplitude in the  $x$ -direction at  $x \simeq \pm 40 \mu\text{m}$ .

In Fig.[density fig], we show the static density profile (i.e. in the absence of a microwave drive on the resonator) in the device for the applied voltages used for the measurement in Fig. 4.10a, for the channel electrode voltage at the center of the avoided crossing ( $V_{\text{ch}} \simeq 0.374 \text{ V}$ ). In particular, we see there exists an intrinsic static density inhomogeneity in the

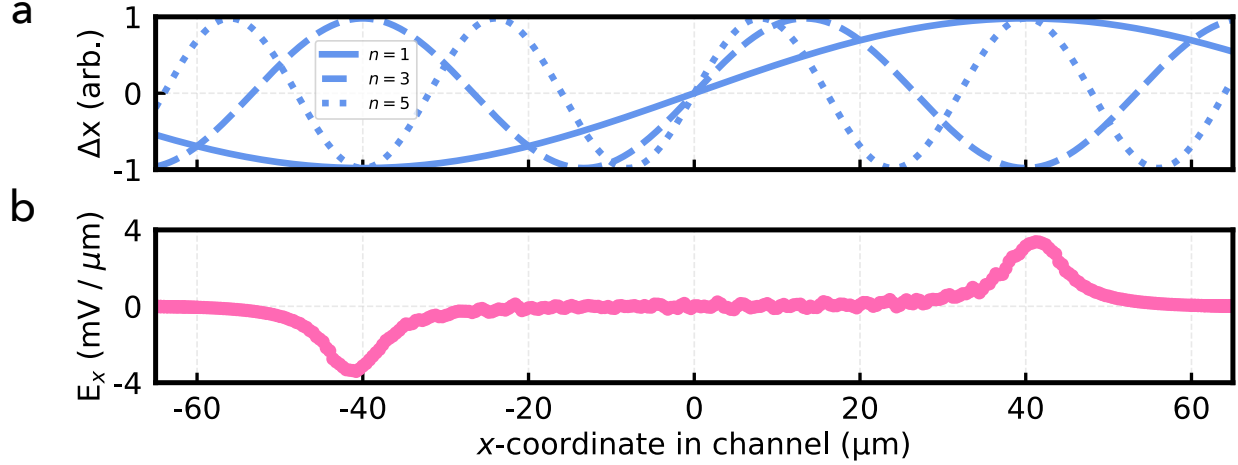


Figure 4.13: (a) Plot showing how the  $n = 1, 3,$  and  $5$  plasmon modes will manifest in terms of the change in electron displacement  $\Delta x$  along the channel. (b)  $x$ -component of the electric field produced by the resonator center conductor along the center of the central microchannel. Each pink dot corresponds to a position in the channel from the pink dotted line in Fig. 4.14a.

channel near the edges of the resonator center conductor, which could impose the boundary condition at  $x = \pm 40$   $\mu\text{m}$  for a plasmon mode wavelength of  $\lambda/2 = 80$   $\mu\text{m}$ .

If we assume the electric field and density inhomogeneity produced by the resonator at the edges of the center conductor set the plasmon mode coupling and wavelength, respectively, we can estimate the plasmon frequencies for this geometry. The plasmon dispersion relation, from the 2D screened plasmon dispersion relation we defined in Chapter 3 (Eq. 3.1), is

$$\omega_p/2\pi = \left[ \frac{n_s e^2}{2m_e \epsilon_0} \sqrt{q_x^2 F(q_x)} \right]^{1/2}. \quad (4.2)$$

Here, the wavevector  $q_x = n\pi/L$  corresponds to the direction along the length of the channel for the plasmon wavelength  $\lambda/2 = L$  and corresponding mode  $n$ . The screening parameter,  $F(q_x) = \frac{1}{2}[\tanh(l q_x) + \tanh(d q_x)]$ , depends on the screening lengths from: (1) the electron system to the center conductor (at  $y = 4$   $\mu\text{m}$ ) and ground plane (at  $y = -4$   $\mu\text{m}$ ),  $l = w - w_e$ , for the channel width  $w = 8$   $\mu\text{m}$  and the 2D electron sheet effective width  $w_e$ ;

and (2) the electron system to the channel electrode beneath  $d = 1.17 \text{ }\mu\text{m}$ . The avoided crossing feature in Fig. 4.10a occurs at  $V_{\text{ch}} \simeq 0.374 \text{ V}$ , which corresponds to a density of  $n_s \simeq 7.81 \times 10^{12} \text{ m}^{-2}$  and an effective width  $w_e \simeq 3.2 \text{ }\mu\text{m}$ . Plugging these numbers into Eq. 4.2, we find that the  $n = 1, 3,$  and  $5$  modes correspond to the plasmon frequencies  $\omega_p/2\pi = 1.9 \text{ GHz}, 4.3 \text{ GHz},$  and  $6.2 \text{ GHz}$ , respectively. Although these plasmon frequencies are not consistent with the  $5.42 \text{ GHz}$  frequency we observe in the avoided crossing, we can model the system as two classical coupled oscillators to determine where the discrepancy might be coming from. This will also allow us to model our data to estimate the effective coupling strength  $g_{\text{eff}}$  and the plasmon mode loss rate  $\gamma$ .

#### 4.3.2.2 Coupled system equations of motion and eigenfrequencies

To model the resonator response, we approximate the plasmon-resonator system as two classical coupled oscillators, following the illustration of the coupled system shown in Fig. 4.15a. First, we consider the CPW resonator as its  $LC$ -circuit equivalent. This allows us to write the Lagrangian  $\mathcal{L}$  of the circuit in terms of the charge variable  $q(t)$  including a dissipation term  $\mathcal{F}$ , corresponding to the resonator loss rate  $\kappa$ , using

$$\frac{d}{dt} \left( \frac{\partial \mathcal{L}}{\partial \dot{q}} \right) - \frac{\partial \mathcal{L}}{\partial q} + \frac{\partial \mathcal{F}}{\partial \dot{q}} = 0. \quad (4.3)$$

The Lagrangian,  $\mathcal{L} = \mathcal{T} - U$ , for the damped  $LC$ -circuit has kinetic energy  $\mathcal{T}$  due to the geometric inductance  $L_r$  of the resonator  $T = \frac{1}{2}L_r\dot{q}^2$ , and potential energy  $U$  from the geometric capacitance  $C_r$  of the resonator,  $U = q^2/C_r$ . The dissipative term is given by  $\mathcal{F} = \frac{1}{2}\gamma\dot{q}^2$  [187]. From this, we can write the equation of motion for the resonator as

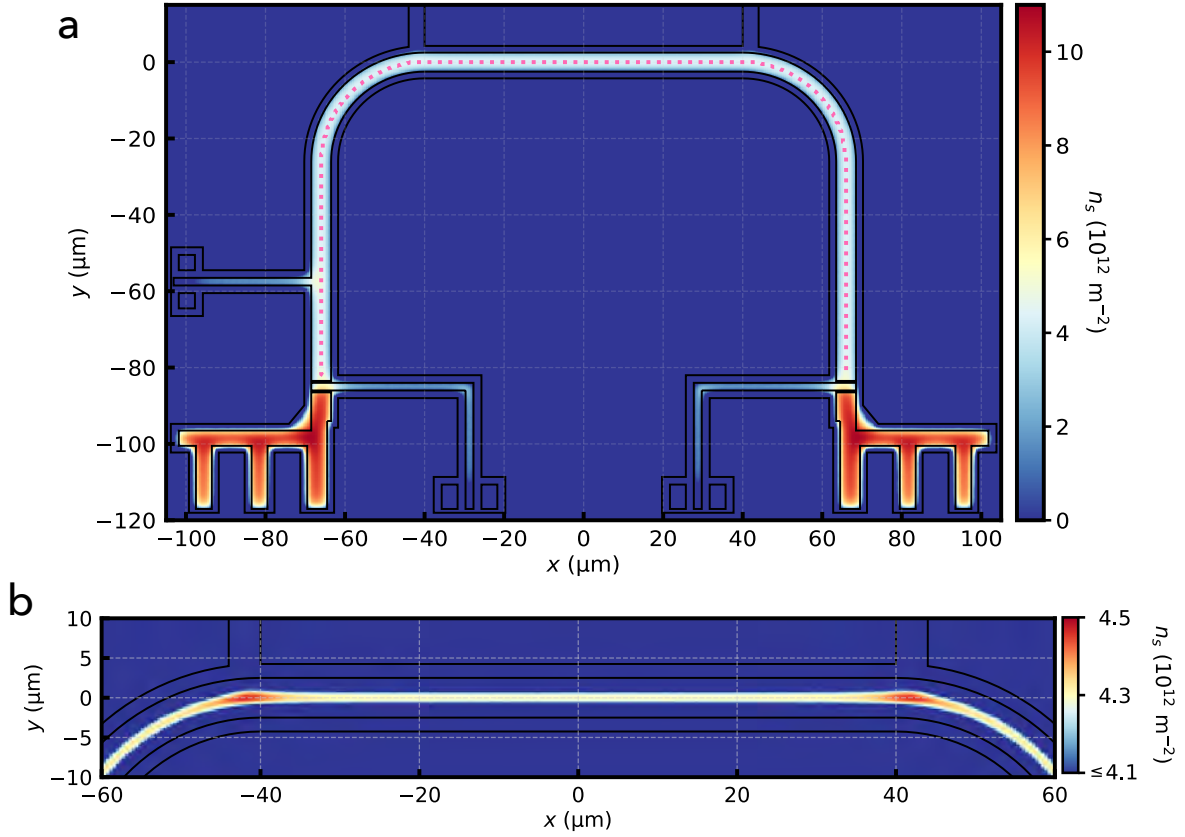


Figure 4.14: (a) Electron density distribution for the corresponding voltages used for the measurement in Fig. 4.10a, where  $V_{\text{res}} = 0.5 \text{ V}$ ,  $V_{\text{pinch}} = -0.2 \text{ V}$ , and  $V_{\text{ch}} = 0.374 \text{ V}$ . Pink dotted line along the center of the central channel corresponds to the location of the calculated points in Fig. 4.13a-b. (b) Electron density distribution from (a), zoomed into the region near the resonator center conductor. Colormap shown for  $4.1 \leq n_s < 4.5$  ( $\times 10^{12} \text{ m}^{-2}$ ) to highlight the intrinsic static density inhomogeneity in the region of the channel near the resonator.

$$L_r \frac{d^2 q(t)}{dt^2} + 2L_r \kappa \frac{dq(t)}{dt} + \frac{1}{C_r} q(t) = g x(t). \quad (4.4)$$

On the right hand side, the parameter  $g x(t)$  corresponds to the coupling rate  $g$  of the charge density wave oscillator, with generalized coordinate  $x(t)$  corresponding to the electron positions. The equation of motion for the charge density wave oscillator can be written in terms of the position of the electrons  $x(t)$ , as

$$\tilde{m} \frac{d^2 x(t)}{dt^2} + 2\tilde{m}\gamma \frac{dx(t)}{dt} + \tilde{m}\omega_p^2 x(t) = g q(t), \quad (4.5)$$

where we have the effective mass of the charge density wave  $\tilde{m}$ , plasmon damping rate  $\gamma$ , and plasmon frequency  $\omega_p$  [187]. These two coupled equations describe how the amplitude of the resonator field will apply a force on the charges in the sheet proportional to  $q(t)$  and similarly, how the charge density oscillations will influence the local resonator field. At frequency  $\omega$ , the two systems can hybridize. We can find the eigenfrequencies of the coupled plasmon-resonator system by making the ansatzes,

$$q(t) = q_0 e^{-i\omega t}, \quad x(t) = x_0 e^{-i\omega t} \quad (4.6)$$

for the resonator and the plasmon excitations, respectively. Plugging these into Eqs. 4.4 and 4.5, gives the coupled equations in the form:

$$q_0(-\omega^2 - 2i\kappa\omega + \omega_r^2) = \frac{g}{L_r} x_0 \quad (4.7)$$

$$x_0(-\omega^2 - 2i\gamma\omega + \omega_p^2) = \frac{g}{\tilde{m}} q_0, \quad (4.8)$$

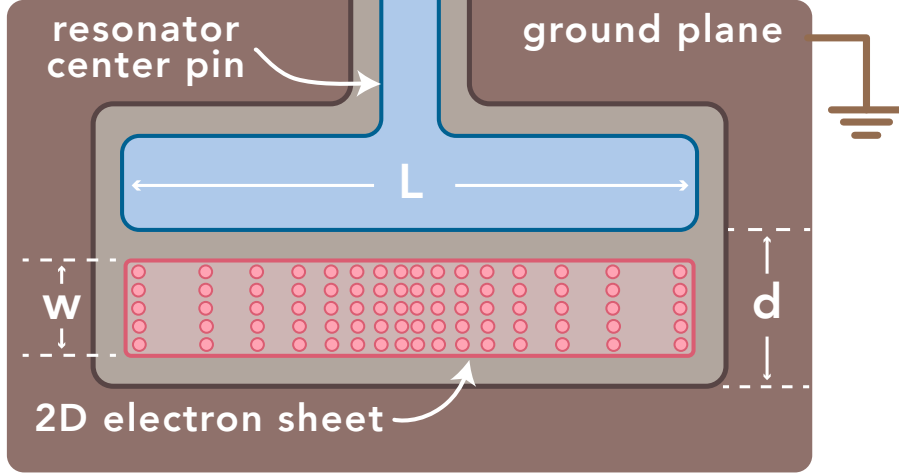


Figure 4.15: (a) Simplified illustration of the 2D plasmon in the region between the end of the resonator center pin and the ground plane. The electron sheet will have some width  $w$  and the plasmon mode length will be approximately the length of the resonator center pin foot  $L$ . The distance between the open end of the resonator and the ground plane is  $d$ .

where in Eq. 4.7, we have divided by  $L_r$  and defined the fundamental frequency of the resonator  $\omega_r = 1/\sqrt{L_r C_r}$ . The two equations can be set up in matrix form,

$$\begin{pmatrix} (\omega_r^2 - \omega^2 - 2i\kappa\omega) & -\frac{g}{L_r} \\ -\frac{g}{\tilde{m}} & (\omega_p^2 - \omega^2 - 2i\gamma\omega) \end{pmatrix} \begin{pmatrix} q_0 \\ x_0 \end{pmatrix} = \begin{pmatrix} 0 \\ 0 \end{pmatrix} \quad (4.9)$$

and the eigenfrequencies can be found by diagonalizing the  $2 \times 2$  matrix. In the undamped limit,  $\kappa = \gamma = 0$ , the eigenfrequencies of the coupled system are

$$\omega_{\pm}^2 = \frac{\omega_r^2 + \omega_p^2}{2} \pm \frac{1}{2} \sqrt{(\omega_r^2 - \omega_p^2)^2 + \frac{4g^2}{L_r \tilde{m}}}. \quad (4.10)$$

On resonance ( $\omega_r = \omega_p$ ), we get the mode splitting  $2g/\sqrt{L_r \tilde{m}}$ . In order to solve for the complex eigenfrequencies in the damped case (i.e. non-zero  $\kappa$  and  $\gamma$ ), we make the simplifying assumption that the damping is weak compared to the frequencies,  $\kappa, \gamma \ll \omega_c, \omega_p$ , and that we are in a near resonance regime such that  $\omega \approx \omega_c \approx \omega_p$ . Then, we find the complex

eigenfrequencies  $\Omega_{\pm}$  by solving  $\det(\mathbf{M} - \Omega\mathbf{I}) = 0$ , where

$$\det \begin{pmatrix} (\omega_r - i\kappa - \Omega) & -\frac{g}{L_r} \\ -\frac{g}{\tilde{m}} & (\omega_p - i\gamma - \Omega) \end{pmatrix} = 0 \quad (4.11)$$

$$(\omega_r - i\kappa - \Omega)(\omega_p - i\gamma - \Omega) - \frac{g^2}{L_r \tilde{m}} = 0, \quad (4.12)$$

and

$$\Omega_{\pm} = \frac{(\omega_r - i\kappa) + (\omega_p - i\gamma)}{2} \pm \sqrt{\frac{1}{4} \left( (\omega_r - i\kappa) - (\omega_p - i\gamma) \right)^2 + \frac{g^2}{L_r \tilde{m}}}. \quad (4.13)$$

The first term is the average of the two uncoupled complex frequencies, where the real part  $\frac{1}{2}(\omega_r + \omega_p)$  is the frequency at which the hybridized system splitting is centered, and the imaginary part gives the average loss, or the hybrid mode linewidth,  $\frac{1}{2}(\kappa + \gamma)$  in the limit of  $\kappa \approx \gamma$ .

### 4.3.3 Analysis of the effective plasmon-resonator coupling

Although we cannot fully quantify the coupling parameter  $g$  due to the complicated way the electric field from the resonator couples to the electron system, we can still model the data from Fig. 4.10a with an effective coupling parameter  $g_{\text{eff}} = \frac{g}{\sqrt{L_r \tilde{m}}}$ . In Fig. 4.16a, we plot the data from Fig. 4.10a beginning at  $V_{\text{ch}}^{\text{th}} = 0.274$  V to simplify the analysis by only considering the case with electrons in the channel. The upper and lower branches are plotted (gray dotted lines) for the undamped limit  $\kappa = \gamma = 0$  and with the effective coupling

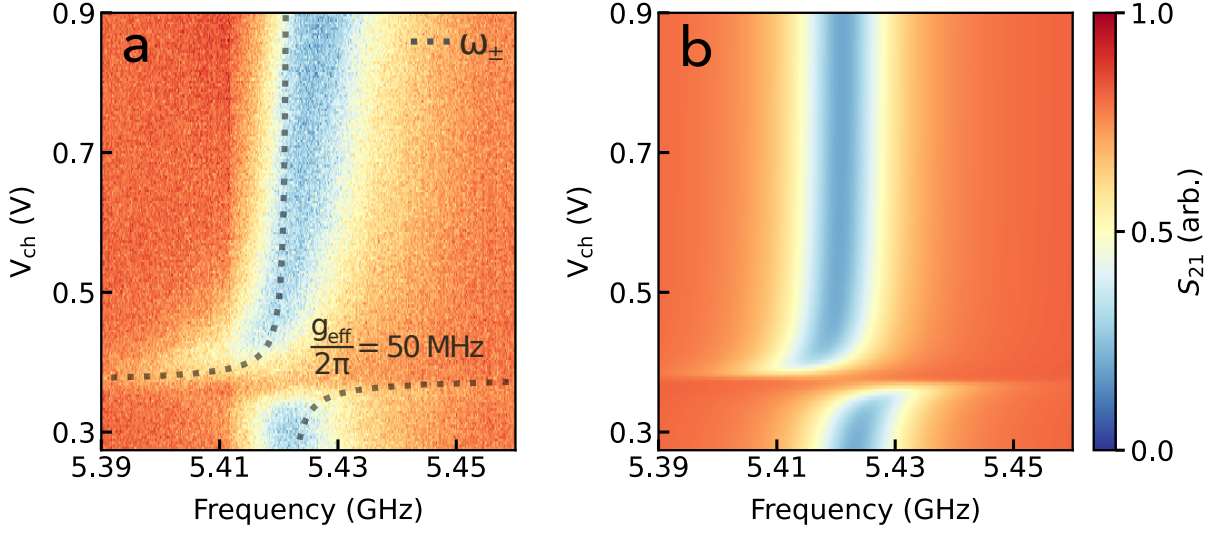


Figure 4.16: (a) Same data from Fig. 4.10a with calculated avoided crossing from Eq. 4.14. Here we find an effective coupling rate  $g_{\text{eff}}/2\pi = 50$  MHz. (b) Calculated  $S_{21}$  response using Eq. 4.16 with  $\kappa/2\pi = 14.4$  MHz,  $\gamma/2\pi = 150$  MHz,  $g_{\text{eff}}/2\pi = 50$  MHz, and a linear plasmon frequency dependence  $\omega_p \simeq \beta V_{\text{ch}}$  with  $\beta/2\pi = 14.5$  GHz/V.

parameter  $g_{\text{eff}}$ , where

$$\omega_{\pm} = \frac{\omega_c + \omega_p}{2} \pm \sqrt{\frac{(\omega_c - \omega_p)^2}{4} + g_{\text{eff}}^2}. \quad (4.14)$$

In this approximation, we neglect how the electron system shifts the resonator frequency, as this will not affect the strength of the effective coupling in this simplified model. In Fig. 4.16b, we calculate the eigenmodes from Eq. 4.13, using the  $g_{\text{eff}}$  parameter, and assume a Lorentzian response for the upper and lower branches  $\mathcal{R}_{\pm}$ ,

$$\mathcal{R}_{\pm} \propto \frac{1}{(\omega - \text{Re}[\Omega_{\pm}])^2 + \text{Im}[\Omega_{\pm}]^2} \quad (4.15)$$

$$\Rightarrow S_{21} = 1 - (\mathcal{R}_+ + \mathcal{R}_-). \quad (4.16)$$

In modeling the avoided crossing data in this approximation, we use the known resonator loss rate  $\kappa/2\pi = 14.4$  MHz and find the effective coupling rate is  $g_{\text{eff}}/2\pi = 50$  MHz and the plasmon loss rate is  $\gamma/2\pi = 150$  MHz. In the near-resonance approximation, we assume the

plasmon mode  $V_{\text{ch}}$ -dependence is roughly linear, with  $\omega_p \simeq \beta V_{\text{ch}}$ . In Fig. 4.16a-b, we find  $\omega_p$  scales with  $V_{\text{ch}}$  as  $\beta/2\pi = 14.5 \text{ GHz/V}$ .

We note that we do not use the plasmon dispersion (Eq. 4.2) to model  $\omega_p$  in this analysis. When we discussed the the plasmon mode we anticipated for the coupled system in Sec. 4.3.2.1, we found that the  $n = 3$  and  $n = 5$  modes would correspond to plasmon frequencies of  $\omega_p/2\pi \simeq 4.3 \text{ GHz}$  and  $\omega_p/2\pi \simeq 6.2 \text{ GHz}$ , respectively. In contrast, for the classical coupled oscillator modeling, we consider the plasmon frequency  $\omega_p$  as scaling linearly with  $V_{\text{ch}}$  as  $\beta/2\pi = 14.5 \text{ GHz/V}$ . We find that the theoretical calculation for the complex eigenfrequencies  $\Omega_{\pm}$  plotted in Fig. 4.16b agrees well with the data, and this parameter gives the plasmon frequency near the avoided crossing  $\omega_p/2\pi \simeq 5.42 \text{ GHz}$ . If we assume the screening parameter  $F(q_x)$  and the FEM simulations for the density are accurate, the primary unknown parameter in our modeling is the plasmon mode wavelength. This is reasonable given the non-trivial  $x$ -component of the electric field distribution, shown in Fig. 4.12. To extract the plasmon frequency we use in the resonant interaction modeling from Fig. 4.16b, the plasmon wavelength would have to correspond to  $\lambda/2 \simeq 58 \text{ }\mu\text{m}$ . In Fig. 4.17, we plot the  $n = 3$ , 2D plasmon dispersion relation  $\omega_p$  for a  $\lambda/2 \simeq 58 \text{ }\mu\text{m}$  wavelength from Eq. 4.2, with the  $\omega_p \simeq \beta V_{\text{ch}}$  plasmon frequency dependence used to model the avoided crossing data for  $\beta/2\pi = 14.5 \text{ GHz/V}$ . From this, we find good agreement with the avoided crossing modeling for the CPW resonator coupling to a  $n = 3$  longitudinal plasmon mode along the length of the channel for a plasmon wavelength of  $\lambda/2 \simeq 58 \text{ }\mu\text{m}$ .

It is also noted that we neglected the effect of electrons in the channel on the resonator frequency that we observe in the data in Fig. 4.10a from  $V_{\text{ch}} = 0.4 - 0.9 \text{ V}$ . The resonator shifting *up* in frequency as a function of electron density is not something we would have anticipated and why this happens remains a mystery. Intuitively, we would expect as the

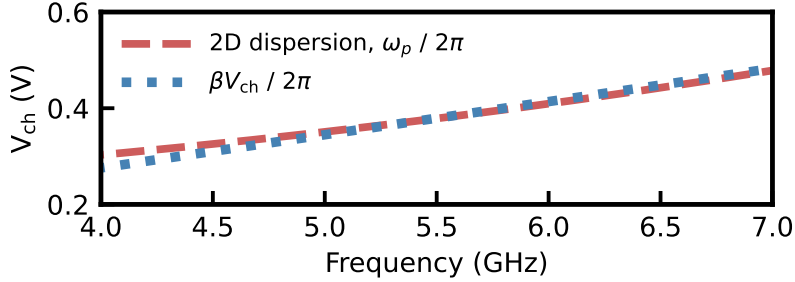


Figure 4.17: Plot showing the  $V_{ch}$  dependence on the plasmon frequency for the 2D screened plasmon dispersion relation introduced in Chapter 3 (Eq. 4.2)  $\omega_p/2\pi$  (pink dashed line) and plasmon frequency used to model the resonant interaction in Fig. 4.16,  $\beta V_{ch}/2\pi$  (blue dotted line,  $\beta/2\pi = 14.5$  GHz/V).

electron density increases (i.e. as the effective width of the electron system increases), the local capacitance between the open end of the resonator and the ground plane would increase and thus the total geometric capacitance  $C_r$  would increase, resulting in a decrease in resonator frequency (see Fig. 4.15). This phenomenon remains an open question. For future iterations of this device, one way to ensure knowing how the plasmon wavelength boundary conditions are set would be to design the channel gate electrodes to be positioned in the channel at  $x = \pm 40$   $\mu\text{m}$ . Experiments of the same kind performed here with that kind of geometry could verify how the ends of the channel in which the plasmon propagates are set, by cutting off the rest of the channel and reservoir regions right at the boundary of where the plasmon mode is likely coupling to the resonator.

#### 4.3.4 Summary of results

Here, we have designed, fabricated, and tested a microchannel device architecture with superconducting coplanar waveguide resonators coupled to the central microchannel region. We found that simultaneous transport measurements in the presence of a microwave drive on the resonator reveal the resonator fundamental mode frequency  $\omega_r/2\pi$  and linewidth  $\kappa/2\pi$

and we observed signatures of non-equilibrium heating effects of the electron system similar to those observed and discussed in Chapter 3. By tuning the density in the central microchannel and measuring the resonator transmission, the resonator and electron system hybridize and the data show an avoided crossing-like feature. We find this avoided crossing feature follows the channel threshold voltage, indicating that the hybrid system is occurring due to electrons in the central microchannel. From FEM calculations, the electric field distribution created by the resonator in the channel region indicates that odd plasmon modes are the most likely modes to couple to the resonator field. By analyzing the coupled electron-resonator system as two classical coupled oscillators, we find that the plasmon and resonator couple with the effective coupling rate  $g = 50$  MHz and that the plasmon loss rate is  $\gamma/2\pi \simeq 150$  MHz. From this analysis, we also find that the boundaries within which the plasmon is confined is ill-defined. However, by setting the plasmon wavelength to be defined at the onset of a non-zero electric field  $x$ -component ( $x \simeq \pm 30 \mu\text{m}$ ), the  $\lambda/2 \simeq 58 \mu\text{m}$   $n = 3$  mode corresponds to the plasmon frequency  $\omega_p/2\pi = 5.42$  GHz.

# Chapter 5

## Using superconducting resonators to investigate helium surface fluctuations

Experiments relying on the low mechanical noise at low temperatures have recently gained more attention. This is largely driven by the increasing popularity of cryogen-free “dry” systems instead of the “wet” dilution refrigerators that rely on cryogenic liquid helium. These wet systems become expensive due to the large helium consumption and require interruptions to experiments for refilling the dewar with helium. “Dry” dilution refrigerators provide an excellent continuous cooling and cost-effective performance at base temperatures of 10 mK. This is achieved by utilizing a Pulse Tube (PT) cryocooler, which provides cooling to 4 K. However, the PT represents a major source of mechanical and acoustical noise [188]. The noise is generated from a rotary valve that switches the connection of the PT between the high pressure helium gas output lines connected to a compressor at a frequency 1.4 Hz. Despite this main obstacle, there is a large effort in the scientific community to minimize the vibrations in “dry” cryostats. For example, scanning probe microscopy requires a low vibrational noise environment for precision measurements, and various vibration isolation techniques at low temperatures have been demonstrated [189–191]. Experiments on superconducting qubits can be affected by electrical noise in the coaxial cables originating from mechanical vibrations [192, 193].

Recent experiments attempting coherent control of the motion of a single electron on the surface of liquid helium have revealed the important role of helium surface fluctuations as a source of decoherence [104]. In these types of experiments, an electrostatic trap determines the motional frequency of the electron qubit and the helium surface fluctuations can lead to dephasing of the electron’s in-plane motional states, as discussed in Sec. 2.5.1. The helium surface fluctuations are naturally coupled to the mechanical vibrations of the cryostat. In this work we investigate the noise properties of a coplanar waveguide (CPW) covered with superfluid helium to quantify the contributions from the PT.

## 5.1 Superconducting coplanar waveguide resonator device

Fig. 5.1a and b show schematics of our measurement setup and a cross section of the CPW resonator, respectively. We patterned the  $\lambda/2$ -wavelength resonator on a high-resistivity ( $\rho \geq 10 \text{ k}\Omega\cdot\text{cm}$ ) Si substrate, where a 230-nm Al film was deposited via thermal evaporation. The Al resonator pattern is generated by exposing reverse image resist AZ5214E through a mask with traditional UV lithography. The resonator has a  $10 \mu\text{m}$  wide center strip with  $w = 5 \mu\text{m}$  gaps between the center strip and the ground plane. The length of the resonator,  $l = 45.54 \text{ mm}$ , corresponds to the measured resonator frequency  $f_r = \omega_r/2\pi = 1.315 \text{ GHz}$ . For this half-wavelength resonator, the fundamental frequency is defined as  $f_r = c/2l\sqrt{\epsilon_{\text{eff}}}$ , where  $c$  is the velocity of light in vacuum and the effective permittivity of the CPW line  $\epsilon_{\text{eff}} = 6.25$ , close to the calculated value  $\epsilon_{\text{eff}} \approx 6$  based on conformal mapping techniques [185]. The center strip of the resonator is coupled to the input transmission line via a finger capacitor with six pairs of fingers of length  $100 \mu\text{m}$ , width  $2 \mu\text{m}$  and separation  $2 \mu\text{m}$ ,

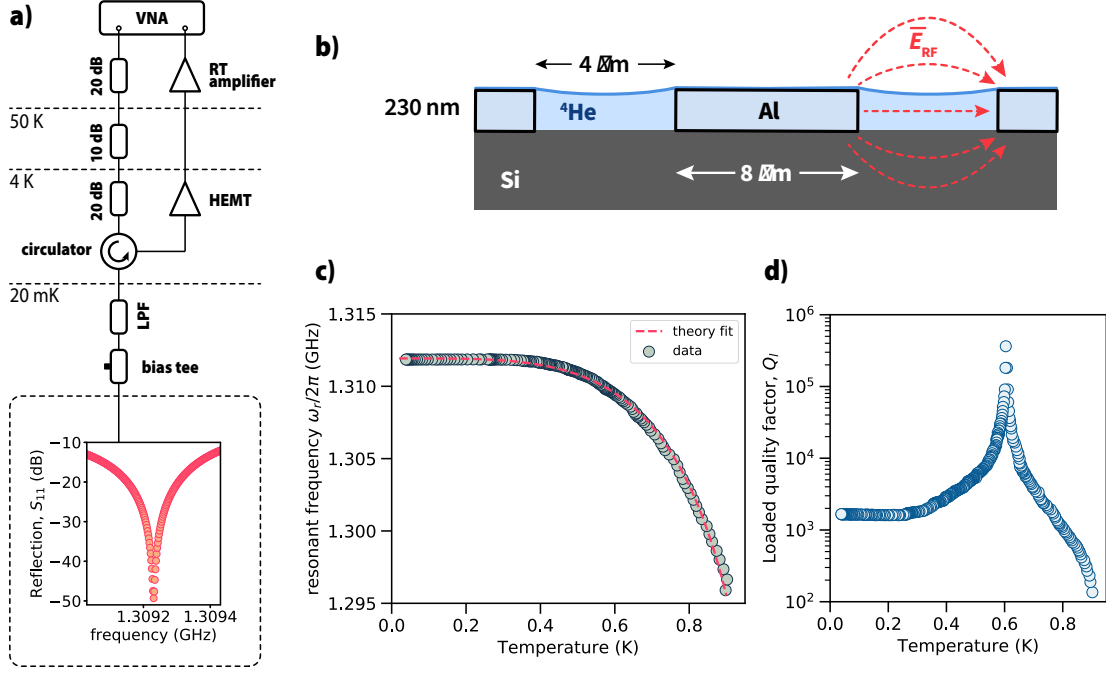


Figure 5.1: (a) The resonator measurement circuit diagram. The microwaves generated in VNA delivered into the sample cell (dashed box) through various attenuator inside the cryostat, cryogenic circulator, low pass filter and bias tee. The reflected signal from the resonator amplified by cryogenic HEMT amplifier and room temperature amplifier before entering the VNA input port. (b) The cross-sectional view of the resonator. Microchannels filled with superfluid helium occupy some part of the electromagnetic field mode volume of the resonator, changing its resonance properties. (c) The temperature dependence of the measured resonance frequency (circles). Dashed line represents a fit to a theoretical model. (d) Measured loaded quality factor, which shows anomalous behavior around 0.6 K.

which gives the capacitive coupling  $C_{\kappa} = 0.12$  pF, calculated from finite element modeling simulations.

## 5.2 Resonator spectroscopy

The frequency dependence of the reflection coefficient  $S_{11}$  was measured with a vector network analyzer (VNA). The microwave signal was attenuated by 20 dB at room temperature, followed by 10 dB and 20 dB of attenuation (at the 50K and 4K stages of the dilution refrigeration).

erator, respectfully) in order to reduce the spectral density of thermal radiation. Microwaves further propagate through a cryogenic circulator RADC-1.35-1.45-Cryo at the 4K stage, and a low pass filter K&L 4L250-4080 (with cut-off frequency 4 GHz) and bias tee Anritsu K250 (in these experiments the dc bias was not used) at the mixing chamber stage with a total insertion loss  $< 4$  dB. The CPW resonator was mounted into custom made printed-circuit board (PCB) located inside the hermetically sealed sample cell attached to the mixing chamber plate of the cryostat. The microwave signals enter the sample cell through hermetic SMP connectors. The reflected signal from the resonator passed back through a circulator with 20 dB isolation to protect the resonator from noise in cryogenic low-noise HEMT amplifier LNF-LNC1.5\_3.5A with a noise temperature of  $\sim 7$  K and gain of 27 dB. At room temperature, the signal is further amplified by a Mini-Circuits ZKL-2R5+ amplifier with a gain of 30 dB.

Typical reflection measurements from the resonator as a function of frequency is shown in Fig. 5.1a (measured at  $T = 0.6$  K) and in inset of Fig. 5.2 (measured at  $T \sim 0.1$  K). The data was acquired with input power -50 dBm, low enough to avoid nonlinearities from high power input. We note, that the resonance curves in inset of Fig. 5.2 show small asymmetry likely arising due to impedance mismatch in the transmission lines or bonding wires [194]. Fig. 5.1c shows the temperature dependence of the resonant frequency. In order to describe this dependence we use lumped element approximation for the resonance frequency, which scales as  $\omega_r \propto 1/\sqrt{L}$  with inductance. The inductance here is a sum of a temperature independent geometric (magnetic) inductance  $L_m$  and temperature dependent kinetic inductance of a superconductor  $L_k$ . The temperature dependence of the kinetic inductance governed by the London penetration depth, which scales as  $L_k \propto \lambda^2(T) \propto (1 - (T/T_c)^4)^{-1}$  [195] with  $T_c = 1.2$  K being critical temperature for Al. We find the best fit of a theoretical function to

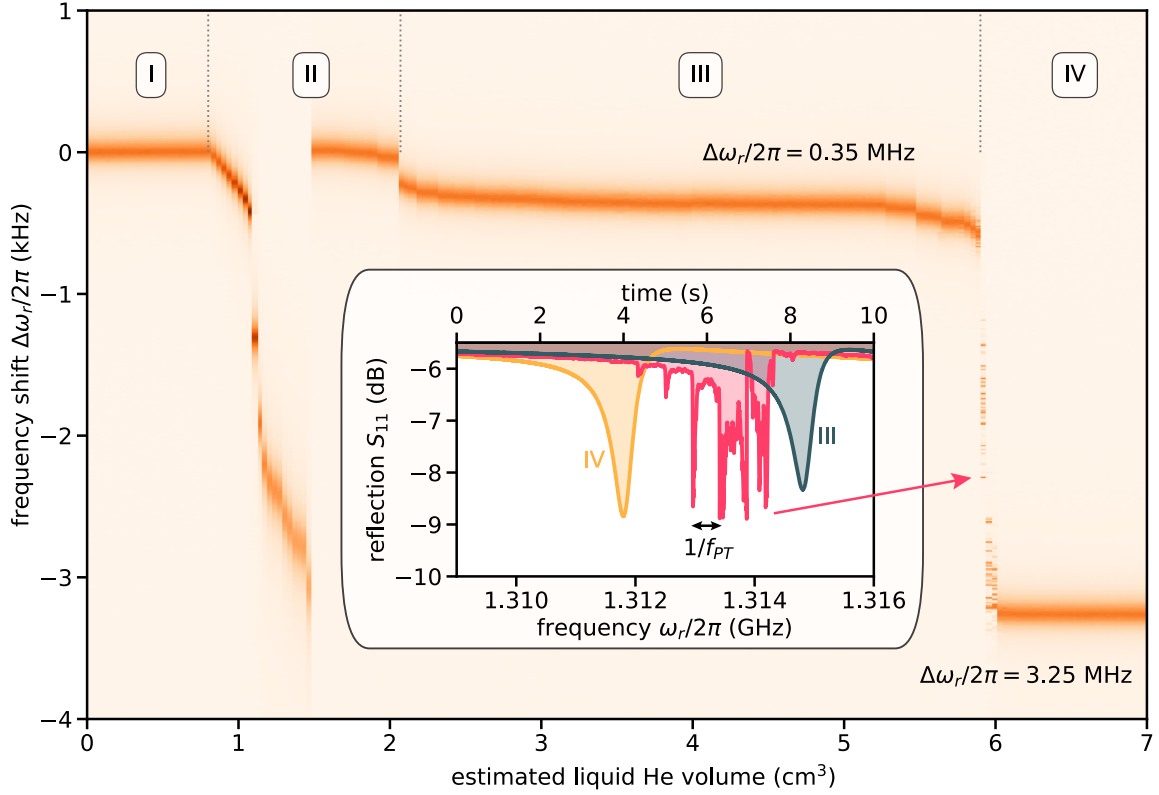


Figure 5.2:  $S_{11}$  power spectrum during the liquid He condensation process. Regions I, II, III and IV indicate different filling regimes as described in the main text. The inset shows the vertical linecuts in regions III, IV demonstrating a distinct shift of the resonance frequency. The linecut at the boundary between these regions shows the periodically distorted resonance conditions during the frequency sweep at the pulse tube frequency.

experimental data with a ratio parameter  $L_k/L_m \approx 0.06$  (see Fig. 5.1c). The loaded quality factor of the resonator is determined as  $Q_l = f_r/2\delta f_r$ , where  $\delta f_r$  is the full width at half max of the power spectrum. Fig. 5.1d shows the temperature dependence of measured  $Q_l$ . At low temperatures  $Q_l$  saturates at values  $1.7 \times 10^3$ . We observe an anomalous increase of the quality factor by 2 orders of magnitude near the temperature  $T = 0.6$  K. We believe that this behavior originate from the internal properties of the resonator, however the origin of the physics remains unknown. We note, that the data presented here acquired from one sample and further investigation with different samples are necessary.

### 5.3 Resonator response to liquid helium

Replacing the vacuum above the resonator with low loss dielectric medium - the liquid helium - changes the electrostatic environment which results in a shift of its resonance frequency. We monitored a frequency shift by measuring power spectrum during the helium condensation process, which is shown in Fig. 5.2. The liquid helium introduced into the sample cell through a stainless still capillary line, and helium is thermally anchored using sintered silver heat exchanger at the 1K stage of the cryostat. During the condensation process the temperature of the mixing chamber varied from 100 mK up to 200 mK. We approximately estimate the condensed liquid helium volume from the pressure changes in the helium tank at room temperatures. We observe four regions with distinct behavior shown in Fig. 5.2. In the first region I the resonance frequency doesn't change, which we associate with the filling of the dead volume in the silver sinter first. The second region II indicates the introduction of the liquid helium in the form of unsaturated thin van der Waals film into the sample cell, which covers the surface of the resonator and all walls of sample cell. Observed large shift of the  $\omega_r/2\pi$  in this region we associate with the increase of the resonator's temperature due to introduction of a "hot" helium initially thermalized at 1K stage. After approximately 3-5 mins the resonance frequency abruptly shifts back to its original value, which we attribute to the thermalization of the liquid helium to a mixing chamber plate temperature. We note that this behavior is reproducible upon the warming up the cell to room temperature and a cooldown with prior evacuating of the sample cell procedure. However, if the cell is warmed up only to 20 K (which results in residual  $^4\text{He}$  gas in the cell) and cooled back down, this feature is not observed. We also note that the condensation rate controlled by the needle valve at the room temperature slightly changes the details of the observed shift

features. This all indicates to a nonequilibrium processes during the thermalization of the liquid helium and the sample substrate, which has complex physical nature. Once the bulk helium is formed at the bottom the cell, the thickness of the helium film on the resonator starts to grow as  $d = (\gamma/\rho g H)^{1/4}$  [94], where  $\gamma$  is the van der Waals constant,  $\rho = 146 \text{ kg/m}^3$  is the mass density of liquid He,  $g$  is the acceleration due to gravity, and  $H$  is the distance from the resonator surface down to the bulk liquid helium level in the cell. At the same time the microchannel regions between central pin and ground plane starts to fill with superfluid due to capillary action (region III in Fig. 5.2). The thickness of the liquid helium in the microchannels is determined by a balance of the hydrostatic pressure caused by gravity and the surface tension, and is given by  $h \simeq d_r - \rho g H w^2 / 16 \sigma_t$  [90], where  $d_r = 230 \text{ nm}$  is the depth of the microchannel,  $\sigma_t = 3.58 \times 10^{-4} \text{ N/m}$  is the surface tension of liquid helium. Once the helium fills microchannels completely we measure the frequency shift of the resonator  $\Delta\omega_r/2\pi = -0.35 \text{ MHz}$ , which is in a close agreement with our Finite Element Modeling (FEM) calculations  $\Delta\omega_r^{\text{FEM}}/2\pi = -0.31 \text{ MHz}$ . The onset of the region IV indicates the level of the bulk helium  $H \rightarrow 0$ , and the formation of bulk volume of liquid above the resonator chip. Interestingly at the boundary between regions II and IV we do not observe a single resonance feature in the power spectrum, but rather a sharp periodic changes in the reflection coefficient appear during the frequency sweep in a 10s span time. The frequency of these periodic features is equal to a main harmonic of the pulse tube. This indicates the generation of the large surface excitations in the bulk helium by mechanical vibrations in the cryostat driven by pulse tube. In the last region IV we measure the frequency shift  $\Delta\omega_r/2\pi = -3.25 \text{ MHz}$ , which is also in a good agreement with our numerical calculations  $\Delta\omega_r^{\text{FEM}}/2\pi = -3.33 \text{ MHz}$ . We would like to emphasize a similar investigations of the helium filling the microwave resonator have been done in ref. [104], where a similar behavior of the

resonance shift were observed with small differences due to different resonator geometry.

## 5.4 Investigating helium surface fluctuations

In order to measure helium surface fluctuations we partially fill microchannels with liquid helium and operate in a region II shown in Fig. 5.2. The fluctuations on helium surface changes the participation volume of the dielectric medium in the electromagnetic mode volume, thus changing resonator's frequency. Therefore the information about the helium fluctuations is embedded in the resonator's noise properties. We recorded the reflection coefficient as a function of time at fixed frequency  $f_0$  corresponding to the highest slope on the power spectrum. A 40-s traces were recorded at a sampling rate 400 Sa/s limited by the bandwidth of the VNA. The spectral densities of the measured noise  $S_{\text{dB}}$  are computed by Welch's average periodogram method. For a reference, we show spectral densities of measured  $S_{11}$  in the absence of liquid helium (region I) and when the resonator is completely submerged in liquid helium (region IV) in Fig. 5.3a. Here we observe electric 60 Hz noise and several distinct resonances, which potentially can originate from mechanical fluctuations of bonding wires. The spectral density changes qualitatively when liquid helium fills microchannels. Fig. 5.3b shows the spectral density of the frequency fluctuations calculated as  $S_f = S_{\text{dB}}(\partial S_{11}/\partial f)^{-1}$  measured at temperature 10 mK. We observe several resonances corresponding to harmonics of the pulse tube at frequencies  $n * f_{\text{PT}}$ , which were absent in Fig. 5.3a. These resonances can be modestly enhanced by inducing mechanical vibrations in the cryostat frame. The majority of PT harmonics disappear or their amplitude reduces when the PT is turned off. A noticeable feature in frequency range 30-60 Hz originate from a building vibrations, which excite cryostat vibrational modes. This was confirmed by a frequency shift after providing

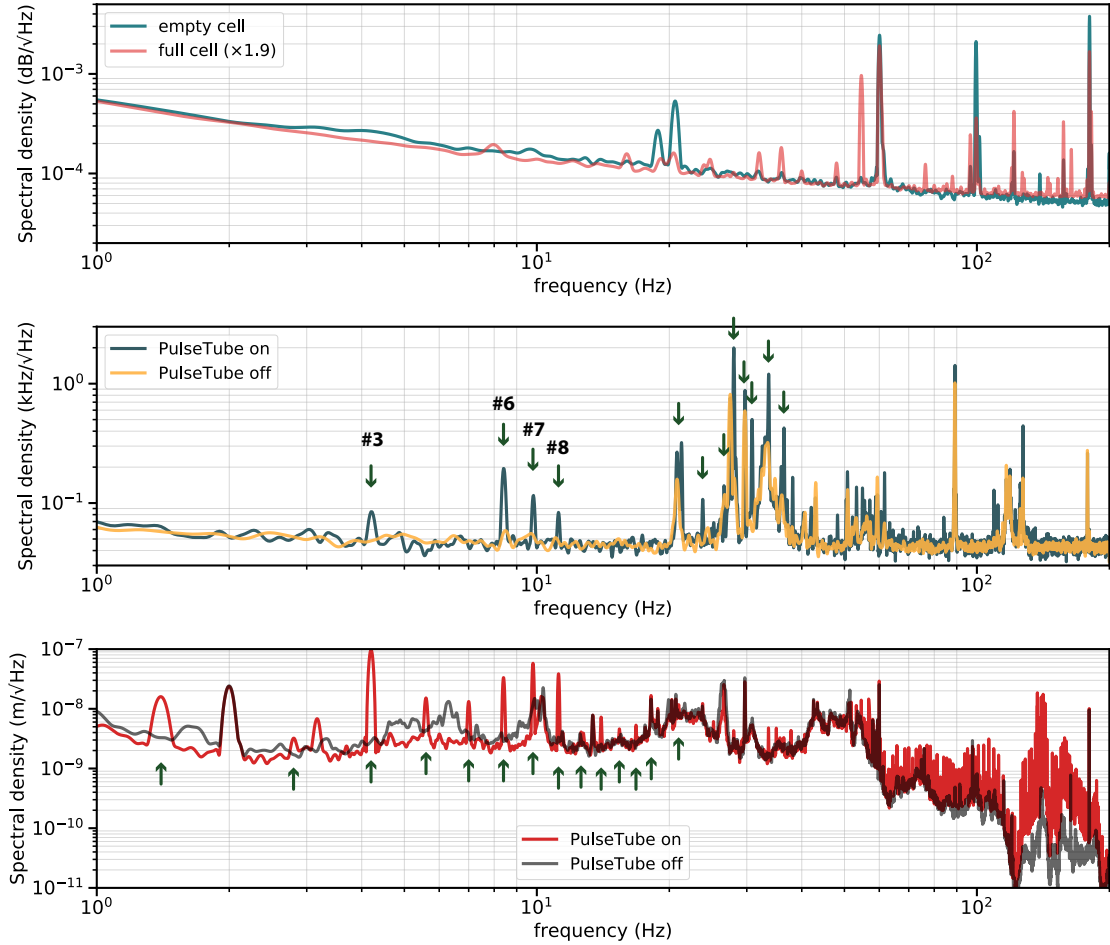


Figure 5.3: (a) Noise spectral density  $S_{dB}$  of the resonator in the absence of liquid helium and when the resonator completely submerged into liquid. Measurements are done at  $T = 20$  mK. (b) Spectral density  $S_f$  of the frequency fluctuations with superfluid partially filling the microchannels. PT harmonics are indicated by arrows. (c) Noise spectral density of vertical vibrations of the mixing chamber plate measured via geophone. Measurements are done at room temperatures. Arrows show PT harmonics.

additional support structure to the cryostat's OVC. These all indicates that the majority of helium fluctuations originate from mechanical vibrations of the cryostat body and frame. The integrated RMS vibrations are calculated as:

$$\Delta h_{\text{RMS}} = \left(\frac{\partial f_r}{\partial h}\right)^{-1} \sqrt{\int_{f_1}^{f_2} S_f^2 df}, \quad (5.1)$$

where  $\partial f_r/\partial h = 1.4$  kHz/nm is obtained from FEM calculations. We estimate  $\Delta h_{\text{RMS}} = 0.9$  nm by integration the data on Fig. 5.3b between frequencies 1 Hz and 200 Hz in the case of PT on. This value reduces to 0.77 nm when the PT is off.

To gain additional information about the vibrations we performed measurements on the geophone attached to the mixing chamber plate. A geophone consist of a spring loaded mass attached to a magnet, which moves relative to a solenoid. Small vertical motion of a magnet produces the voltage on the solenoid, which can be further measured and converted to a displacement. We use Geophone Sensor RTC-4.5Hz-375 with natural frequency 4.5 Hz, below which the sensitivity of the sensor is small. The signal from geophone is further amplified by NF LI-75A low noise current preamplifier with gain 100 and recorded with MC USB-1602HS digitizer at a 2 kSa/s rate. We perform the geophone calibration procedure to relate measured voltages to a magnet displacement as described in ref. [196]. Fig. 5.3c shows the noise spectrum of the vibrations measured on geophone attached to the mixing chamber plate at room temperature with PT on and off. The PT harmonics are clearly visible at low frequencies and at frequencies  $> 60$  Hz, which disappear once the PT is off. From this measurements we estimate the total root mean square displacement noise with PT on and off is 58 nm and 47 nm, respectfully.

All the preliminary experiments, presented here, indicate that the major source of the

mechanical vibrations originate from the PT cryocooler, which then couple to helium fluctuations in the microchannels. There are several possible solutions to reduce fluctuations of the helium surface, for example by mechanically disconnecting the cold head from the cryostat frame, or by using suspended spring stage [190, 197] and adding eddie current dampers [189]. These various vibration isolation techniques should be applied with careful consideration of thermal anchoring.

## 5.5 Summary of results

In conclusion, we have studied a CPW resonator's properties in the presence of the superfluid helium filled microchannel structures. We identified different regimes of the resonator's response depending on the amount of liquid helium in the sample cell. Our results on the frequency shift of the resonator are consistent with FEM calculations. There are open questions, like the anomalous temperature dependence of the quality factor, which needs further investigation.

# Chapter 6

## Conclusion and outlook

Throughout this thesis, we have shown progress in developing architectures for investigating and controlling well-defined collective excitations in electron ensembles trapped above the surface of superfluid helium. By placing superconducting resonators in these architectures, we establish a pathway towards novel regimes of many-body circuit quantum electrodynamics and cavity optoplasmonics with electrons on helium.

### 6.1 Summary of work

In Chapter 3, we show that these collective excitations, in the form of charge density waves, i.e. plasmons, can be precisely engineered and spatially controlled using a microchannel device architecture. In this work, we realize microwave frequency plasmon modes, which we can detect via low-frequency transport measurements, and we find that the modes are tunable with electron density over a broad range ( $\simeq 3$  GHz). Microwave drive power dependent transport measurements allow us to investigate the various broadening mechanisms of the plasmon modes. In particular, we find there exists an evolution from intrinsic to inhomogeneous broadening contributions from low to high power, and we estimate a lower bound plasmon lifetime  $\tau_p \sim 1$  ns. The modes being in the microwave frequency regime make them compatible with the frequency regimes of circuit quantum electrodynamics (cQED) devices, such as superconducting coplanar waveguide (CPW) resonators and superconducting qubits.

In Chapter 4, we utilize the microchannel geometry that enables us to generate the microwave frequency plasmon modes and fabricate a superconducting CPW resonator onto the device, such that the electron system and resonator can couple. In this work, we investigate how the two systems affect on another, through both transport experiments and resonator spectroscopy measurements. By driving the microwave resonator through its resonance frequency while doing simultaneous transport measurements, we can measure the resonance frequency of the CPW resonator via the non-equilibrium heating of the electron system we observe in the transport conductance signal. We also perform resonator spectroscopy measurements as a function of increasing electron density in the central channel. This corresponds to tuning the two-dimensional electron system through densities that correspond to a plasmon frequency  $\omega_p/2\pi \propto \sqrt{n_s}$ . Because of this, as we continuously drive the resonator through its resonance frequency  $\omega_r/2\pi$ , we see an avoided crossing occur when the electron system is tuned into a density such that  $\omega_p(n_s) \approx \omega_r$ . By modeling the hybrid system as two classical coupled oscillators, we can simulate our the resonator response and we find that the systems couple with an effective coupling rate  $g_{\text{eff}}/2\pi = 50$  MHz. Moreover, by performing finite element modeling (FEM) calculations of the electric field produced by the resonator, we find the mode likely mode being generated is the  $n = 3$  plasmon mode and that it has a loss rate of  $\gamma/2\pi \simeq 150$  MHz.

Finally, in Chapter 5 we show how a superconducting coplanar waveguide resonator can be used as a tool to understand how superfluid helium affects these types of devices. In this work, spectroscopy measurements allow us to track how much helium has filled the microchannel structures based on the resonator shift in frequency. This resonator frequency shift is a result of the helium changing the effective dielectric of the device, leading to a decrease in resonator frequency as more helium is introduced into the channels. We also find

that placing this superconducting resonator into superfluid helium allows us to investigate the helium surface fluctuations. In particular, from noise spectral density measurements, we can detect the fluctuations that result from the pulse tube of the dilution refrigerator. These kinds of measurements allow us to better understand the noise we might anticipate seeing in future sensitive quantum devices integrated with electrons on helium architectures.

## 6.2 Outlook and future directions

I have often said that if I could be a graduate student forever, doing these experiments with electrons on helium and quantum circuits indefinitely to my heart's desire, I would. But unfortunately that is not feasible, and many of the experiments I would have liked to do are left up to future generations. Here, a few ideas are outlined that I believe would help progress the work discussed throughout this thesis for future ambitious graduate students.

### 6.2.1 Resolving the unresolved: Wigner crystal *sliding* vs *melting*

One particular phenomenon that remains a mystery throughout the entire electrons on helium community is understanding the non-linear and non-equilibrium behavior of the electron system when perturbed with a high driving field. This was discussed throughout Chapters 2, 3, and 4, where we attempt to understand through our data and past experiments whether the high conductivity regime we observe is a sliding Wigner crystal or an electron liquid heated out of equilibrium. Future experiments using architectures similar to the hybrid microchannel-resonator device from Chapter 4 could help to uncover the unresolved microscopies of this phenomenon. Experiments like the transport assisted cavity spectroscopy in Sec. 4.2 as a function of dilution refrigerator temperature as well as a function of the

ac drive voltage  $V_{\text{ac}}$  could help elucidate whether the high conductivity phenomenon is a heating effect or a sliding effect.

### **6.2.2 Towards strong coupling with a longer lifetime plasmon in electrons on helium**

In Chapter 4, while the architecture allowed us to demonstrate the resonator-plasmon coupling we set out to do, both the plasmon loss rate and cavity loss rate were high. Additionally, experiments on the higher quality factor resonator showed worse coupling rates, likely due to the fact that the number of electrons  $N$  that corresponds to the plasmon frequency at which  $\omega_p \simeq \omega_r$  is lower, and typically the coupling  $g \propto \sqrt{N}$ . One of the likely contributions to the lossy plasmon mode is the ill-defined boundary condition, set by a small density inhomogeneity at the edges of the channel where the resonator couples to the electron system. To demonstrate strong coupling between the plasmon and resonator, a future device architecture could place the channel gate electrodes (see Fig. 4.6a) on either side of the channel where the resonator foot couples to the channel. This would help set a well-defined (and tunable!) plasmon wavelength and limit the loss from the energy leakage into the surrounding electrons in the channel that are not participating in the charge density wave oscillation.

### **6.2.3 Regimes of cQED and cavity optoplasmonics with plasmons in electrons on helium**

If one can design a microchannel architecture that can host a long-lived plasmon, coupling the plasmon to a high-quality factor resonator opens the door to circuit quantum electrodynamics (cQED) and cavity optoplasmonics with electrons on helium plasmons. A device architecture

that could enable experiments within the framework of cQED would be a microchannel device architecture similar to the ones described in this thesis, coupled to a superconducting qubit via a bus resonator. If one could successfully demonstrate a lower loss plasmon following from the ideas listed in the prior paragraph, experiments such as quantum bath engineering [149, 151, 198, 199] could be realized with plasmons in electrons on helium.

Moreover, if one designs a microchannel that can host plasmons in the MHz frequency range, one could also realize experiments similar to those done in the field of cavity optomechanics. For example, a 500  $\mu\text{m}$  long channel could host a  $\approx 500$  MHz fundamental plasmon mode. By designing the channel gate electrodes as discussed in Sec. 6.2.2, one could apply an external microwave drive to the electron system to drive the 500 MHz plasmon mode, while performing simultaneous resonator spectroscopy measurements. When coupled, one could anticipate resolving sidebands in the resonator spectroscopy at  $\pm 500$  MHz, and even demonstrate cavity optomechanical phenomenon [200, 201] like sideband cooling and amplification of the mechanical motion [202–206] of the charge density wave.

## APPENDICES

# Appendix A

## Measurement apparatus, circuits, and protocol

### A.1 Measurement apparatus and circuit components

Table A.1 and Table A.2 show the main measurement apparatus and circuit components used in the measurements described in this thesis. The full circuit diagrams for the experiments with these listed components are diagrammed in Sec. A.3 and Sec. A.4.

Measurement apparatus	
Description	Model
DC voltage sources	Yokogawa GS200 and Yokogawa 7651
Vector network analyzer (VNA)	Keysight N5230A PNA-L Network Analyzer (2-ports), 300 kHz - 13.5 GHz
High frequency lock-in amplifier	Stanford Research Systems, Model SR844
Waveform generator (WG)	Keysight 33500B Waveform Generator
Spectrum analyzer	Signal Hound, SA124B
High frequency (HF) source	Signal Core SC-5511A
Data acquisition device (DAQ)	Measurement Computing USB-2404-10

Table A.1: Table of the measurement apparatus used for the experiments described in this thesis.

Circuit components	
Description	Model
Bias tee (MC)	Mini Circuits Bias-Tee, 0.1 MHz - 6000 MHz, ZFBT-6GW+
Bias tee (A)	Anritsu Bias-Tee, 0.1 - 40 GHz, K250
Low pass filter (SLP-5+)	Mini Circuits LC Low pass filter, DC - 5 MHz, 50 $\Omega$ , SLP-5+
Low pass filter (SLP-2950+)	Mini Circuits LC Low Pass Filter, DC - 2700 MHz, 50 $\Omega$ , SLP-2950+
Low pass filter (EF-112)	Thor Labs Low-Pass Electrical Filter, $\leq 2$ kHz Passband, EF-112
Low pass filter (EF-120)	Thor Labs Low-Pass Electrical Filter, $\leq 10$ kHz Passband, EF-120
Amplifier (ZFL)	Mini Circuits Low Noise Amplifier, 50 $\Omega$ , 0.1 MHz - 500 MHz, ZFL-500LN+
Amplifier (ZX60)	Mini Circuits Linear Amplifier, 500 MHz - 8000 MHz, 50 $\Omega$ , ZX60-83LN-S+
Cryogenic microwave low pass filter (K&L)	K & L Microwave, 6L250 Tubular Low Pass Filter, 6L250-10000/T20000-O/O
Cryogenic filter epoxy	Cuming Microwave, C-RAM KR-112

Table A.2: Table of the main circuit components used for the experiments described in this thesis.

## A.2 Pre-experiment device preparation

### A.2.1 Sample cell “pump & flush” procedure

Once the sample cell is closed up (using a superfluid-leak-tight seal with an indium o-ring) and mounted onto the mixing chamber plate of a dilution refrigerator, before cooling it down, it is cleaned out by doing a “pump & flush” procedure. The procedure utilizes an external pump station (EPS) – consisting of an Agilent Varian Dry Scroll pump and Pfeiffer Vacuum TMU-261 Compact Turbo pump – and an external helium gas handling (EGHS) system. The “pump & flush” procedure is as follows:

1. The sample cell is pumped down using the EPS scroll pump for approximately 45 mins.

2.  $\simeq 350$  Torr of helium gas (measured at the channel 2 pressure gauge on the EGHS) is let into the sample cell – this takes approximately 5 – 10 minutes to reach the sample cell in the dilution refrigerator (Helios) where the experiments in this thesis were performed.
3. After waiting  $\simeq 10$  mins, the sample cell is pumped down again using the EPS scroll pump for approximately 45 mins.
4. Steps (1) and (2) are repeated such that each step is completed 6 times.
5. On the final pump, the cell is pumped out via the turbo pump and left to pump for 12 – 24 hours.

### **A.2.2 Condensing helium into sample cell**

Once the dilution refrigerator reaches  $T \simeq 100$  mK, before turning on the turbo pump in the dilution circulation, helium is condensed into the sample cell. The helium is condensed from a 22 L room temperature tank connected to the EGHS and is circulated through a cold trap submerged in liquid nitrogen before entering into the capillary fill line that leads down to the sample cell at the mixing chamber plate of the dilution refrigerator. Because the helium being condensed is coming from a room temperature volume, the pressure corresponding to the flow rate of helium into the capillary line (channel 2 on the EGHS) is kept low to keep the fridge from warming up. Typically, we start with pressures  $P_{\text{Ch}_2} \simeq 15$  Torr for the first 10 – 15 Torr of helium out of the tank – the amount of helium condensed is monitored by the change in helium pressure in the 22 L tank (this is the channel 1 pressure  $P_{\text{Ch}_1}$ ). After  $\Delta P_{\text{Ch}_1} \simeq 15$  Torr, the flow rate of helium can be slowly increased, however we typically do not exceed  $P_{\text{Ch}_2} \simeq 45$  Torr. As helium is condensed into the cell, the still temperature on

the dilution refrigerator is monitored, such that the temperature does not increase above  $T_5 \simeq 1.2$  K. The amount of helium required to fill the microchannels of the device varies device to device. For the device in Chapter 3, we typically found  $\Delta P_{\text{Ch}_1} \simeq 75 - 125$  Torr was sufficient. With the device in Chapter 4, filling was more straightforward, as we could monitor the amount being filled via the resonator shift, as discussed in detail in Chapter 5. For the microchannel-resonator hybrid device, we found  $\Delta P_{\text{Ch}_1} \simeq 80 - 100$  Torr to be the filling sweet spot (see Sec. A.4.1).

### A.2.3 Electron firing procedure

Once the helium is condensed into the sample cell, the helium is left overnight to stabilize before electron deposition is performed. Electrons are fired via thermionic emission of the tungsten filament that is wired into the device PCB. The filament is connected at room temperature to superconducting twisted pairs down the fridge. One leg of the filament is grounded at room temperature and the resistance across the filament at base temperature should be  $8 \Omega$  – at room temperature, it is typically  $25 \Omega$ . A Keysight 33500B Waveform Generator is used to send a single, manually triggered, inverted square pulse to the filament. The square wave is typically between  $-1.6 V_{\text{pp}}$  to  $-2.0 V_{\text{pp}}$ , with an offset of half the amplitude of the pulse, and a total pulse duration of  $200 - 400$  ms. For the device in Chapter 3, trapping electrons into the microchannels was most successful when the mixing chamber was heated to temperatures of  $T \simeq 400 - 600$  mK. Additionally, before firing electrons, we would apply the following voltages to the electrodes:  $V_{\text{res}} = 1.2$  V,  $V_{\text{res}} = 0.7$  V,  $V_{\text{ac}} = 50$  mV,  $f_{\text{ac}} = 3$  MHz. In contrast, the microchannel-resonator hybrid device did not seem to be sensitive to the temperature of the system to successfully trap electrons. We found we could trap electrons anywhere between  $T = 50$  mK –  $450$  mK. The applied electrode

voltages for successful trapping in this hybrid device were similar to those in the former device, however, as discussed in the main text, the electrodes corresponding to the unused side microchannel device were biased negatively (see Sec. 4.1.2).

### A.3 Plasmon mode engineering device

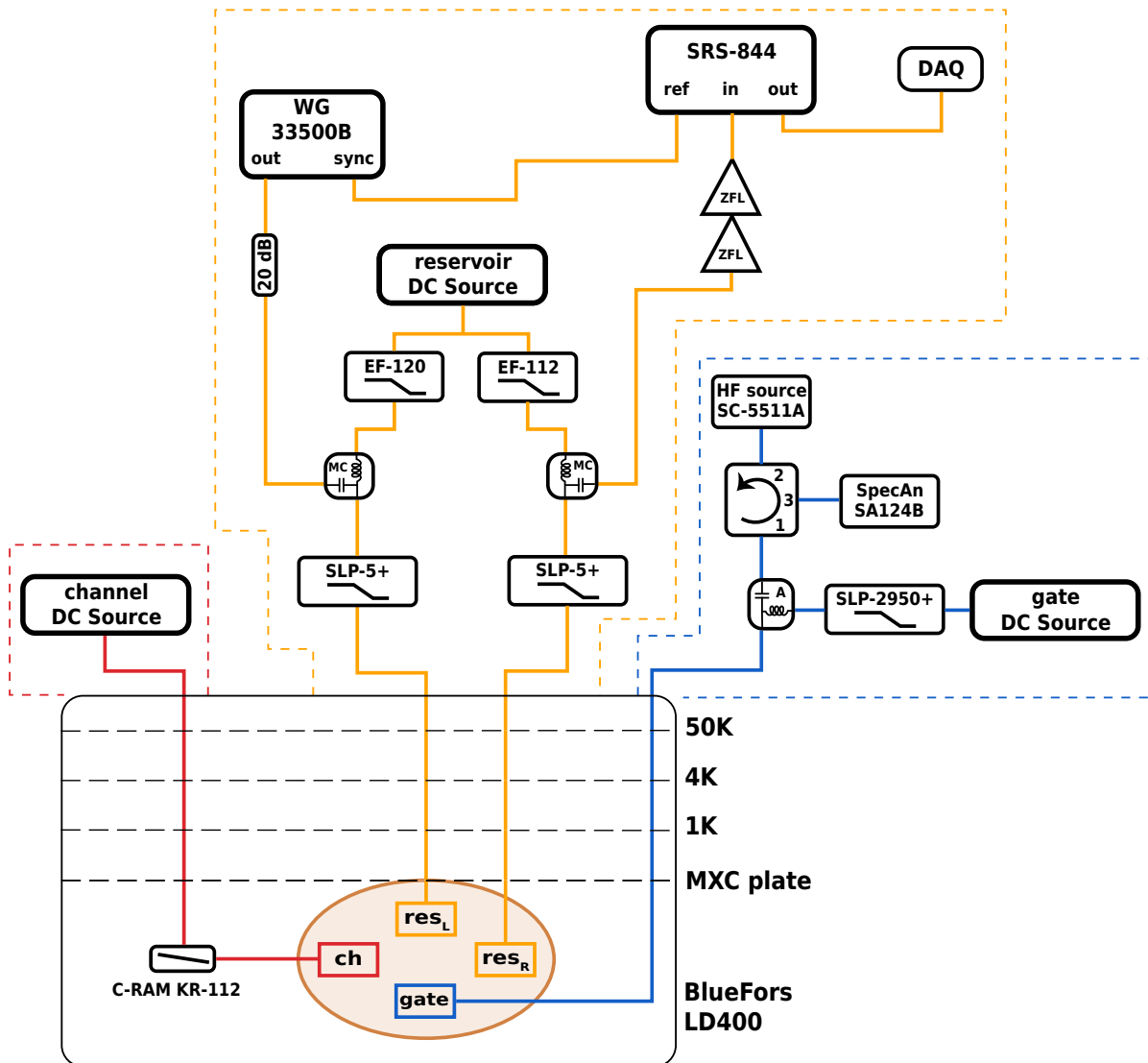


Figure A.1: Full circuit diagram for experiments on the device described in Chapter 3. See Table A.1 and Table A.2 for full description of listed components.

## A.4 Microchannel-resonator hybrid device

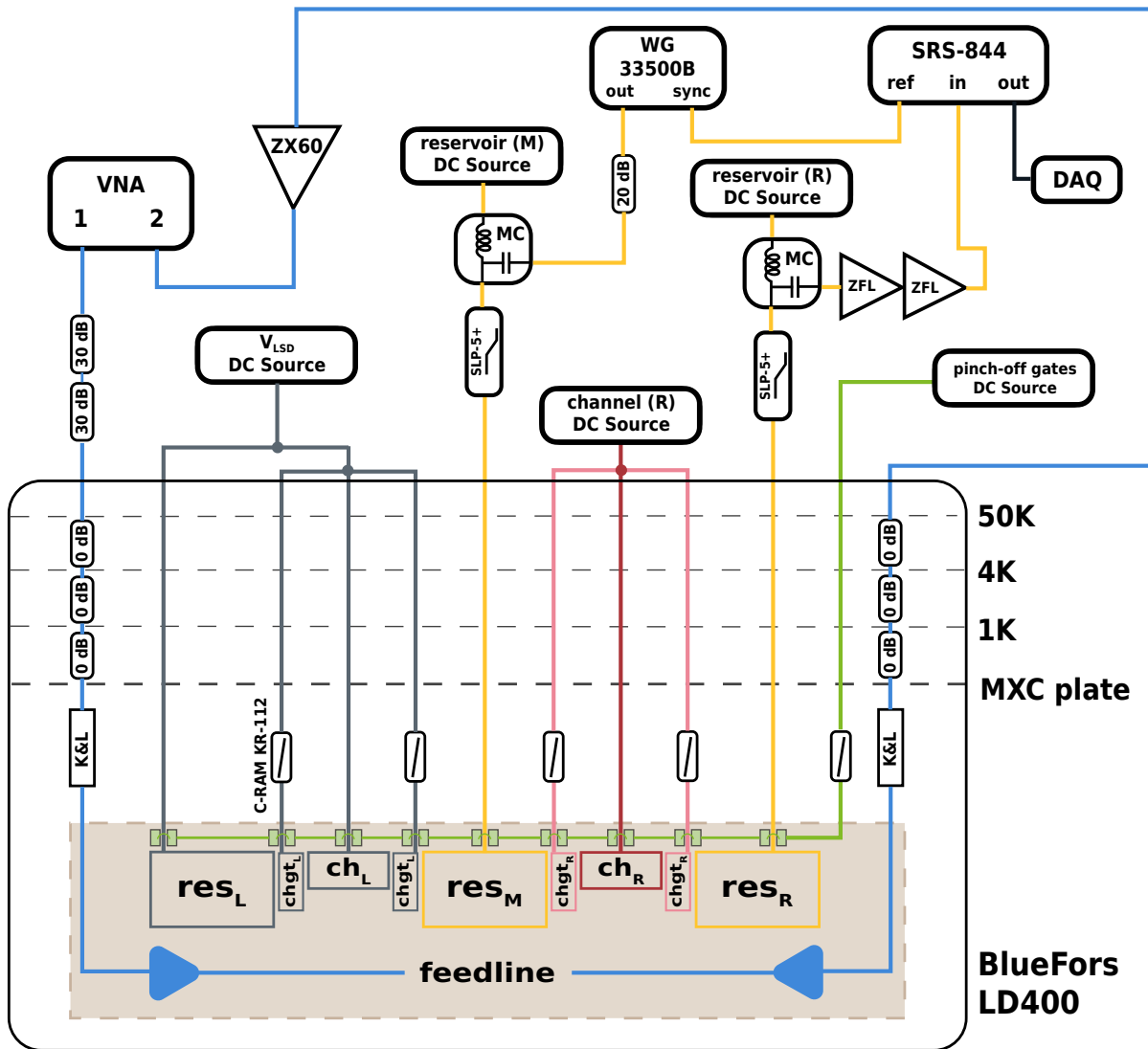


Figure A.2: Full circuit diagram for experiments on the device described in Chapter 4. See Table A.1 and Table A.2 for full description of listed components.

### A.4.1 Helium filling characteristics of the resonators

As discussed in detail in Chapter 5, as helium fills the sample cell, a resonator device will shift in frequency as a function of the amount of helium covering the device. We performed similar spectroscopy measurements for the resonator devices in the microchannel-resonator hybrid device from Chapter 4.

A sketch of the filling regimes for the cross section of these resonators is shown in Fig. A.3. The four regimes are as follows: (I) no helium is condensed in the device and the resonator frequency is the bare resonator frequency in the absence of helium; (II) helium is just barely introduced into the device and begins to fill the main surfaces with a thin van der Waals film, just slightly shifting the resonator frequency; (III) a large enough volume of helium has filled the cell such that the channels throughout the device fill via capillary action and the resonator shifts down in frequency on the order of 1 – 2 MHz; (IV) a large helium bulk in the cell causes the channels to over fill beyond the capillary meniscus and the entire device lives beneath the bulk helium layer within the cell, causing a frequency shift  $\Delta\omega/2\pi > 10$  MHz.

The filling data that corresponds to the regimes discussed above is shown for the left side device resonator in Fig. A.4 and for the right side device resonator in Fig. A.5. In both figures, the resonator data is plotted as a function of the difference in the 22 L room temperature helium tank pressure  $\Delta P_{\text{Ch}_1}$ , where Ch<sub>1</sub> is the corresponding pressure gauge (Pfeiffer DPG 202) we monitor on the helium filling external gas handling system.

For both figures, panel (a) shows the resonator shift  $\Delta\omega_{(R/L)}/2\pi$  as a function of the change in the room temperature helium tank pressure  $\Delta P_{\text{Ch}_1}$ . The data points were extracted by fitting the spectroscopy data shown in panel (b) to Lorentzian distributions. The linewidth for each point was also extracted and the loaded quality factor is plotted in panel

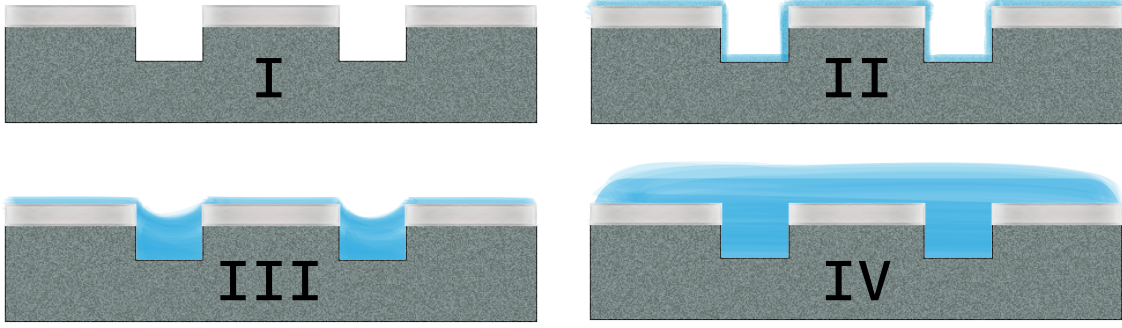


Figure A.3: Cross section of CPW resonator showing how superfluid helium fills the resonator device via capillary action. The four filling regimes discussed in Chapter 5 are shown: (I) no helium is in the device, (II) helium begins to create a van der Waals film throughout the surfaces of the device, (III) helium fills the channels via capillary action, (IV) a large amount of helium has filled the device and created a bulk helium level beyond the height of the device.

(c), where  $Q_L = \omega/\kappa$ . In the experiments performed here, we found the sweet spot for filled channels and stable electron trapping to be at  $\Delta P_{\text{Ch}_1} \simeq 80 - 100$  Torr.

#### A.4.2 Reservoir voltage dependence for avoided crossing measurements

As discussed in Chapter 4, we can confirm the avoided crossing feature we see in our resonator spectroscopy measurements as a function of channel electron density is coming from the electrons in the channel by performing these measurements at varying reservoir voltage. These measurements are shown in Fig. A.6. These measurements correspond to the extracted data points in Fig. 4.10.

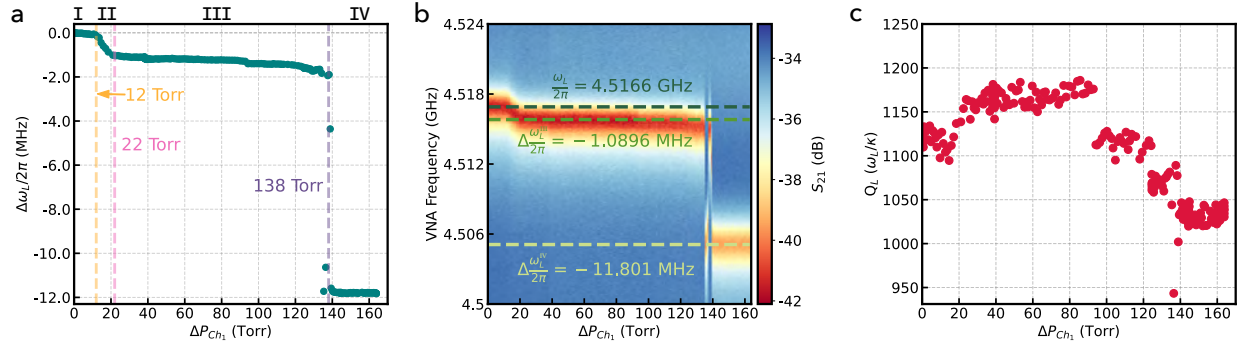


Figure A.4: Helium filling characteristics of the left side resonator ( $\omega_L \simeq 4.5$  GHz). (a) Plot showing the shift in resonator frequency  $\Delta\omega_L/2\pi$  as a function of the pressure difference from the helium tank at room temperature  $\Delta P_{\text{Ch}_1}$ . The four filling regimes corresponding to Fig. A.3 are indicated in Roman numerals. The pressure difference in the helium tank when the resonator shifts into a different filling regime are labeled accordingly. Each resonance frequency was extracted by fitting the spectroscopy data to a Lorentzian distribution. (b) Resonator spectroscopy as a function of the helium tank pressure difference  $\Delta P_{\text{Ch}_1}$  from which the frequency shifts in (a) were extracted from. Dark green dashed line shows the initial resonator frequency  $\omega_L/2\pi = 4.5166$  GHz in the absence of helium and lighter green dashed lines show the two main helium shifted frequencies,  $\Delta\omega_L^{\text{III}}/2\pi = -1.0896$  MHz, and  $\Delta\omega_L^{\text{IV}}/2\pi = -11.801$  MHz. (c) Resonator loaded quality factor  $Q_L$  as a function of helium filling.  $Q_L$  is calculated by extracting the full-width at half-maximum (i.e. the linewidth  $\kappa$ ) from the Lorentzian fit used to extract the points in (a), then the loaded Q-factor is calculated ( $Q_L = \omega/\kappa$ ) for each helium tank pressure dependent spectroscopy measurement.

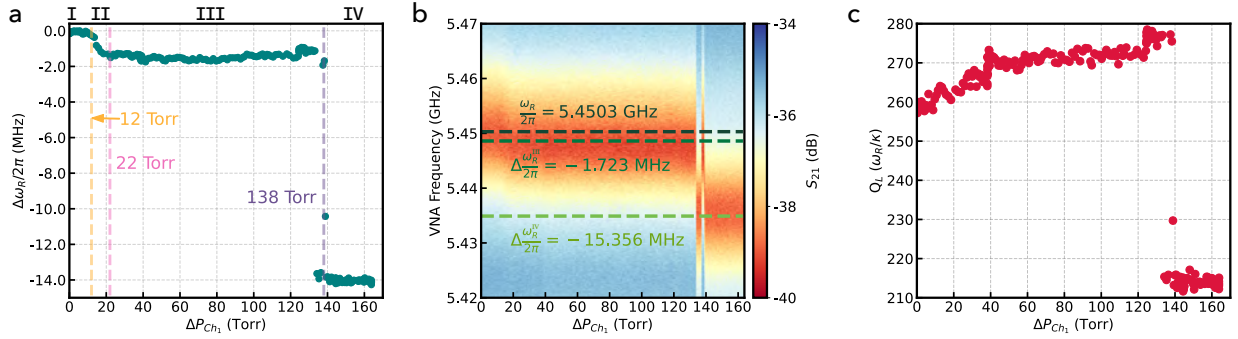


Figure A.5: Helium filling characteristics of the right side resonator ( $\omega_R \simeq 5.45$  GHz). (a) Plot showing the shift in resonator frequency  $\Delta\omega_R/2\pi$  as a function of the pressure difference from the helium tank at room temperature  $\Delta P_{\text{Ch}_1}$ . The four filling regimes corresponding to Fig. A.3 are indicated in Roman numerals. The pressure difference in the helium tank when the resonator shifts into a different filling regime are labeled accordingly. Each resonance frequency was extracted by fitting the spectroscopy data to a Lorentzian distribution. (b) Resonator spectroscopy as a function of the helium tank pressure difference  $\Delta P_{\text{Ch}_1}$  from which the frequency shifts in (a) were extracted from. Dark green dashed line shows the initial resonator frequency  $\omega_R/2\pi = 5.4503$  GHz in the absence of helium and lighter green dashed lines show the two main helium shifted frequencies,  $\Delta\omega_R^{III}/2\pi = -1.723$  MHz, and  $\Delta\omega_R^{IV}/2\pi = -15.356$  MHz. (c) Resonator loaded quality factor  $Q_L$  as a function of helium filling.  $Q_L$  is calculated by extracting the full-width at half-maximum (i.e. the linewidth  $\kappa$ ) from the Lorentzian fit used to extract the points in (a), then the loaded Q-factor is calculated ( $Q_L = \omega/\kappa$ ) for each helium tank pressure dependent spectroscopy measurement.

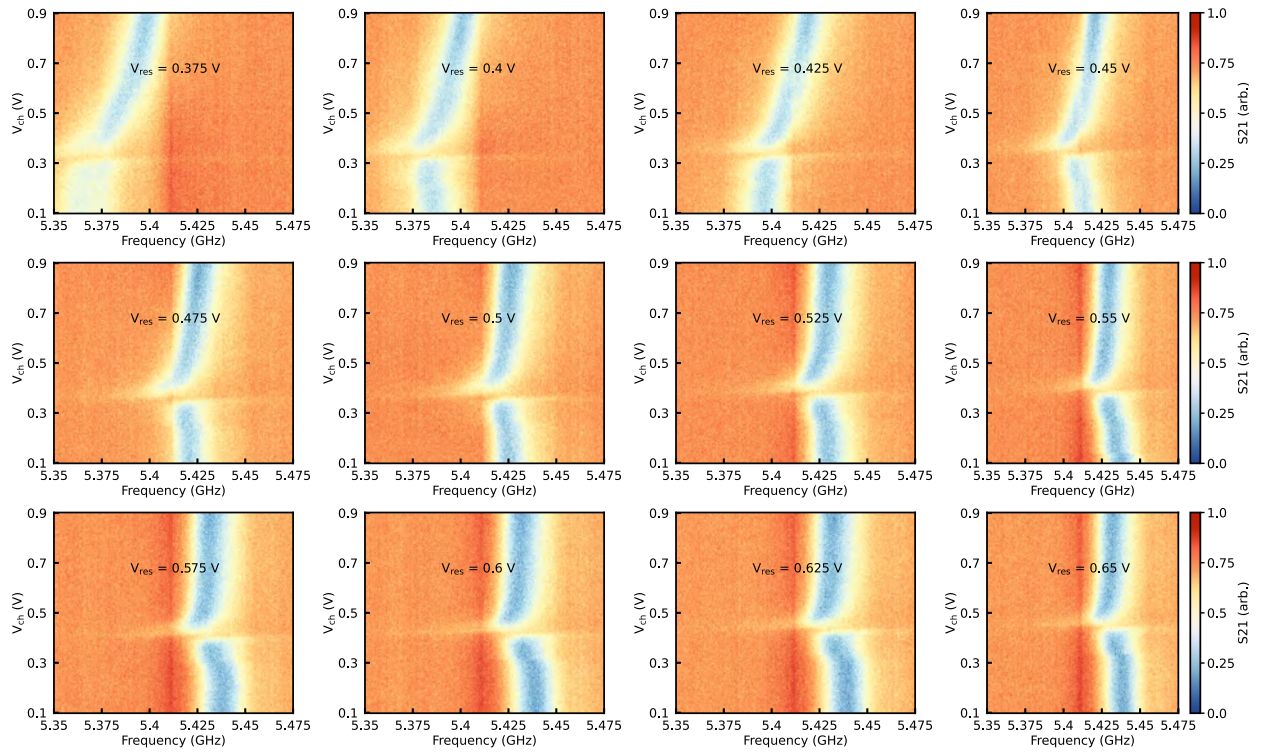


Figure A.6: Resonator spectroscopy measurements as a function of the channel electrode voltage  $V_{ch}$  for varying reservoir electrode voltages  $V_{res}$ . As the reservoir voltage increases, the avoided crossing feature shifts to increased channel voltage, due to the increased chemical potential.

# Appendix B

## Fabricating microchannel devices

The plasmon mode device fabrication discussed in this section corresponds to the particular device from Chapter 3. However, fabrication processes following the one described here can be used to fabricate a variety of similar microchannel device architectures.

### B.1 Silicon chip cleaning protocol

We begin with a pre-cut (1 cm x 1 cm) high resistivity silicon chip and use a standard chip cleaning protocol to remove the S1813 resist used to dice the wafer into their 1 cm<sup>2</sup> chip sizes, as well as any other small particles on the chip surface. This standard chip cleaning protocol is as follows:

1. Coarse clean the pre-cut silicon chips in acetone to remove all photo-resist.
2. Place chips into a slotted PTFE cleaning basket and submerge the basket in a beaker filled with acetone. Put the beaker into a heated ( $\sim 40^{\circ}\text{C}$ ) ultrasonic bath sonicate acetone beaker with chips for 15 minutes.
3. After 15 minutes, clean out the beaker of acetone and replace with fresh acetone. Sonicate chips for 5 - 10 more minutes.
4. After 5 - 10 minutes of sonication, begin removing a single chip at a time to check for any residual gunk on the chips under an optical microscope – to do this, first remove a

single chip from the beaker (leaving the others in the beaker), rinse with fresh acetone, followed by a rinse with IPA, then blow dry with an N2 gun and check for gunk under microscope. If gunk remains, put chip back into position in the slotted basket and check another chip. If no gunk is present, put chip back into basket in a new position. Continue checking until no gunk is visible on any chips.

5. Once all chips are fully cleaned with acetone, remove the beaker from the sonicator and take out slotted cleaning basket with chips. Replace beaker of acetone with beaker of IPA and put the basket with chips into the beaker of IPA. Place beaker back into heated ultrasonic bath for 5 - 10 minutes.
6. Check each chip once again, one by one, to ensure no gunk or imperfections are on the chips – this time removing the chips one by one, rinsing with fresh IPA, blow drying with an N2 gun, and looking at the chip under an optical microscope.
7. Once all chips have been cleaned under sonication and no imperfections are visible under the optical microscope, remove all chips from the PTFE slotted basket, rinse with IPA followed by DI water and blow dry with N2 gun.
8. Finally, put all chips onto aluminum foil tray and torch in the plasma etcher at 300W for 3 minutes.

The chips should now all be free of any gunky imperfections!

## **B.2 Fabrication of plasmon mode device**

Fabrication of the plasmon mode device begins on a 1 cm x 1 cm high resistivity silicon chip, where three devices will be patterned onto in a single fabrication process. At each step of

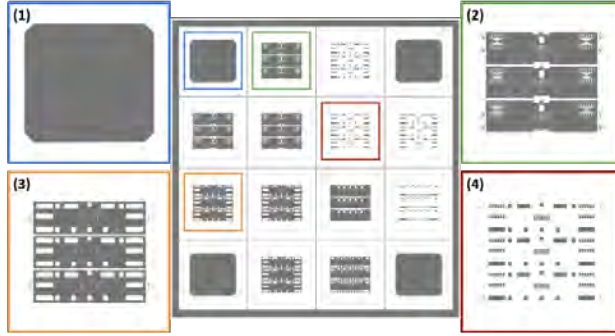


Figure B.1: Photomask associated with the plasmon mode device. Full photomask is in the center with enlarged patterns for each step of photolithography. (1) is the corner mask, (2) is the first electrode layer, (3) is the dielectric hard baking layer, and (4) is the channel structures and top layer electrodes.

fabrication, ensure that no particles have landed on the chip by looking under the optical microscope – if any imperfections are present, the previous step must be redone if possible, or the entire device fabrication must be started over from the beginning if not possible to fix the imperfection from the previous step. The UV lithography steps for this device utilizes the Photo Sciences mask with device name: DeviceD\_141121, as pictured in Fig. B.1.

1. First layer: Bottom electrodes (channel and reservoir electrodes)

- (a) UV lithography I

- i. Place sample on resist spinner, spin sample and blow dry with N<sub>2</sub> gun to ensure a particle-free, clean chip surface
    - ii. Spin coat AZ5214E (~ 5-8 drops should completely cover the surface of chip) at 4000 RPM for 50 seconds
    - iii. Clean off any resist that got on the bottom of the chip with acetone and a ruby stick
    - iv. Bake in the oven at 90°C for 30 minutes (or on the hot place at 100°C for 60 seconds)

- v. Prepare sample on UV lithography stage and expose the corner cleaning mask ((1) in Fig. B.1) for 24 seconds
- vi. Develop in AZ300 MIF for 30 seconds, rinse in beaker of DI water for 15 seconds, blow dry with N2 gun
- vii. Clean off any remaining resist along the edges of the sample that were not removed in the developing process with acetone and a ruby stick

(b) UV lithography II

- i. Place device on UV lithography stage and prepare the bottom electrode mask ((2) in Fig. B.1)
- ii. Expose pattern for 3 seconds
- iii. Bake in the oven at 95° C for 30 minutes
- iv. Let sample cool for a couple minutes, then place back onto stage and do a flood exposure for 24 seconds
- v. Develop in AZ300 MIF for 45 seconds, followed by a rinse in DI water for 15 seconds and blow dry with N2 gun
- vi. Pre-ash in the plasma etcher – 100W for 20 seconds

(c) Thermal evaporation I

- i. Prepare thermal evaporator with titanium and gold for metal deposition
- ii. Pump down thermal evaporator to  $\sim 2 \times 10^{-5}$  Torr, then thermal degass 5 nm of Au followed by 5 nm of Ti
- iii. Wait until chamber pumps down to a base pressure of  $\sim 8 \times 10^{-7}$  Torr (will need to fill cold trap to achieve this pressure)
- iv. Evaporate first 3.5 nm of Ti, followed by 40 nm of Au.

(d) Lift-off I

- i. Begin lift-off of sample in a beaker of PG remover on a 100° C hotplate for ~ 20 minutes
- ii. In the meantime, place a second beaker of PG remover (without samples) on the 100° C hotplate
- iii. After 20 minutes, put samples into the second beaker of 100° C PG remover and gently sonicate to remove any excess metal (if necessary upon inspection under microscope)
- iv. Rinse in IPA for ~ 15 seconds to clean PG remover from device and blow dry with N2 gun
- v. Torch in plasma etcher – 300W for 300 seconds

(e) Electron beam lithography I

- i. Spin coat PMMAC2 resist at 4000 RPM for 40 seconds
- ii. Clean off the bottom of the sample of any resist with acetone and a ruby stick
- iii. Bake on hotplate at 180° C for 8 minutes
- iv. Prepare sample in EBL
- v. Set the magnification to x400 and first write the align design file:  
"MCH\_11\_single\_ALIGN.dc2"
- vi. Once aligned, run the "MCH\_11\_single\_EBEAM.dc2" file to write the microchannel electrodes
- vii. Develop pattern in a 1:3 solution of MIBK:IPA for 50 seconds, followed by rinsing in IPA for 15 seconds and blow drying with N2 gun
- viii. Pre-ash in plasma etcher at 100W for 35 seconds

(f) Thermal evaporation II

- i. Prepare the thermal evaporator and follow steps (i) - (iii) in "Thermal evaporation I"
- ii. Evaporate 4 nm Ti, followed by 50 nm Au

(g) Lift-off II

- i. Prepare beaker of acetone (with an aluminum foil lid to prevent evaporation) on a 60° C hot plate
- ii. Place samples warm acetone for at least 30 minutes, then can remove from the hot plate and leave for lift-off overnight
- iii. Inspect samples under microscope to ensure all metal has lifted off – gently sonicate if not
- iv. Once all metal lifted off, rinse in IPA and blow dry with N<sub>2</sub>
- v. Torch in plasma etcher – 300W for 150 seconds

2. Second layer: Microchannel structures created with hardbaked resist

(a) UV lithography III and hard bake

- i. Spin coat S1813 resist at 4000 RPM for 60 seconds
- ii. Bake on the hot plate at 110° C for 120 seconds
- iii. Place sample on UV lithography stage and prepare the dielectric openings pattern ((3) in Fig. B.1)
- iv. Expose pattern for 8 seconds
- v. Develop in MF319 for 30 seconds, rinse in DI water for 15 seconds, then blow dry with N<sub>2</sub>

- vi. Clean around the edges of sample to get rid of residual resist with acetone and a ruby stick
  - vii. Pre-ash in plasma etcher – 100W for 60 seconds
  - viii. Place samples on the already 110° C hot plate and increase the temperature to 200° C. Bake for 1 hour and 50 minutes
  - ix. Let samples cool for at least an hour after baking
3. Third layer: Top layer electrodes (guard electrode, gate electrode, and ground plane)
- (a) UV lithography IV
    - i. Spin coat AZ5214E resist at 4000 RPM for 45 seconds
    - ii. Bake on the hotplate at 100° C for 60 seconds
    - iii. Expose the corner mask ((1) in Fig. B.1) for 24 seconds
    - iv. Develop in AZ300 MIF for 30 seconds followed by a rinse in DI water 15 seconds
    - v. Clean edges of device with acetone and a ruby stick
  - (b) UV lithography V
    - i. Place sample on UV lithography stage and ensure the sample is as flat and level as possible
    - ii. Using the top layer electrode mask ((4) in Fig. B.1), align the mask utilizing all the alignment marks around the edges
    - iii. Expose the pattern for 3 seconds
    - iv. Bake on the hotplate at 120° C for 90 seconds
    - v. Do a flood exposure of the entire sample for 24 seconds

- vi. Develop in AZ300 MIF for 50 seconds followed by DI water for 15 seconds
  - vii. Clean edges of any residual resist with acetone and a ruby stick
  - viii. Pre-ash in plasma etcher – 100W for 20 seconds
- (c) Thermal evaporation III
- i. Prepare the thermal evaporator and follow steps (i) - (iii) in "Thermal evaporation I"
  - ii. Evaporate 5 nm Ti, followed by 60 nm Au
- (d) Lift-off III
- i. Prepare a beaker of PG remover on a hotplate at 100° C
  - ii. Place sample in hot PG remover for ~ 25 minutes and then inspect
  - iii. Once lift-off complete, rinse in IPA and blow dry with N2
- (e) Torching dielectric layer
- i. Place samples into plasma etcher and torch at 300W for at least 300 seconds
  - ii. Keep an eye on the device through the window (a flashlight angled at the right hand corner window above the device is usually a good angle) and watch for the interference pattern indicating the dielectric layer is being torched away. This typically takes between 400 seconds - 600 seconds.
  - iii. As soon as you see the last bit of dielectric get torched away, wait 20 more seconds and then turn off the plasma etcher
  - iv. Inspect device under microscope to ensure excess dielectric layer has been removed and you are left with open channels in the reservoirs – if not, torch for longer

# Appendix C

## Finite element modeling calculations for devices

Finite element modeling (FEM) simulations are a useful tool to parameterize the microchannel device. In these simulations, we can model how the electron system capacitively couples to the surrounding electrodes, find the effective width of the electron system for a given confinement, and calculate the electron densities in the central microchannel for a given electrostatic potential profiles. In the modeling of the microchannel devices throughout this thesis, we have mainly utilized FreeFem++ [207] for FEM calculations and Gmsh [208] for building and visualizing the geometry. We have also used ZeroHeliumKit [209], which utilizes both FreeFem++ and Gmsh. For modeling the superconducting coplanar waveguide resonators, COMSOL Multiphysics was used.

### C.1 FEM for microchannel devices

For both devices discussed in this thesis, the following device modeling procedure holds for finding the various device parameters. Here we discuss two different methods for approaching how one can calculate the electron density in the microchannel. In the first method, we build the full three-dimensional geometry of the device, where we calculate the capacitive coupling constants,  $\alpha(x, y)$ , at each coordinate in the device, and from this we can estimate a quasi-1D

electron density, where

$$n_s^{\text{q1D}} = \frac{\varepsilon_0 \varepsilon_{\text{He}}}{ed} \left( \sum_i \alpha_i(x, y) V_i - \phi_e \right), \quad (\text{C.1})$$

or an estimate of the 2D electron density from

$$n_s^{\text{2D}} = \frac{\varepsilon_0 \varepsilon_{\text{He}}}{ed} (V_{\text{ch}} - \phi_e). \quad (\text{C.2})$$

Here, the chemical potential  $\phi_e = \alpha_{\text{ch}}^0 V_{\text{ch}}^{\text{th}}$ , with  $\alpha_{\text{ch}}^0$  the capacitive coupling constant to the channel electrode in the center of the central microchannel, calculated in FEM.

In the second method, we use the two-dimensional  $(y, z)$ -cross section along the center of the channel ( $x = 0$ ), and self-consistently solve the Poisson equation to obtain a two-dimensional electron sheet width across the channel ( $w_e$ ) as a function of a varying channel electrode voltage  $V_{\text{ch}}$ .

## C.2 Method 1: FEM calculation of coupling constants,

$$\alpha(x, y)$$

This method begins with a DXF file containing the parts of the device to be modeled. In Gmsh, the device electrodes get assigned to physical surface identifiers, and the chip below, helium within the channels, and vacuum above get assigned to physical volume identifiers. Then, the electrostatic Laplace equation in the weak form is solved,

$$\varepsilon \int_{Th} (\nabla u \cdot \nabla v) dV. \quad (\text{C.3})$$

Here,  $u$  is the unknown function that we are trying to solve for and  $v$  is the test function used in the weak formulation, and we solve this iteratively at each point in space for each electrode. In this type of FEM, we use the three-dimensional(3D) quadratic-element space (P2 polynomials in 3D) on the mesh  $\mathcal{T}_h$  [207].

### C.3 Method 2: FEM calculation of densities, $n_s$ , using the microchannel device cross section

This method begins with using a cross section across the center of the central microchannel (see Fig. 3.3 for example). In order to self-consistently solve for the electron sheet width, we calculate the electrostatic force  $F = -e \frac{\partial \phi}{\partial y}$  acting on the edges of the electron sheet, such that at the equilibrium configuration,  $F = 0$ . This will give the effective electron sheet width  $w_e$ .

To solve for the electron areal density, we solve for the potential above and below the electron sheet,

$$\left. \frac{\partial \phi}{\partial z} \right|_{\text{above}} - \varepsilon_{\text{He}} \left. \frac{\partial \phi}{\partial z} \right|_{\text{below}} = -\frac{en_s}{\varepsilon_0}, \quad (\text{C.4})$$

where the integral for the linear density  $n_l$

$$n_l = \int_{-w_e/2}^{w_e/2} n_s(y) dy \quad (\text{C.5})$$

is used to calculate the number of electron rows  $N_y = \sqrt{w_e n_l}$  for a given confinement [86].

# Bibliography

1. Sommer, W. T. Liquid Helium as a Barrier to Electrons. *Physical Review Letters* **12**, 271 (1964).
2. Woolf, M. A. & Rayfield, G. Energy of Negative Ions in Liquid Helium by Photoelectric Injection. *Physical Review Letters* **15**, 235 (1965).
3. Cole, M. W. & Cohen, M. H. Image-Potential-Induced Surface Bands in Insulators. *Physical Review Letters* **23**, 1238 (1969).
4. Shikin, V. Motion of Helium Ions near a Vapor-liquid Surface. *Soviet Physics JETP* **31**, 936. <http://jetp.ras.ru/cgi-bin/e/index/e/31/5/p936?a=list> (1970).
5. Crandall, R. & Williams, R. Crystallization of electrons on the surface of liquid helium. *Physics Letters A* **34**, 404 (1971).
6. Wigner, E. On the Interaction of Electrons in Metals. *Physical Review* **46**, 1002 (1934).
7. Grimes, C. & Adams, G. Evidence for Liquid-to-Crystal Phase Transition in a Classical Two-Dimensional Sheet of Electrons. *Physical Review Letters* **42**, 795 (1979).
8. Xu, Y.-Z. *et al.* Controlled melting of a Wigner ion crystal with atomic resolution. *Physical Review A* **102**, 063121 (6 2020).
9. Matthiesen, C., Yu, Q., Guo, J., Alonso, A. M. & Häffner, H. Trapping Electrons in a Room-Temperature Microwave Paul Trap. *Phys. Rev. X* **11**, 011019 (1 2021).
10. Dykman, M. I., Fang-Yen, C. & Lea, M. J. Many-electron transport in strongly correlated nondegenerate two-dimensional electron systems. *Physical Review B* **55**, 16249–16271 (24 1997).
11. Rees, D. G., Beysengulov, N. R., Lin, J.-J. & Kono, K. Stick-slip motion of the wigner solid on liquid helium. *Phys. Rev. Lett* **116**, 206801 (2016).
12. Dykman, M. I., Kono, K., Konstantinov, D. & Lea, M. J. Ripplonic Lamb Shift for Electrons on Liquid Helium. *Physical Review Letters* **119**, 256802 (25 2017).
13. Rees, D. G. *et al.* Point-Contact Transport Properties of Strongly Correlated Electrons on Liquid Helium. *Physical Review Letters* **106**, 026803 (2011).
14. Bradbury, F. R. *et al.* Efficient Clocked Electron Transfer on Superfluid Helium. *Physical Review Letters* **107**, 266803 (2011).
15. *The Nobel Prize in Physics 1913* NobelPrize.org. <https://www.nobelprize.org/prizes/physics/1913/summary/>.

16. Kapitza, P. Viscosity of Liquid Helium below the  $\lambda$ -Point. *Nature* **141**, 74 (1938).
17. Allen, J. & Misener, A. Flow Phenomena in Liquid Helium II. *Nature* **142**, 643–644 (1938).
18. Annett, J. F. *Superconductivity, Superfluids and Condensates* (Oxford University Press, 2004).
19. Platzman, P. & Fukuyama, H. Phase diagram of the two-dimensional electron liquid. *Physical Review B* **10**, 3150 (1974).
20. Peeters, F. M. & Platzman, P. M. Electrons on Films of Helium: A Quantum Mechanical Two-Dimensional Fermion System. *Physical Review Letters* **50**, 2021–2023 (1983).
21. Mehrotra, R., Guo, C. J., Ruan, Y. Z., Mast, D. B. & Dahm, A. J. Density-dependent mobility of a two-dimensional electron fluid. *Physical Review B* **29**, 5239 (1984).
22. Stan, M. & Dahm, A. Two-dimensional melting: Electrons on helium. *Physical Review B* **40**, 8995–9005 (1989).
23. Cândido, L., Rino, J. P. & Studart, N. Melting of classical two-dimensional electrons on a helium film: A molecular-dynamics study. *Physical Review B* **54**, 7046–7051 (1996).
24. Lea, M. J. *et al.* Magnetoconductivity of two-dimensional electrons on liquid helium: Experiments in the fluid phase. *Physical Review B* **55**, 16280 (1997).
25. Rees, D. G., Ikegami, H. & Kono, K. Reentrant Melting of a Classical Quasi-One-Dimensional Wigner Crystal on the Surface of Liquid Helium. *Journal of the Physical Society of Japan* **82**, 124602 (2013).
26. Monarkha, Y. P. & Shikin, V. Theory of a two-dimensional Wigner crystal of surface electrons in helium. *Soviet Physics JETP, Vol. 41, No.4 (Zh. Eksp. Teor. Fiz)* **41 (68)**, 1423–1433 (1975).
27. Shirahama, K. & Kono, K. Dynamical Transition in the Wigner Solid on a Liquid Helium Surface. *Physical Review Letters* **74**, 781–784 (1995).
28. Ikegami, H., Akimoto, H. & Kono, K. Nonlinear Transport of the Wigner Solid on Superfluid  $^4\text{He}$  in a Channel Geometry. *Physical Review Letters* **102**, 046807 (2009).
29. Monarkha, Y. P. & Syvokon, V. A two-dimensional Wigner crystal (Review Article). *Low Temperature Physics* **38**, 1067 (2012).
30. Glattli, D. C., Andrei, E. Y., Deville, G., Poitrenaud, J. & Williams, F. I. B. Dynamical Hall Effect in a Two-Dimensional Classical Plasma. *Physical Review Letters* **54**, 1710–1713 (1985).
31. Van der Heijden, R., Gijsman, H. & Peeters, F. The high-field Hall effect and magnetoresistance of electrons on helium. *Journal of Physics C: Solid State Physics* **21**, L1165 (1988).
32. Lea, M., Stone, A. & Fozooni, P. The Hall Effect in 2D Electrons on Liquid Helium. *Europhysics Letters* **7**, 641 (1988).

33. Peters, P., Scheuzger, P., Lea, M., Jacobs, W. & van der Heijden, R. The AC Hall effect for electrons on liquid helium in ultra-high magnetic fields. *Surface Science* **305**, 674–677. ISSN: 0039-6028 (1994).
34. Grimes, C. & Adams, G. Observation of Two-dimensional Plasmons and Electron-Ripplon Scattering in a Sheet of Electrons on Liquid Helium. *Physical Review Letters* **36** (1976).
35. Mast, D. B., Dahm, A. J. & Fetter, A. L. Observation of Bulk and Edge Magnetoplasmons in a Two-Dimensional Electron Fluid. *Physical Review Letters* **54**, 1706–1709 (1985).
36. Sivokon', V., Dotsenko, V., Kovdrya, Y. & Grigor'ev, V. 2D Wigner Solid over Liquid Helium: Resonant and Non-Linear Phenomena. *Journal of Low Temperature Physics* **111**, 609–614 (1998).
37. Chen, J., Zadorozhko, A. A. & Konstantinov, D. Strong coupling of a two-dimensional electron ensemble to a single-mode cavity resonator. *Physical Review B* **98**, 235418 (23 2018).
38. Kawakami, E., Elarabi, A. & Konstantinov, D. Relaxation of the Excited Rydberg States of Surface Electrons on Liquid Helium. *Physical Review Letters* **126**, 106802 (2021).
39. Yang, G. *et al.* Coupling an Ensemble of Electrons on Superfluid Helium to a Superconducting Circuit. *Physical Review X* **6**, 011031 (2016).
40. Chepelianskii, A. D., Papoular, D., Konstantinov, D., Bouchiat, H. & Kono, K. Coupled pair of one- and two-dimensional magnetoplasmons on electrons on helium. *Physical Review B* **103**, 075420 (2021).
41. Yunusova, K. M., Konstantinov, D., Bouchiat, H. & Chepelianskii, A. D. Coupling between Rydberg States and Landau Levels of Electrons Trapped on Liquid Helium. *Physical Review Letters* **122**, 176802 (2019).
42. Zadorozhko, A., Chen, J., Chepelianskii, A. & Konstantinov, D. Motional quantum states of surface electrons on liquid helium in a tilted magnetic field. *Physical Review B* **103**, 054507 (2021).
43. Byeon, H. *et al.* Piezoacoustics for precision control of electrons floating on helium. *Nature Communications* **12**, 4150 (2021).
44. Abdurakhimov, L., Yamashiro, R., Badrutdinov, A. & Konstantinov, D. Strong coupling of the cyclotron motion of surface electrons on liquid Helium to a microwave cavity. *Physical Review Letters* **117**, 056803 (2016).
45. Shirahama, K., Ito, S., Suto, H. & Kono, K. Surface study of liquid  $^3\text{He}$  using surface state electrons. *Journal of Low Temperature Physics* **101**, 439–444 (1995).
46. Esel'son, B., Rybalko, A. & Sokolov, S. Investigation of the surface electron mobility in liquid  $\text{He}^4$  and weak solutions of  $\text{He}^3$  in  $\text{He}^4$ . *Soviet Journal of Low Temperature Physics* **6**, 544 (1980).

47. Grimes, C., Brown, T., Burns, M. L. & Zipfel, C. Spectroscopy of electrons in image-potential-induced surface states outside liquid helium. *Physical Review B* **13**, 140 (1976).
48. Saitoh, M. Warm Electrons on the Liquid  $^4\text{He}$  Surface. *Journal of the Physical Society of Japan* **42**, 201–209 (1977).
49. Monarkha, Y. & Kono, K. *Two-Dimensional Coulomb Liquids and Solids* (Springer, 2004).
50. Zou, S. & Konstantinov, D. Image-charge detection of the Rydberg transition of electrons on superfluid helium confined in a microchannel structure. *New Journal of Physics* **24**, 103026 (2022).
51. Sarma, M. S. *Introduction to Electrical Engineering* 371–378 (Oxford University Press, 2001).
52. Nasyedkin, K. *et al.* Unconventional field-effect transistor composed of electrons floating on liquid helium. *Journal of Physics: Condensed Matter* **30**, 465501 (2018).
53. Sommer, W. & Tanner, D. Mobility of Electrons on the Surface of Liquid  $^4\text{He}$ . *Physical Review Letters* **27**, 1345–1349 (1971).
54. Andrei, E. Y. *Two-Dimensional Electron Systems on Helium and Other Cryogenic Substrates* (Kluwer Academic Publishers, 1997).
55. Deville, G., Valdes, A., Andrei, E. Y. & Williams, F. I. B. Propagation of Shear in a Two-Dimensional Electron Solid. *Physical Review Letters* **53**, 588–591 (1984).
56. Chepelianskii, A. D., Watanabe, M., Nasyedkin, K., Kono, K. & Konstantinov, D. An incompressible state of a photo-excited electron gas. *Nature Communications* **6**, 7210 (2015).
57. Fisher, D. S., Halperin, B. I. & Platzman, P. M. Phonon-Ripplon Coupling and the Two-Dimensional Electron Solid on a Liquid-Helium Surface. *Physical Review Letters* **42**, 798–801 (1979).
58. Sivokon', V. E., Dotsenko, V. V. & Kovdrya, Y. Z. Nonlinear phenomena in phonon-ripplon oscillations in a two-dimensional electron crystal over liquid helium. *Low Temperature Physics* **27**, 83–87 (2001).
59. Monarkha, Y. P., Sokolov, S. S., Hai, G.-Q. & Studart, N. Magnetoresistance of non-degenerate quantum electron channels formed on the surface of superfluid helium. *Physical Review B* **69**, 104525 (2004).
60. Konstantinov, D. & Kono, K. Novel Radiation-Induced Magnetoresistance Oscillations in a Nondegenerate Two-Dimensional Electron System on Liquid Helium. *Physical Review Letters* **103**, 266808 (2009).
61. Goksu, M. I., Kim, M., Mantey, K. A. & Dahm, A. J. Edge magnetoplasmons in a partially screened two-dimensional electron gas on a helium surface. *Physical Review B* **75**, 115323 (2007).
62. Fetter, A. L. Electrodynamics of a Layered Electron Gas. I. Single Layer. *Annals of Physics* **81**, 367–393 (1973).

63. Jackson, J. D. *Classical Electrodynamics (3rd ed.)* (John Wiley Sons, 1999).
64. Zou, S., Konstantinov, D. & Rees, D. G. Dynamical ordering in a two-dimensional electron crystal confined in a narrow channel geometry. *Phys. Rev. B* **104**, 045427 (4 July 2021).
65. Glasson, P. *et al.* Observation of Dynamical Ordering in a Confined Wigner Crystal. *Physical Review Letters* **87**, 176802 (2001).
66. Rees, D. G. *et al.* Structural order and melting of a quasi-one-dimensional electron system. *Physical Review B* **94**, 045139 (2016).
67. Konstantinov, D. *et al.* Microwave-absorption-induced heating of surface state electrons on liquid  $^3\text{He}$ . *J. Phys. Soc. Jpn* **77**, 034705 (2008).
68. Nasyedkin, K., Syvokon, V. & Monarkha, Y. Transport Properties of the Two-Dimensional Wigner Solid on Liquid Helium in the Presence of a High-Frequency Damaging Electric Field. *J. Low Temp. Phys* **163**, 148–163 (2011).
69. Chung, Y. J. *et al.* Understanding limits to mobility in ultrahigh-mobility GaAs two-dimensional electron systems: 100 million  $\text{cm}^2/\text{Vs}$  and beyond. *Physical Review B* **106**, 075134 (2022).
70. Ashcroft, N. & Mermin, N. D. *Solid State Physics* (Saunders College Publishing, 1976).
71. Mehrotra, R., Guenin, B. M. & Dahm, A. J. Ripplon-Limited Mobility of a Two-Dimensional Crystal of Electrons: Experiment. *Physical Review Letters* **48**, 641 (1982).
72. Jones, R. C., Williams, A. J. E., Vinen, W. F. & Ewbank, P. A. The lifetime of interacting ripplons on the surface of superfluid helium. *Journal of Low Temperature Physics* **92**, 239–261 (1993).
73. Platzman, P. & Dykman, M. Quantum Computing with Electrons Floating on Liquid Helium. *Science* **284**, 1967–1969 (1999).
74. Dykman, M. I., Platzman, P. M. & Seddighrad, P. Qubits with electrons on liquid helium. *Phys. Rev. B* **67**, 155402. <https://link.aps.org/doi/10.1103/PhysRevB.67.155402> (15 Apr. 2003).
75. Moskovtsev, K. *Nonlinear dynamics of coupled electron-vibrational systems* PhD thesis (Michigan State University, 2018).
76. Friend, J. N. Latent Heat of Evaporation of Liquid Helium. *Nature* **139**, 472–473 (1937).
77. Crandall, R. S. Non-Ohmic Electron Transport on Liquid Helium. *Physical Review A* **6** (1972).
78. Shikin, V. Some properties of surface electrons in liquid helium. *Soviet Physics JETP* **33**, 387 (1971).
79. Mehrotra, R. & Dahm, A. Analysis of the Sommer technique for measurement of the mobility for charges in two dimensions. *Journal of Low Temperature Physics* **67**, 115 (1987).

80. Karakash, J. J. *Transmission Lines And Filter Networks* (The Macmillan Company, New York, 1950).
81. Dykman, M. I. & Rubo, Y. G. Bragg-Cherenkov Scattering and Nonlinear Conductivity of a Two-Dimensional Wigner Crystal. *Physical Review Letters* **78**, 4813–4816 (1997).
82. Giannetta, R. & Wilen, L. Nonequilibrium melting of the two dimensional electron crystal. *Solid State Communications* **78**, 199–203 (1991).
83. Vinen, W. Non-linear electrical conductivity and sliding in a two-dimensional electron crystal on liquid helium. *Journal of Physics: Condensed Matter* **11**, 9709 (1999).
84. Kristensen, A. *et al.* Hall-Velocity Limited Magnetoconductivity in a Classical Two-Dimensional Wigner Crystal. *Physical Review Letters* **77**, 1350–1353 (1996).
85. Rees, D. G., Totsuji, H. & Kono, K. Commensurability-Dependent Transport of a Wigner Crystal in a Nanoconstriction. *Physical Review Letters* **108**, 176801 (2012).
86. Beysengulov, N. R. *et al.* Structural Transitions in a Quasi-1D Wigner Solid on Liquid Helium. *Journal of Low Temperature Physics* **182**, 28–37 (2016).
87. Badrutdinov, A. O., Smorodin, A. V., Rees, D. G., Lin, J. Y. & Konstantinov, D. Non-linear transport of the inhomogeneous Wigner solid in a channel geometry. *Physical Review B* **94**, 195311 (2016).
88. Lin, J.-Y., Smorodin, A. V., Badrutdinov, A. O. & Konstantinov, D. Sliding of an electron crystal of finite size on the surface of superfluid  $^4\text{He}$  confined in a microchannel. *Physical Review B* **98**, 085412 (2018).
89. Monarkha, Y. P. Bragg–Cherenkov resonance and polaron-like decoupling of the Wigner solid on superfluid helium. *Low Temperature Physics* **48**, 612–620 (2022).
90. Marty, D. Stability of two-dimensional electrons on a fractionated helium surface. *Journal of Physics C: Solid State Physics* **19**, 6097 (1986).
91. Glasson, P. *et al.* Microelectronics on liquid helium. *Physica B: Condensed Matter* **284-288**, 1916–1917 (2000).
92. Sokolov, S. S., Hai, G.-Q. & Studart, N. Mobility of electrons in a quasi-one-dimensional conducting channel on the liquid-helium surface. *Physical Review B* **51**, 5977–5988 (1995).
93. Glasson, P. *et al.* Confined electron crystals and Rydberg states on liquid helium. *Physica E: Low-dimensional Systems and Nanostructures* **22**, 761–766 (2004).
94. Pobell, F. *Matter and Methods at Low Temperatures* ISBN: 978-3-540-46356-6 (Springer Berlin, Heidelberg, 2007).
95. Dzyaloshinskii, I. E., Lifshitz, E. M. & Pitaevskii, L. P. The general theory of van der Waals forces. *Advances in Physics* **10**, 165–209 (1961).
96. Donnelly, R. J. & Barenghi, C. F. The Observed Properties of Liquid Helium at the Saturated Vapor Pressure. *Journal of Physical and Chemical Reference Data* **27**, 1217–1274 (1998).

97. Mima, K. & Ikezi, H. Propagation of nonlinear waves on an electron-charged surface of liquid helium. *Phys. Rev. B* **17**, 3567–3575 (1978).
98. Ikezi, H. & Platzman, P. M. Stability of helium films charged with electrons. *Phys. Rev. B* **23**, 1145–1148 (1981).
99. Roche, P., Deville, G., Keshishev, K. O., Appleyard, N. J. & Williams, F. I. B. Low Damping of Micron Capillary Waves on Superfluid  $^4\text{He}$ . *Physical Review Letters* **75**, 3316–3319 (1995).
100. Chernikova, D. Properties of a self-localized charged layer on the surface of liquid helium. *Zh. Eksp. Teor. Fiz* **68**, 249 (1975).
101. Spangler, G. & Hereford, F. Injection of electrons into He II from an immersed tungsten filament. *Physical Review Letters* **20**, 1229 (1968).
102. Lin, J.-Y., Smorodin, A., Badrutdinov, A. & Konstantinov, D. Transport Properties of a Quasi-1D Wigner Solid on Liquid Helium Confined in a Microchannel with Periodic Potential. *Journal of Low Temperature Physics* **195**, 289 (2018).
103. Sabouret, G., Bradbury, F. R., Shankar, S., Bert, J. A. & Lyon, S. A. Signal and charge transfer efficiency of few electrons clocked on microscopic superfluid helium channels. *Applied Physics Letters* **92**, 082104 (2008).
104. Koolstra, G., Yang, G. & Schuster, D. I. Coupling a single electron on superfluid helium to a superconducting resonator. *Nature Communications* **10**, 5323 (2019).
105. Feynman, R. P. Simulating physics with computers. *International Journal of Theoretical Physics* **21**, 467–488 (1982).
106. Collin, E. *et al.* Microwave Saturation of the Rydberg States of Electrons on Helium. *Physical Review Letters* **89**, 245301 (2002).
107. Kawakami, E., Elarabi, A. & Konstantinov, D. Image-Charge Detection of the Rydberg States of Surface Electrons on Liquid Helium. *Physical Review Letters* **123**, 086801 (2019).
108. Kawakami, E., Chen, J., Benito, M. & Konstantinov, D. Blueprint for quantum computing using electrons on helium. *Physical Review Applied* **20**, 054022 (2023).
109. Belianchikov, M., Kraus, J. & Konstantinov, D. Cryogenic Resonant Amplifier for Electron-on-Helium Image Charge Readout. *Journal of Low Temperature Physics* **215**, 312–323 (2024).
110. Lyon, S. A. Spin-based quantum computing using electrons on liquid helium. *Physical Review A* **74**, 052338 (2006).
111. Schuster, D., Fragner, A., Dykman, M., Lyon, S. & Schoelkopf, R. Proposal for Manipulating and Detecting Spin and Orbital States of Trapped Electrons on Helium Using Cavity Quantum Electrodynamics. *Physical Review Letters* **105**, 040503 (2010).
112. Blais, A., Grimsmo, A. L., Girvin, S. & Wallraff, A. Circuit quantum electrodynamics. *Rev. Mod. Phys.* **93**, 025005 (2 May 2021).
113. Castoria, K. *et al.* Sensing and Control of Single Trapped Electrons Above 1 Kelvin. *arXiv preprint*. arXiv: [arXiv:2412.03404](https://arxiv.org/abs/2412.03404) (2024).

114. Koolstra, G. *et al.* High-impedance resonators for strong coupling to an electron on helium. *arXiv preprint*. arXiv: [arXiv:2410.19592](https://arxiv.org/abs/2410.19592) (2024).
115. Zhou, X. *et al.* Single electrons on solid neon as a solid-state qubit platform. *Nature* **605**, 46–50 (2022).
116. Zhou, X. *et al.* Electron charge qubit with 0.1 millisecond coherence time. *Nature Physics* **20**, 116–122 (2024).
117. Lea, M., Frayne, P. & Mukharsky, Y. Could we quantum compute with electrons on helium? *Fortschritte der Physik* **48**, 1109–1124 (2000).
118. Averin, D. V. & Likharev, K. K. Coulomb blockade of single-electron tunneling, and coherent oscillations in small tunnel junctions. *Journal of Low Temperature Physics* **62**, 345–373 (1986).
119. Papageorgiou, G. *et al.* Detecting electrons on helium with a single-electron transistor (SET). *Physica E: Low-dimensional Systems and Nanostructures* **18**, 179–181 (2003).
120. Papageorgiou, G. *et al.* Counting Individual Trapped Electrons on Liquid Helium. *Applied Physics Letters* **86**, 153106 (2005).
121. Phillips, W. A. Two-level states in glasses. *Reports on Progress in Physics* **50**, 1657 (1987).
122. Paladino, E., Galperin, Y., Falci, G. & Altshuler, B. 1/f noise: Implications for solid-state quantum information. *Reviews of Modern Physics* **86**, 361–418 (2014).
123. Phillips, W. A. Tunneling states in amorphous solids. *Journal of low temperature physics* **7**, 351–360 (1972).
124. Martinis, J. M. *et al.* Decoherence in Josephson Qubits from Dielectric Loss. *Physical Review Letters* **95**, 210503 (2005).
125. Müller, C., Cole, J. H. & Lisenfeld, J. Towards understanding two-level-systems in amorphous solids: insights from quantum circuits. *Reports on Progress in Physics* **82**, 124501 (2019).
126. Klimov, P. V. *et al.* Fluctuations of Energy-Relaxation Times in Superconducting Qubits. *Physical Review Letters* **121**, 090502 (2018).
127. Burnett, J. *et al.* Decoherence benchmarking of superconducting qubits. *npj Quantum Information* **5** (54 2019).
128. Schlör, S. *et al.* Correlating Decoherence in Transmon Qubits: Low Frequency Noise by Single Fluctuators. *Physical Review Letters* **123**, 190502 (2019).
129. Carroll, M., Rosenblatt, S., Jurcevic, P., Lauer, I. & Kandala, A. Dynamics of superconducting qubit relaxation times. *npj Quantum Information* **8** (132 2022).
130. Beysengulov, N. R. *et al.* Noise Performance and Thermalization of a Single Electron Transistor using Quantum Fluids. *Journal of Low Temperature Physics* **205**, 143–154 (2021).
131. Amelio, G. F., Tompsett, M. F. & Smith, G. E. Experimental verification of the charge coupled device concept. *Bell System Technical Journal* **49**, 593–600 (1970).

132. Boyle, W. S. & Smith, G. E. Charge coupled semiconductor devices. *Bell System Technical Journal* **49**, 587–593 (1970).
133. Sabouret, G. & Lyon, S. Measurement of the charge transfer efficiency of electrons clocked on superfluid helium. *Applied Physics Letters* **88**, 254105 (2006).
134. Takita, M. *et al.* Spatial distribution of electrons on a superfluid helium charge-coupled device. *Journal of Physics: Conference Series* **400**, 042059 (2012).
135. Takita, M. & Lyon, S. A. Isolating electrons on superfluid helium. *Journal of Physics: Conference Series* **568**, 052034 (2014).
136. Feldman, M. *et al.* Sensing Few Electrons Floating on Helium with High-Electron-Mobility Transistors. *Journal of Low Temperature Physics* (2025).
137. Blais, A., Huang, R.-S., Wallraff, A., Girvin, S. M. & Schoelkopf, R. J. Cavity quantum electrodynamics for superconducting electrical circuits: An architecture for quantum computation. *Physical Review A* **69**, 062320 (6 June 2004).
138. Petersson, K. *et al.* Circuit quantum electrodynamics with a spin qubit. *Nature* **490**, 380–383 (Oct. 2012).
139. LaHaye, M., Suh, J., Echternach, P., Schwab, K. C. & Roukes, M. L. Nanomechanical measurements of a superconducting qubit. *Nature* **459**, 960–964 (2009).
140. O’Connell, A. D. *et al.* Quantum ground state and single-phonon control of a mechanical resonator. *Nature* **464**, 697–703 (2010).
141. Pirkkalainen, J. *et al.* Hybrid circuit cavity quantum electrodynamics with a micromechanical resonator. *Nature* **494**, 211–215 (Feb. 2013).
142. Clerk, A., Lehnert, K., Bertet, P., Petta, J. & Nakamura, Y. Hybrid quantum systems with circuit quantum electrodynamics. *Nature Physics* **16**, 257–267 (2020).
143. Goryachev, M. *et al.* High-cooperativity cavity QED with magnons at microwave frequencies. *Physical Review Applied* **2**, 054002 (2014).
144. Tabuchi, Y. *et al.* Hybridizing ferromagnetic magnons and microwave photons in the quantum limit. *Physical Review Letters* **113**, 083603 (2014).
145. Tabuchi, Y. *et al.* Coherent coupling between a ferromagnetic magnon and a superconducting qubit. *Science* **349**, 405–408 (2015).
146. Li, J., Zhu, S.-Y. & Agarwal, G. Magnon-photon-phonon entanglement in cavity magnomechanics. *Physical Review Letters* **121**, 203601 (2018).
147. Lachance-Quirion, D. *et al.* Entanglement-based single-shot detection of a single magnon with a superconducting qubit. *Science* **367**, 425–428 (2020).
148. Gustafsson, M. V. *et al.* Propagating phonons coupled to an artificial atom. *Science* **346**, 207–211 (2014).
149. Chu, Y. *et al.* Quantum acoustics with superconducting qubits. *Science* **358**, 199–202 (2017).
150. Satzinger, K. *et al.* Quantum control of surface acoustic-wave phonons. *Nature* **563**, 661–665 (2018).

151. Kitzman, J. M. *et al.* Phononic bath engineering of a superconducting qubit. *Nature Communications* **14**, 3910 (2023).
152. Kubo, Y. *et al.* Strong Coupling of a Spin Ensemble to a Superconducting Resonator. *Physical Review Letters* **105**, 140502 (2010).
153. Schuster, D. I. *et al.* High-Cooperativity Coupling of Electron-Spin Ensembles to Superconducting Cavities. *Physical Review Letters* **105**, 140501 (14 2010).
154. Dykman, M., Asban, O., Chen, Q., Jin, D. & Lyon, S. Spin dynamics in quantum dots on liquid helium. *Physical Review B* **107**, 035437 (2023).
155. Beysengulov, N. R. *et al.* Coulomb Interaction-Driven Entanglement of Electrons on Helium. *PRX Quantum* **5**, 030324 (3 Aug. 2024).
156. Schuster, D., Fragner, A., Dykman, M., Lyon, S. & Schoelkopf, R. Proposal for manipulating and detecting spin and orbital states of trapped electrons on helium using cavity quantum electrodynamics. *Phys. Rev. Lett* **105**, 040503 (2010).
157. Lea, M., Fozooni, P., Richardson, P. & Blackburn, A. Direct Observation of Many-Electron Magnetoconductivity in a Nondegenerate 2D Electron Liquid. *Phys. Rev. Lett* **73**, 1142–1145 (8 Aug. 1994).
158. Kostylev, I., Hatifi, M., Konstantinov, D. & Chepelianskii, A. Delocalized low-frequency magnetoplasmon in a two-dimensional electron fluid with cylindrical symmetry. *arXiv preprint arXiv:2404.07582* (2024).
159. Rees, D. G. *et al.* Dynamical decoupling and recoupling of the Wigner solid to a liquid helium substrate. *Physical Review B* **102**, 075439 (2020).
160. Dykman, M. personal communication. 2024.
161. Ikegami, H., Akimoto, H. & Kono, K. Melting of Wigner Crystal on Helium in Quasi-One-Dimensional Geometry. *Journal of Low Temperature Physics* **179**, 251–263 (2015).
162. Dykman, M. I. Stick-Slip Motion in a Quantum Field. *Physics* **9**, 54. <https://physics.aps.org/articles/v9/54> (2016).
163. Glattli, D., Andrei, E. & Williams, F. Thermodynamic measurement on the melting of a two-dimensional electron solid. *Physical Review Letters* **60**, 420 (1988).
164. Piacente, G., Schweigert, I. V., Betouras, J. J. & Peeters, F. M. Generic properties of a quasi-one-dimensional classical Wigner crystal. *Physical Review B* **69**, 045324 (2004).
165. Konstantinov, D., Chepelianskii, A. & Kono, K. Resonant Photovoltaic Effect in Surface State Electrons on Liquid Helium. *Journal of the Physical Society of Japan* **81**, 093601 (2012).
166. Kapralov, K. & Svintsov, D. Plasmon Damping in Electronically Open Systems. *Physical Review Letters* **125**, 236801 (23 Dec. 2020).
167. Satou, A., Ryzhii, V. & Chaplik, A. Plasma oscillations in two-dimensional electron channel with nonideally conducting side contacts. *Journal of Applied Physics* **98**, 034502 (Aug. 2005).

168. Torre, I. *et al.* Acoustic plasmons at the crossover between the collisionless and hydrodynamic regimes in two-dimensional electron liquids. *Physical Review B* **99**, 144307 (14 Apr. 2019).
169. Serniak, K. *et al.* Direct dispersive monitoring of charge parity in offset-charge-sensitive transmons. *Physical Review A* **12**, 014052 (2019).
170. Martinis, J. M. *et al.* Decoherence in Josephson Qubits from Dielectric Loss. *Physical Review Letters* **95**, 210503 (2005).
171. Klimov, P. *et al.* Fluctuations of Energy-Relaxation Times in Superconducting Qubits. *Physical Review Letters* **121**, 090502 (2018).
172. Wallraff, A. *et al.* Strong coupling of a single photon to a superconducting qubit using circuit quantum electrodynamics. *Nature* **431**, 162–167 (2004).
173. Schuster, D. I. *Circuit Quantum Electrodynamics* PhD thesis (Yale University, 2007).
174. Koch, J. *et al.* Charge-insensitive qubit design derived from the Cooper pair box. *Physical Review A* **76**, 042319 (4 2007).
175. Clarke, J. & Wilhelm, F. K. Superconducting quantum bits. *Nature* **453**, 1031–1042 (2008).
176. Gambetta, J. M., Chow, J. M. & Steffen, M. Building logical qubits in a superconducting quantum computing system. *npj Quantum Information* **3**, 2 (2017).
177. Arute, F. *et al.* Quantum supremacy using a programmable superconducting processor. *Nature* **574**, 505–510 (2019).
178. Bravyi, S., Dial, O., Gambetta, J. M., Gil, D. & Nazario, Z. The future of quantum computing with superconducting qubits. *Journal of Applied Physics* **132**, 160902 (2022).
179. Simon, J. *Cavity QED with Atomic Ensembles* PhD thesis (Harvard University, 2010).
180. Wu, H. *et al.* Storage of Multiple Coherent Microwave Excitations in an Electron Spin Ensemble. *Physical Review Letters* **105**, 140503 (14 2010).
181. Schleier-Smith, M. H., Leroux, I. D. & Vuletić, V. States of an Ensemble of Two-Level Atoms with Reduced Quantum Uncertainty. *Physical Review Letters*, 073604 (7 2010).
182. Leroux, I. D., Schleier-Smith, M. H. & Vuletić, V. Implementation of Cavity Squeezing of a Collective Atomic Spin. *Physical Review Letters* **104**, 073602 (2010).
183. Lee, J., Vrijsen, G., Teper, I., Hosten, O. & Kasevich, M. A. Many-atom-cavity QED system with homogeneous atom-cavity coupling. *Optics Letters* **39**, 4005–4008 (2014).
184. Fink, J. M. *et al.* Dressed Collective Qubit States and the Tavis-Cummings Model in Circuit QED. *Physical Review Letters*, 083601 (8 2009).
185. Göppl, M. *et al.* Coplanar waveguide resonators for circuit quantum electrodynamics. *Journal of Applied Physics* **104**, 113904 (2008).
186. SourceForge. *WCalc Coplanar Waveguide Calculator* <https://wcalc.sourceforge.net/cgi-bin/coplanar.cgi>.

187. Goldstein, H., Poole, C. P. & Safko, J. L. *Classical Mechanics* (Addison-Wesley, 2002).
188. Tomaru, T. *et al.* Vibration analysis of cryocoolers. *Cryogenics* **44**, 309–317 (2004).
189. Den Haan, A. *et al.* Atomic resolution scanning tunneling microscopy in a cryogen free dilution refrigerator at 15 mK. *Review of Scientific Instruments* **85**, 035112 (2014).
190. Pelliccione, M., Sciambi, A., Bartel, J., Keller, A. & Goldhaber-Gordon, D. Design of a scanning gate microscope for mesoscopic electron systems in a cryogen-free dilution refrigerator. *Review of Scientific Instruments* **84**, 033703 (2013).
191. De Wit, M. *et al.* Vibration isolation with high thermal conductance for a cryogen-free dilution refrigerator. *Review of Scientific Instruments* **90**, 015112 (2019).
192. Kalra, R. *et al.* Vibration-induced electrical noise in a cryogen-free dilution refrigerator: Characterization, mitigation, and impact on qubit coherence. *Review of Scientific Instruments* **87**, 073905 (2016).
193. Mykkänen, E. *et al.* Reducing current noise in cryogenic experiments by vacuum-insulated cables. *Review of Scientific Instruments* **87**, 105111 (2016).
194. Megrant, A. *et al.* Planar superconducting resonators with internal quality factors above one million. *Applied Physics Letters* **100**, 113510 (2012).
195. Schmidt, V. V., Schmidt, V., Müller, P. & Ustinov, A. V. *The physics of superconductors: Introduction to fundamentals and applications* (Springer Science & Business Media, 1997).
196. Van Kann, F. & Winterflood, J. Simple method for absolute calibration of geophones, seismometers, and other inertial vibration sensors. *Review of scientific instruments* **76**, 034501 (2005).
197. De Lorenzo, L. & Schwab, K. Ultra-High Q Acoustic Resonance in Superfluid  $^4\text{He}$ . *Journal of Low Temperature Physics* **186**, 233–240 (2017).
198. Murch, K. W. *et al.* Cavity-Assisted Quantum Bath Engineering. *Physical Review Letters* **109**, 183602 (18 2012).
199. Aiello, G. *et al.* Quantum bath engineering of a high impedance microwave mode through quasiparticle tunneling. *Nature Communications* **13**, 7146 (2022).
200. Collett, M. J. & Gardiner, C. W. Squeezing of intracavity and traveling-wave light fields produced in parametric amplification. *Physical Review A* **30**, 1386–1391 (3 1984).
201. Aspelmeyer, M., Kippenberg, T. J. & Marquardt, F. Cavity optomechanics. *Reviews of Modern Physics* **86**, 1391–1452 (4 2014).
202. Genes, C., Vitali, D., Tombesi, P., Gigan, S. & Aspelmeyer, M. Ground-state cooling of a micromechanical oscillator: Comparing cold damping and cavity-assisted cooling schemes. *Physical Review A* **77**, 033804 (3 2008).
203. Schliesser, A., Rivière, R., Anetsberger, G., Arcizet, O. & Kippenberg, T. J. Resolved-sideband cooling of a micromechanical oscillator. *Nature Physics* **4**, 415–419 (2008).
204. Anetsberger, G. *et al.* Near-field cavity optomechanics with nanomechanical oscillators. *Nature Physics* **5**, 909–914 (2009).

205. Chan, J. *et al.* Laser cooling of a nanomechanical oscillator into its quantum ground state. *Nature* **478**, 89–92 (2011).
206. Verhagen, E., Deléglise, S., Weis, S., Schliesser, A. & Kippenberg, T. J. Quantum-coherent coupling of a mechanical oscillator to an optical cavity mode. *Nature* **482**, 63–67 (2012).
207. Hecht, F. New development in FreeFem++. *J. Numer. Math.* **20**, 251–265. ISSN: 1570-2820. <https://freefem.org/> (2012).
208. Geuzaine, C. & Remacle, J.-F. Gmsh: A 3-D finite element mesh generator with built-in pre- and post-processing facilities. *International Journal for Numerical Methods in Engineering* **79**, 1309–1331. <https://onlinelibrary.wiley.com/doi/abs/10.1002/nme.2579> (2009).
209. Beysengulov, N. R. *ZeroHeliumKit* 2024. <https://github.com/eeroqlab/zeroheliumkit>.